

THE NEAR AND FAR OF PORE PRESSURE DURING
LANDSLIDE AND EARTHQUAKE RUPTURES

A dissertation presented

by

Robert Christian Viesca

to

The School of Engineering and Applied Sciences

in partial fulfillment of the requirements
for the degree of

Doctor of Philosophy

in the subject of

Engineering Sciences

Harvard University
Cambridge, Massachusetts

August 2011

©2011 Robert Christian Viesca
All rights reserved.

Dissertation Advisor: Professor James R. Rice

Robert Christian Viesca

THE NEAR AND FAR OF PORE PRESSURE DURING LANDSLIDE AND EARTHQUAKE RUPTURES

ABSTRACT

Geological materials near the Earth's surface and within the Earth's crust contain pore spaces, largely saturated with water. In this work I study how changes in the pressure of this saturating pore fluid affect deformation, focusing on the deformation of shear ruptures occurring during an earthquake or a landslide. I represent ruptures in both contexts as sliding fractures to better understand the conditions under which they propagate. Elevated pore pressures are frequently cited as a nucleating mechanism, particularly in the landslide context. For undersea landslides, these elevations build upon a preexisting pressurization founded by gradual sedimentation and consolidation, studied here in a simple framework. During initiation, the slow growth of the fracture may give way to fast propagation, corresponding to the source of earthquake shaking and the origin of landslide acceleration. I quantify the extent to which pore pressures, geometry, and material response determine the development. During the fast phase of rupture propagation, pore pressure changes may serve to inhibit or enable inelastic deformation of material away from the slip surface. Such deformation is one of the signatures left by an earthquake. I implement a convenient method for accounting for saturation during rapid rupture propagation and evaluate the impact on the distribution and magnitude of the inelastic deformation. Returning to the slip surface, this inelastic deformation affects fluid flow there on the short timescales of dynamic rupture. I enhance an existing poroelastic model to include these effects.

CONTENTS

ABSTRACT	iii
CONTENTS	iv
LIST OF FIGURES	vii
LIST OF TABLES	xiv
ACKNOWLEDGEMENTS	xv
ACKNOWLEDGEMENT OF SUPPORT	xvii
1 INTRODUCTION	1
2 NUCLEATION OF DYNAMIC RUPTURE BY LOCALIZED INCREASE OF PORE PRESSURE	6
2.1 Abstract	6
2.2 Introduction	7
2.2.1 Narrow shear zones in landslides	7
2.2.2 Previous fracture modeling of landslide and avalanche initiation	9
2.2.3 Extension to account for local sources of pore pressure	12
2.3 Steady, long-time sedimentation with consolidation and effective-stress-dependent permeability	15
2.4 Sources of local increases in pore pressure on seafloor	22
2.5 Rupture nucleation by local increases in pore pressure	25
2.5.1 Nucleation far from a free surface	28
2.5.2 Residual friction and dynamic rupture arrest implications	34
2.5.3 Elastodynamic solutions with rupture arrest	37
2.5.4 Nucleation near a free surface	38
2.6 Discussion and Conclusions	45
3 DYNAMIC RUPTURE IN SATURATED INELASTIC MATERIALS	48
3.1 Abstract	48
3.2 Introduction	49
3.2.1 Previous modeling	49
3.2.2 Objectives of the present work	50

3.3	Background and theory	52
3.3.1	Linear poroelasticity	52
3.3.2	Poroelastoplasticity	54
3.3.3	Slip-weakening friction	58
3.4	Numerical procedure	62
3.4.1	Implementation	62
3.4.2	Parameter selection	64
3.5	Results and discussion	65
3.5.1	Effect of undrained pore pressure generation on extent of inelastic deformation	65
3.5.2	Effect of pore pressure-induced changes in inelastic deformation on rupture propagation	71
3.5.3	Role of undrained conditions and plastic dilatancy in the elimination of plastic localization.	72
3.6	Conclusion	75
4	SLIP-SURFACE PORE PRESSURE CHANGES DUE TO INELASTIC DEFORMATION OF ADJACENT MATERIAL	77
4.1	Abstract	77
4.2	Introduction	78
4.3	Determining pore pressures at a sliding interface with plastically deforming surroundings	80
4.4	Finite element model of a dynamic subsurface rupture	87
4.5	Conclusions	91
5	CONCLUSIONS	92
A	METHODS FOR DETERMINING NUCLEATION LENGTHS	97
A.1	Nucleation lengths for broad-curvature pore pressure profiles and the corresponding eigenvalue problems	97
A.1.1	Nucleation lengths much smaller than depth	97
A.1.2	Nucleation lengths approaching and exceeding depth	99
A.2	Solution by collocation method using Gauss-Chebyshev quadrature .	101
A.2.1	Ruptures with no residual friction	102
A.2.2	Ruptures with residual friction	106
A.3	Approximate solution by a variational method	107
B	ADDITIONAL RESULTS ON DYNAMIC RUPTURE NUCLEATION	110
B.1	Additional slip-dependent behavior: cohesion loss and undrained pore pressure generation	110
B.2	Arrest and renucleation under small-scale yielding conditions	111

B.3	Method to account for largely undrained poroelastic response to sub-surface rupture	113
C	RESOLVING CONFLICTING SOLUTIONS FOR AN EDGE DISLOCATION NEAR A FREE SURFACE	117
C.1	Background	117
C.2	Elastic reciprocity	120
C.3	Symmetry	122
C.4	Coordinate changes	123
C.5	Expressions for stress due to edge dislocations under change of coordinates, Burgers vector convention	125
C.6	Stress intensity factors for a uniformly pressurized subsurface crack .	128
D	INELASTIC CONSTITUTIVE PROPERTIES IN THE DEFORMATION OF SATURATED POROUS MEDIA	129
E	DERIVATION OF EFFECTIVE MATERIAL PARAMETERS FOR UNDRAINED BEHAVIOR	134
	BIBLIOGRAPHY	138

LIST OF FIGURES

Figure 1.1 Schematic overview of the locations of interest for each chapter.

The general focus of the thesis is on the role of pore pressures during a shear rupture within porous materials, such as (a) the basal slip surface of a landslide and (b) the slip surface of an earthquake fault. Black lines indicate slipping region while the adjacent arrows indicate sense of relative displacement and the propagation direction. Chapter 2 focuses on the pore pressures along the slip surface and its potential extension (dashed lines). Chapter 3 moves away from the slip surface to examine how pore pressure changes affect deformation. Chapter 4 examines pore pressure changes just adjacent to the slip surface (and their effects on the pore pressure on the slip surface itself).

2

Figure 2.1 Comparison of pore pressure in excess of hydrostatic, $u(z)$, determined by separate measurements on the southern shelf of the Mississippi delta (points) and by models representing steady sedimentation (colored lines). Models treat permeability either as a constant (dashed red) or as an exponentially decreasing function of effective stress (blue). Two of the models are direct solutions of steady sedimentation-consolidation problems with a hydrostatic pore-pressure gradient at the seafloor while the third (dashed blue) is the solution to a problem of constant flow q_c (hence its departure at shallow depths). Total normal stress of model (black) plotted for comparison.

19

Figure 2.2 Superposition of a peaked pore pressure profile along a depth h (blue) on an illustration of a slipping region that parallels a slope surface (both black). The profile shown corresponds precisely to that which would generate the illustrated slipping region. The slipping region is enlarged by a gradual increase of pore pressure $\Delta p(x, t)$ to a critical extent, illustrated here at $t = t_c$, beyond which its growth may continue without any further pressure increase. The value $\Delta p(0, 0) = \sigma'_o - \tau_o/f_p$ is that at which a failure criterion is first met and sliding is initiated at the origin. A frictional length scale ℓ is used to denote relative depth by $H \equiv \sqrt{h/\ell}$. Here $\tau_o/\sigma'_o = 0.25$ and $f_p = 0.5$ (i.e., $\Delta p(0, 0) = 0.5\sigma'_o$), $H = 0.5$, and $K_{h\ell} = 1$ is the dimensionless profile curvature defined in text. Interestingly, in the case considered here, only a marginal increase past $\Delta p(0, 0)$ is required to bring the slope to the critical point.

24

Figure 2.3 (a) Enlargement of crack length $a(t)$ with increasing pore pressure Rt , nondimensionally as T , for profiles of pore pressure with various curvatures κ , nondimensionally as K . (b) Plot of maximum slip $\delta_{max}(t)$, occurring at $x = 0$, against pore pressure increase. The nucleation of a dynamic rupture occurs at the peak of the loading paths and the crack propagates without any further increase in pore pressure. (c) Plot of peak slip (red) and pore pressure increase (blue) against the crack length at the point of nucleation. (d) Plot of peak slip at nucleation against the nondimensional profile curvature. These analyses assume that $f_r/f_p < (1 - w\delta_{max}/f_p)$, implying that solutions with $w\delta_{max}/f_p > 1$ are unphysical.

30

Figure 2.4 Distribution of (a) slip and (b) shear stress change for various levels of pore pressure increase $T \equiv Rt f_p/\tau_o$ and fixed curvature $K \equiv f_p \kappa \ell^2/\tau_o = 1$. (c) Ratio of shear stress to effective normal stress for $f_p = 0.6$ and $\tau_o/\sigma'_o = 0.3$. Solid curves are those distributions originating from a nucleated crack of zero length to an unstable limit (bold), dashed curves are unstable distributions beyond the point of nucleation.

32

Figure 2.5 Solutions of crack length $a(t)$ with increase in pore pressure T at a fixed curvature $K = 1$. Solid and dashed lines represent stable and unstable quasistatic solutions. (a) Solutions for variable f_r/f_p , and the solution neglecting residual friction. In these solutions the shear stress is small (low τ_o/τ_p). Starting with the solution of (a), $f_r/f_p = 0.5$ (red), the solutions in (b) show the result of increasing shear stress τ_o/τ_p (black).

34

Figure 2.6 Dynamic rupture arrest (Case 1, a–b) and continuation (Case 2, c–d) as indicated by plots of slip and shear stress at time intervals of ℓ/c_s . The cases correspond to two cases of Figure 2.5b. In both cases $f_r/f_p = 0.5$, and the sole difference is an increase in shear stress from $\tau_o/\tau_p = 0.5$ for Case 1 to $\tau_o/\tau_p = 0.7$ for Case 2. Each rupture is nucleated by suddenly applying the same critical loading $\Delta p(x, t_c)$ (with profile curvature $K = 1$) as the initial condition. The dashed lines in (a–b) correspond to arrest length predicted by quasi-static solution (point (B) in Figure 2.5b).

Figure 2.7 Distribution of (a) slip, (b) shear stress, and (c) total normal stress for given pore pressure increase T with a fixed curvature (normalized such that $K_{hl} \equiv f_p \kappa h \ell / \tau_o = 1$), and fixed effective depth ($H \equiv \sqrt{h/\ell} = 0.1$, such that x -axis limits are $\pm 40h$). Curves in black outline those distributions originating from a nucleated crack of zero length to an unstable limit (bold).

Figure 2.8 (a) Crack half-length, (b) crack asymmetry, (c) peak slip, and (d) pore pressure increase all at the nucleation condition for $f_p = 0.5$, fixed non-dimensional pore pressure curvature ($K_{hl} \equiv f_p \kappa h \ell / \tau_o = 0.01$), and variable effective depth ($H \equiv \sqrt{h/\ell}$). For such broad increases in pore pressure, the plots show and a limiting behavior for ruptures much longer than their depth, and particularly a transition in nucleation behavior from an effectively deep scaling at large H , $a(t_c) \approx 0.579\ell$, to a shallow one at low H , $a(t_c) \approx 2.2\sqrt{h\ell}$. The former scaling follows from the eigenvalue problem of *Uenishi and Rice* [2003], and the latter from a comparable eigenvalue problem in Appendix A.1.2.

Figure 2.9 Variation of critical slip surface lengths, $2a(t_c)$, with burial depth under submarine and subaerial conditions. These lengths mark the onset of dynamic slip surface growth and downslope acceleration. Solutions presented for case where pore pressures are nearly uniformly elevated over the length $2a(t_c)$ (as in Figure 2.8a). Submarine conditions reflect a sediment bulk weight of $\gamma_b = 1.5\gamma_w$ and shallow slope angles. Subaerial conditions reflect $\gamma_b = 2\gamma_w$ and steeper slopes. In all cases the Poisson ratio is $\nu = 1/3$ and peak friction is $f_p = 0.5$. Results in (a) are for a range of slope angles in both environments; intermediate values of the slip-weakening rate w and shear modulus μ are used. The dashed lines show the scalings of nucleation lengths in the “deep” and “shallow” limits for the bounding submarine cases. Results in (b) and (c) are, respectively, for low and high slip-weakening rates w , each over a range of sediment stiffnesses.

Figure 3.1 Adapted from Rice et al. [2005]. Contour plot of ratio of maximum shear stress to maximum Coulomb strength as a function of position around tip of a propagating right-lateral slip pulse for different inclination angles of the initial most compressive stress, $\Psi = (1/2) \tan^{-1}[2\sigma_{xy}^o/(\sigma_{xx}^o - \sigma_{yy}^o)]$, with the fault in a medium without and with undrained poroelastic response (left column, Skempton $B = 0$; right column, $B = 0.6$, respectively). The seismic S ratio is 6.4 and $f_r/f_d = 0.2$. Rupture speeds are scaled with the shear wave speed C_s (so that these cases are very near the Rayleigh wave speed, $0.92C_s$), and distance with the scale length R_o^* (called R_o in the text) that the slip-weakening zone would have at very low propagation speed and under a pre-stress corresponding to a large value of the seismic S ratio. 51

Figure 3.2 Illustration of the effective undrained cohesion, b_u , and internal friction coefficient, μ_u , for a given initial effective stress state, σ_{ij}^o , drained cohesion, b , and drained internal friction, μ . Here $\sigma_{kk} = \sigma_{kk}^o + \Delta\sigma_{kk}$ where $\Delta\sigma_{kk}$ is the total stress change that occurs under undrained conditions; and here $\bar{\tau}$ is based on s_{ij} , where $s_{ij} = s_{ij}^o + \Delta s_{ij}$ where s_{ij}^o is independent of initial pore pressure. 58

Figure 3.3 a) 2D Model geometry with initial stresses resulting in an angle of most compressive stress to the fault, Ψ . The right-lateral rupture is nucleated in the center of the fault along length L'_c . b) Linear slip-weakening friction model used to describe the degradation of the shear strength of the fault from a peak to a residual strength as a function of slip along the fault. c) Example stress distribution around crack tip during propagation; R_o is the size of R in the limit of low rupture speed and large seismic S ratio, G is shear modulus. d) Fault shear stresses resulting from proscribed initial slip distribution over length L'_c slightly greater than static nucleation length estimate L_c 59

Figure 3.4 Contour plots of $\gamma^{pl}/(\tau_p/2G)$ as a function of distance from the fault for $S = 1$, for $\Psi = 14^\circ$, fixed on- and off-fault strength parameters ($f_s = 0.65$, $f_d = 0.05$; $\mu = 0.6$ ($\tan \phi = 0.75$)), fixed closeness of the initial stress state to off-fault failure ($CF = 0.8$), and no plastic dilation. We consider a case in which pore pressure changes are neglected ($\Delta p = 0$) and undrained cases for which an increase of the Skempton coefficient ($B = 0.5, 0.7, 0.9$) illustrates the role of undrained pore pressure generation in increasing the extent of inelastic deformation. 66

Figure 3.5 Contour plots of $\gamma^{pl}/(\tau_p/2G)$ as a function of distance from the fault for $S = 1, \Psi = 56^\circ$, fixed on- and off-fault strength parameters ($f_s = 0.45, f_d = 0.045; \mu = 0.6$), fixed closeness of the initial stress state to off-fault failure ($CF = 0.5$), and no plastic dilation. We consider a case in which pore pressure changes are neglected ($\Delta p = 0$) and undrained cases for which an increase of the Skempton coefficient ($B = 0.5, 0.7, 0.9$). As a contrast to a shallower angle ($\Psi = 14^\circ$, Figure 3.4), the drained response exhibits deformation on the extensional side of the fault. Here the undrained cases ($B = 0.5, 0.7, 0.9$) show a decrease in inelastic deformation.

68

Figure 3.6 Contours of $\gamma^{pl}/(\tau_p/2G)$ as a function of distance from the fault, with all parameters the same as in Figure 3.4, except here we consider the effects of inelastic dilatancy on the undrained response. For the case of Figure 3.4 in which $B = 0.7$ (repeated at top here), increasing plastic dilatancy ($\beta = 0, 0.2, 0.4$) has significant effect on reducing the extent of inelastic deformation.

69

Figure 3.7 Contours of $\gamma^{pl}/(\tau_p/2G)$ as a function of distance from the fault, with all parameters the same as in Figure 3.5, except here we consider the effects of inelastic dilatancy on the undrained response. For the case of Figure 3.4 in which $B = 0.7$ (repeated at top here), introducing plastic dilatancy serves to reduce the extent plasticity, but does not have as significant effect as in Figure 3.6

70

Figure 3.8 Plot of normalized rupture tip position versus normalized time for drained and undrained $\Psi = 14^\circ$ cases of Figure 3.4 (i.e., without inelastic dilatancy). Here C_S is the shear wave speed. The increasing extent of inelastic deformation from drained to undrained responses is reflected in the slight delay for the rupture tip to reach a particular distance of the fault.

72

Figure 3.9 Plot of normalized rupture tip position versus normalized time for undrained $\Psi = 14^\circ$ cases of Figure 3.6 with and without dilatancy. Here, the decreasing extent of inelastic deformation with increasing dilatancy is reflected in the slight decrease in time for the rupture tip to reach a particular distance of the fault. In addition to the cases presented in Figure 3.6, we also consider a case of rupture in an undrained elastic medium. In Figure 3.8 we considered a similar elastic case neglecting pore pressure changes. Here we find that under undrained conditions, the rupture transitions to supershear.

73

Figure 3.10 Plots of the normalized critical value of hardening h_{cr} , at which localization is expected to occur for static loading, versus the stress state parameter N . No localization of deformation is expected if $h \geq h_{cr}$. (a) Here, we neglect effects of inelastic dilatancy ($\beta = 0$). (b) Here, we consider a dilatancy $\beta = 0.3$ and hold all other parameters fixed. Note the effect of dilatant hardening in the reduction of $h_{cr,u}$.	74
Figure 4.1 Illustration of pressure-dependent yield criterion F .	81
Figure 4.2 Plot of factor of increase in storage coefficients (compressibilities) with onset of ideally plastic ($h = 0$) yielding for compacting sediment (dashed) and dilating rock (solid) over a range of stress states for which $s_{zz} = 0$, $s_{xy}/\bar{\tau} = \sin \theta$, and $s_{xx}/\bar{\tau} = -s_{yy}/\bar{\tau} = \cos \theta$.	84
Figure 4.3 (a) Schematic of portion of model domain (actual downdip length \tilde{R}), initial stresses, and subsequent behavior. (b) Snapshots of effective normal stress along the slip surface at intervals of $3.75\tilde{R}/c_s$ for a subsurface rupture at depth $H = 1.5\tilde{R}$ in a saturated poroelastic body. Rupture shows preferred downslope propagation and significant normal stress changes. Model initial stress state is defined as $\bar{\sigma}_{yy}^o = (\gamma_b - \gamma_w)H \cos \theta$, $\bar{\sigma}_{xy}^o = (\gamma_b - \gamma_w)H \sin \theta$, $\bar{\sigma}_{xx}^o = K_o \bar{\sigma}_{yy}^o$, and $\bar{\sigma}_{zz}^o = (\bar{\sigma}_{xx}^o + \bar{\sigma}_{yy}^o)/2$, where $\gamma_b = 1.75\gamma_w$, $\theta = 15.75^\circ$, and $K_o = 1$. Surface frictional parameters are $f_p = 0.45$, $f_r = 0.2$, and $t^* = 0.015\tilde{R}/c_s$. Bulk poroelastic parameters are $G = 600\bar{\sigma}_{yy}^o$, $\nu = 0.35$, and $\nu_u = 0.483$, and $B = 0.4$	88
Figure 4.4 Snapshots of slip surface shear stress changes in elasticplastic saturated medium (a) neglecting slip surface pore pressure changes and (b) including elastic-plastic effects on pore pressure changes	90
Figure A.1 Comparison of numerical solutions for crack length at nucleation, $a(t_c)/\sqrt{h\ell}$ with dimensionless depth $h/\sqrt{h\ell}$ of Figure 2.8a (solid line) against solutions to the eigenvalue problem of (A.5) in the limit of very broad pore pressure increases, $K_{hl} \rightarrow 0$ (open circles).	100
Figure A.2 Comparison of solutions for (a) crack length and (b) peak slip arrived at directly by Chebyshev-Gauss quadrature (black), as in Figure 2.3, and approximately by the simpler variational approach (grey). Dashed lines highlight the divergence, between methods, of the dynamic rupture nucleation point for increasingly peaked pore pressures.	108

LIST OF TABLES

Table C.1 Mode-I and -II stress intensity factors for a plane-strain, surface-parallel crack under uniform pressure.	127
--	-----

ACKNOWLEDGEMENTS

To put it simply, my Ph.D. advisor, Jim Rice, has been great. He's had a selfless interest in my development and I'm thankful for the advice, responsibility, and room he's provided as my Ph.D. progressed. I'm also thankful for his careful thought, expression, and discernment, and I've enjoyed the collegiality he has always offered.

Thanks to my dissertation committee members, Professors Dmitry Garagash, Taylor Perron, John Shaw and Zhigang Suo, for discussion and advice along the way. I feel lucky to have had such a complementary group.

I thank Jim and Renata Dmowska for the wonderful, collaborative group they cultivated. Thanks to Harsha Bhat, Eric Dunham, and Yajing Liu for their guidance as the more senior members of the group; Elizabeth Templeton-Barrett for her collaboration and support, especially as I started out; Victor Tsai and Nora DeDontney for numerous discussions and Nora for company as the other half of my cohort; and the newest student, John Platt, for making me feel both young and old. I've also had the fortune of being here for many more visitors to the group, each of whom has added another precious facet to my time here.

The third floor of Pierce Hall, where I've sat for most of my Ph.D., seems to have a tide that regularly brings in an interesting crew. I owe much to these folk, those I've known before, and those I've met otherwise for making the time during my Ph.D.

such a rich education.

To my parents, Kristina, Fernando, and Elizabeth, who sacrificed so much of their time and thoughts for my benefit, and supported and encouraged my pursuits: I've felt catapulted and you'll always have my thanks.

I thank my wife Emilie for the near and far of all those years. An explorer with a sharp wit, open and committed, she has influenced my work in an inseparable way. Her warmth, humor, good nature, and love have given me much joy and have made hard moments bearable, particularly those apart. I look forward to the discoveries that remain.

ACKNOWLEDGEMENT OF SUPPORT

I would like to gratefully acknowledge the support received during the period of this doctoral work (Sept. 2005 – Aug. 2011). I would particularly like to thank Total E & P Recherche Développement and Total PIs Jérôme Adamy and Sylvie Grimaud for sponsoring the final two and a half years through a collaborative agreement with Harvard University (FR00003219). Support prior to this came from the Division (now School) of Engineering and Applied Sciences (for 1.5 years); the Integrated Ocean Drilling Project (IODP)/Consortium for Ocean Leadership Schlanger Ocean Drilling Fellowship and a grant from the Harvard University Center for the Environment (each for the support of approximately 0.5 years). Additional support also came from the Southern California Earthquake Center (funded by NSF Cooperative Agreement EAR-0106924 and USGS Cooperative Agreement 02HQAG0008), and NSF-EAR grants 050193 and 0809610.

CHAPTER 1

INTRODUCTION

Thesis overview

In this thesis we examine the role of pore pressures during the localized deformation of earthquakes and landslides as shear ruptures. Figure 1.1 shows a schematic illustration of a slipping region as may exist below the Earth's surface a) as a landslide and b) fault movement. The structure of this thesis is organized around 1) the evolution of the slip surface, from slow initiation to dynamic enlargement and 2) the location of pore pressure changes. Chapter 2 is concerned with the pore pressure distribution along the entire slip surface and potential failure plane; as well as consequences of a peaked distribution slowly growing the slipping region to a catastrophic limit. Chapter 3 and 4 cover periods where deformation rates are fast and fluid diffusion limited. In these chapters, the interest is in quantifying the consequences of pore pressure changes in material both away from (Ch. 3), adjacent to, and on the slip surface (Ch. 4). The body of the work focuses on the presentation of these problems and highlighting results: additional details, derivations and methods are relegated to the appendices.

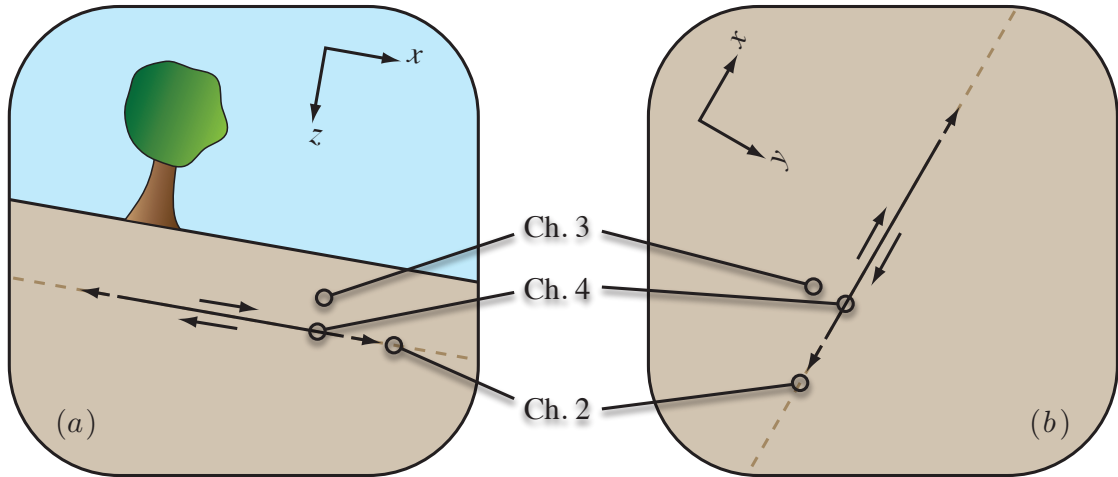


Figure 1.1: Schematic overview of the locations of interest for each chapter. The general focus of the thesis is on the role of pore pressures during a shear rupture within porous materials, such as (a) the basal slip surface of a landslide and (b) the slip surface of an earthquake fault. Black lines indicate slipping region while the adjacent arrows indicate sense of relative displacement and the propagation direction. Chapter 2 focuses on the pore pressures along the slip surface and its potential extension (dashed lines). Chapter 3 moves away from the slip surface to examine how pore pressure changes affect deformation. Chapter 4 examines pore pressure changes just adjacent to the slip surface (and their effects on the pore pressure on the slip surface itself).

Chapter 2

Observations indicate that deformation in a landslide may be localized to the point where downslope motion is effectively accommodated by a basal slip surface [Cooper et al., 1998; Wen and Aydin, 2003, 2004]. Following others, we take the further step to presume that the slip surface does not appear spontaneously over the entire length of the landslide, but instead grows to a finite size before proceeding catastrophically [Palmer and Rice, 1973; Cleary and Rice, 1974; McClung, 1979; Bazant et al., 2003; Puzrin et al., 2004; Puzrin and Germanovich, 2005; McClung, 2009]. We look at the growth of the slipping region by increases in pore pressure, which can also be representative of earthquake rupture initiation. We place some emphasis on submarine

slopes, particularly when examining ambient conditions and potential sources for local pore pressures. This environment is of particular interest as it poses seemingly paradoxical behavior: the shallow slopes would seem to preclude any landsliding, but in fact the environment is the frequent host of some of the world's largest [e.g., Canals et al., 2004]. We look towards the fracture representation to see if such a model would be sufficiently able to account for shallow slope failure as well as the order of magnitude (or greater) difference in size between submarine and subaerial landslides. To do so, we take the representative fracture solutions several steps further to consider differences in the setting (submarine versus subaerial), failure geometry (depth to slip surface), as well the evolution of slip in response to a gradually increasing pore pressure distribution. Features resulting from the model include 1) the potential for a portion of the slope to suddenly accelerate and arrest under a fixed increase in pore pressure, 2) which may occur at low slope angles; as well as 3) a significant increase in expected failure from several tens of meters to several hundred meters for subaerial and submarine slopes, respectively.

Chapter 3

Within the landslide fracture model, the sudden slope acceleration is accompanied by the dynamic growth of the slip surface, as in an earthquake-generating rupture propagation. During the fast progression of the rupture tip, stress concentrations in an elastic medium would be expected to reach a point of inelastic yielding [Poliakov et al., 2002; Rice et al., 2005]. Consequently, recent work has numerically calculated the extent and intensity of inelastic deformation by implementing a yield criterion allowing for the elastic-plastic response of the material away from the slip surface [Andrews, 2005; Ben-Zion and Shi, 2005; Duan and Day, 2008; Templeton and Rice,

2008; Hok et al., 2010; Dunham et al., 2011b,a]. However, these studies generally neglected that this material is fluid saturated. The deformation rates in this dynamic phase leave little time for fluid to diffuse and for pore pressures to equilibrate. Consequently, pore pressures may increase or decrease under these undrained conditions, bringing material closer or further from failure. We discuss how to appropriately account for elastic-plastic deformation in undrained conditions. Additionally, we incorporate the method into a dynamic rupture study and find that the distribution of plastic strain may be significantly altered by changes in pore pressure.

Chapter 4

To understand the conditions that lead to instability, or help sustain it, there is an interest in the pore pressure changes on the slip surface. The general focus by the earthquake-rupture community has been on weakening mechanisms due to the behavior within the thin shear zone that the slip surface approximates. Such mechanisms include thermal pressurization (whereby fast shear heating, thermally expansive fluid, and stiff pore spaces lead to increases in pore pressures), mineral decomposition, and dilatancy [e.g., Sibson, 1973; Lachenbruch, 1980; Rice, 1980; Han et al., 2007]. Another contribution is due to the deformation of the porous material adjacent to the slip surface (i.e., the adjacent material diffusively sampled by the slip surface on the timescale of interest). This problem in the poroelastic case was addressed by Rudnicki and Rice [2006] and Dunham and Rice [2008]. We extend this to include the possibility that the adjacent material may yield plastically as slip occurs. The two commonly understood effects of plastic deformation are 1) pore pressure changes due to dilatancy or compaction and 2) a potential increase or decrease in fluid permeability. We quantify an additional effect that is likely often

neglected in treatments of pore fluid movement during plastic deformation: 3) namely, that the pore fluid storage coefficient increases due to an increase in compliance of the yielding material. We then implement an approximation to calculate the pore pressure change on the slip surface account for 1) and 3).

CHAPTER 2

NUCLEATION OF DYNAMIC RUPTURE BY LOCALIZED INCREASE OF PORE PRESSURE

2.1 ABSTRACT

We model landslide initiation as slip surface growth driven by local elevated pore pressure, with particular reference to submarine slides. Assuming an elastic medium and friction that weakens with slip, solutions exist in which the slip surface may dynamically grow, without further pore pressure increases, at a rate of the order of the sediment shear wave speed, a situation comparable to earthquake nucleation. The size of the rupture at this transition point depends weakly on the imposed pore pressure profile; however, the amount of slip at the transition depends strongly on whether the pore pressure was broadly or sharply elevated. Sharper profiles may also result in pore pressures reaching the total slope-normal stress before dynamic rupture is nucleated. While we do not account for modes of failure other than pure slip on a failure surface, this may be an indication that additional modes involving liquefaction or hydraulic cracking may be factors in the initiation of shallow slope

This chapter, as well as the contents of Appendix A, are in preparation for submission as “Viesca, R.C., and J. R. Rice, Nucleation of slip-weakening rupture instability in landslides by localized increase of pore pressure” to *J. Geophys. Res.*

failure. We identify two lengthscales, one geometrical (h , depth below the free surface) and one material (ℓ , determined by the frictional weakening rate) and a transition in nucleation behavior between effectively “deep” and “shallow” limits dependent on their ratio. Whether dynamic propagation of failure is indefinite or arresting depends largely on whether the background shear stress is closer to nominal peak or residual frictional strength. This is determined in part by background pore pressures, and to consider the submarine case we simplify a common sedimentation/consolidation approach to reflect interest in near-seafloor conditions.

2.2 INTRODUCTION

2.2.1 NARROW SHEAR ZONES IN LANDSLIDES

Landslides on land have often been observed to occur as slip on a localized shear surface within the soil column. The excavation of a failed clay slope in Selborne England, where failure was artificially triggered by fluid injection under experimental conditions, revealed a shear zone of mm thickness within a cm-scale disturbed zone, creating an arcuate shape that extended to a peak depth of 4 m below the slope surface Cooper et al. [1998]. Trenching following a naturally (rainfall) induced slope failure revealed a disturbed zone 2–20 mm thick occurring within decomposed granite or within clay seams at comparable 2–5 m depths [Wen and Aydin, 2003, 2004]. Similar to the Selborne failure, much of the downslope displacement was inferred to have occurred over shear zones < 5 mm thick. Extensive observations of landslides in southern Italy show extended periods of slow, downslope motion [summarized in Picarelli et al., 2005]. In addition to excavation of the slip surface, string inclinometers were used to infer the displacement profile with depth over time and shear was observed to occupy a thickness at or below the resolution of the inclinometers (\sim 50 cm)

[Picarelli et al., 1995; Pellegrino et al., 2004]. Slip surfaces have also been detected in landslides at quite shallow depths. In a landslide induced by artificial rainfall, the deflection of a buried rod with strain gauges attached at 10-cm spacings gave an indication that a shear zone developed below the strain gauge resolution at depths ranging from 0.6–1.2 m [Ochiai et al., 2004]. Discontinuities in displacement may occur laterally as well, as observed by geodetic data from the steadily creeping Slumgullion earthflow [Gomberg et al., 1995].

Despite much lower resolution of observation in the submarine environment, there remains evidence to suggest that downslope motion may occur as translation of material overlying a shear zone that is thin relative to its depth. One indication is simply the apparent slide morphology with an example being the Gaviota slide off of the California coast. The slide is a sheet-like failure bounded by upslope detachment and thrusting out of the apparent failure plane occurring at the toe [Edwards et al., 1995]. Furthermore, an open gap that is colinear with the landslide headscarp and extends for several kilometers indicates that the adjacent regions started to move downslope. At its largest, the gap is 2 m deep (compared to 6–8 m deep headscarp of the adjacent failure) and 10 m wide, however high resolution (< 1 m in depth) seismic data show no apparent signs of disturbance from the sediment deformation, consistent with initial slip on a surface-parallel rupture [Blum et al., 2010]. Limits on resolution are also partially compensated by the accessibility through seismic data of failures preserved under deep sediment drapes. Offshore Angola, Gee et al. [2005] uncovered blocks of sediment with seismically intact stratigraphy that had been transported downslope several kilometers. The dimensions of the blocks themselves reach several kilometers in length and are approximately 100 m in depth. In such instances there is often mentioned a “weak horizon” implying that for the stratigraphy to remain as parallel

reflectors, downslope movement is translational with shear localized to a basal layer.

Such localized deformation may be expected for materials that weaken with shear. The Selborne event occurred in overconsolidated sediments (i.e., soils that have previously supported greater overburden than at present), for which such weakening is commonly known to exist and is demonstrated, for example, in ring shear tests where localized deformation is kinematically enforced [e.g., Bishop, 1971] or in a triaxial cell in which weakening occurs and localization is allowed to develop spontaneously. In contrast to overconsolidated sediments, normally consolidated sediments (i.e., soils whose current overburden is the largest ever supported) are thought to strengthen with shear. However, while marine sediments are ideally considered as normally consolidated, given typical sedimentation rates on these slopes (\sim mm/yr or less) strength may develop due to the long lifetime of interparticle contacts. Such behavior is indicated by increased sample stiffness following long periods of fixed loads in consolidation tests [e.g., Karig and Ask, 2003]; by the development of increasingly peaked stress-strain profiles under triaxial loading conditions for normally consolidated samples previously held under loads for increasingly long times [e.g., Bjerrum and Lo, 1963]; as well as evidence of strength regain in ring-shear tests upon fixed displacement [e.g., Stark et al., 2005; Carrubba and Del Fabbro, 2008; Stark and Hussain, 2010]. Such strength would be lost upon sufficient disruption of contacts (i.e., the sediments are considered sensitive), and if weakening is sufficiently strong, localized deformation may be expected as is for overconsolidated sediments.

2.2.2 PREVIOUS FRACTURE MODELING OF LANDSLIDE AND AVALANCHE INITIATION

That weakening leads to localized deformation has been a basis for theoretical work of slope stability, where the shear zone is approximated as a discontinuity in shear dis-

placement (slip, δ) occurring across a surface. This representation has the advantage that stress and displacements in the slope may be readily calculated for a given distribution of slip or stress on the discontinuity [as in Muller and Martel, 2000; Martel, 2004]. The work on initiation has most commonly been done under the assumption of linear elastic behavior of sediments in response to slip parallel to a free surface at a depth h ; and that the shear strength on the slip surface weakens from a peak τ_p to residual value τ_r over a characteristic amount of slip δ_c . The purpose of this line of work has been to examine conditions under which the slipping region will propagate without external forcing (other than gravity).

Much of the work in this field has assumed *a priori* that the unstable rupture length will be much longer than the depth. As a result of this assumption, the analyses can reasonably neglect the deformation of the material underlying the slip surface and also presume that the overlying material undergoes a uniform compression or extension in response to the slip. While this may seem reasonable for submarine slope failures where lengths often exceed a kilometer, we examine in a later section the conditions under which this assumption is reasonable. The first work in this vein was that of Palmer and Rice [1973] who examined the scenario of a slip-surface induced by the relief of stress from a cut in a slope. McClung [1979] extended this analysis to the representation of snow slab avalanches for the case when the crack originates not from a cut in the slope, but within the slope itself. Puzrin et al. [2004] performed a similar analysis in the landslide context. An additional simplifying assumption in much of the above work is that the weakening from peak to residual occurs over a distance from the rupture tip that is small compared to the depth. This so-called small-scale-yielding assumption effectively presumes that the strength of the slipping surface is at the residual level over the length of the crack. While keeping the shallow

depth assumption, this assumption of small-scale-yielding was relaxed in subsequent work [Cleary and Rice, 1974; Bazant et al., 2003; Puzrin et al., 2004; Puzrin and Germanovich, 2005; McClung, 2009].

In this shallow depth limit, the crack length at which propagation occurs was found to scale with the length

$$\sqrt{\frac{E^* h \delta_c}{\tau_p - \tau_r}} \quad (2.1)$$

where $E^* = 2\mu/(1 - \nu)$ as the plane-strain modulus relating stress changes to the extension and compression of the overlying material (and μ and ν are the shear modulus and Poisson ratio). Recent work has begun to consider finite aspect ratios of crack length to depth. Studying the initiation of snow-slab avalanches by the presence of uniformly weak regions in the slipping zone, Bazant et al. [2003] assumed both a finite slip-weakening region and burial depth, but treated the underlying material as rigid, as is effectively assumed in the shallow crack limit. In this work we will explore the transition in behavior from that of a deeply buried slip surface to that in a shallow limit for finite-size weakening zones.

The above work lies in parallel to that pursued in mechanics of faulting, akin to a deeply buried limit [e.g., Ida, 1972]. Uenishi and Rice [2003] studied the quasistatic growth of slip-weakening shear fracture in a linear elastic medium by a locally increasing concentration of shear stress on the fault. They observed that the fracture may reach a length at which its growth may continue without further increases in shear stress, corresponding to the nucleation of a dynamically propagating rupture. Furthermore, the key result was their observation that, so long as shear strength weakened linearly with slip (with slope $(\tau_p - \tau_r)/d_c$), this critical length was independent of the shape of the shear stress concentration. At this nucleation limit, they showed that the problem reduced to a eigenvalue problem the smallest eigenvalue of

which corresponds to the critical length, approximately

$$0.579 \frac{\mu^* \delta_c}{\tau_p - \tau_r} \quad (2.2)$$

where μ^* is $\mu/(1 - \nu)$ for mode II (slip in the direction of rupture propagation, as assumed for work above) and μ for mode III (slip direction normal to rupture propagation). In this work we will arrive at a comparable eigenvalue problem to find the critical length under similar conditions near a free surface. While nucleation under slip-weakening friction continues to be of interest for some dynamic rupture models [e.g., Bizzarri, 2010], experiments indicate that friction on faults at the slow slip rates of the nucleation stage may be better represented by a slip rate and state dependence and consequently, there has been a shift of focus to nucleation under this condition [Tse and Rice, 1986; Dieterich, 1992; Lapusta et al., 2000; Rubin and Ampuero, 2005; Ampuero and Rubin, 2008; Rubin and Ampuero, 2009].

2.2.3 EXTENSION TO ACCOUNT FOR LOCAL SOURCES OF PORE PRESSURE

Within the landslide context, what has yet to be thoroughly studied in fracture growth is the role of the triggering mechanism, the most commonly cited of which is an increase in pore pressure. Rather than static increases in levels of shear stress, the effective stress is reduced, lowering the frictional contribution to shear strength. Of interest here is the growth of a thin shear rupture in direct response to local elevations of pore pressure, and how such local slip may catastrophically grow to induce failure over a much larger area. To isolate this response, we exclude potential for weakening other than that induced by slip. This is in slight contrast to work that seeks to couple this effect with the potential formation and coalescence of weakened, but not necessarily localized, regions of deformation to explain apparent acceleration of

deformation over days prior to failure [Kilburn and Petley, 2003; Petley et al., 2005]. For the infinite-slope-type problems considered for fracture propagation, promising work in this direction explored both shear-stress and pore-pressure loading via a finite element discretization of a shear-softening basal layer lying above a rigid boundary layer and below an elastic-ideally plastic material [Wiberg et al., 1990]. Of particular interest here is how localized failure may propagate while pore pressure remains at a level below confining stress levels, at which point conditions may be met for liquefaction (a complete loss of sediment shear strength, typically assumed here to be frictionally determined) or the opening of a hydraulic fracture. Our intention is not to exclude these possibilities, which are beyond the scope of this paper, and indeed we will find in the course of this study that such scenarios may not be easily avoidable in certain environments.

Observations have been made where pore pressures remain below confining stresses and induced slip extends over a region larger a local elevation. In the Selborne experiment [Cooper et al., 1998], failure was triggered within the overconsolidated clay by injecting water over a period of several months. In the days preceding failure, the pore pressures averaged along the eventual slip surface (as estimated from that of adjacent piezometers) reached only approximately 15% of the vertical overburden. Not only is this well below probable lithostatic stress levels, but it is also well below what would generally be expected for initiation of failure on the nominal slope angle ($\sim 25^\circ$). However, when examining the distribution of pore pressure along the slip surface, the authors find a pronounced peak approximately midslope, during a period of slow movement 12 days before catastrophic collapse. The highest pore pressure in that local peak is approximately 48 kPa at 4.2 m below the surface. With an estimated bulk soil unit weight a factor 1.7–2 times that of water, this pore pressure

seems sufficient to induce localized slip while remaining below lithostatic stresses.

A well-instrumented slope hollow in the Oregon Coast Range underwent recorded changes in head with depth during a rainstorm that precipitated a shallow (~ 0.5 m-deep) landslide [Montgomery et al., 2009]. There, frictional strength alone would be insufficient to maintain the soil on such steep, $\sim 40^\circ$ slopes and effective cohesive strength was provided by a root network. The observations indicate that fractured bedrock channelized the infiltrating flow towards the hollow and caused localized seepage into the overlying soil mantle, elevating pore pressures artesianally in one region to failure and subsequently creating a larger scale failure. The measured pore pressure, reported as its ratio to the overlying soil thickness times the unit weight of water (the peak value of which was 0.75 and coincided near a presumed initiating region), did not reach the local slope-normal stress (corresponding approximately to a ratio of 1 for the nominal slope angle and typical bulk soil weight). Furthermore, the pore pressures over what would eventually be the failure surface were generally much less than the peak value.

With respect to the scenarios above, we will explore whether a slipping region may be brought to the point of unforced propagation before pore pressures reach the total slope-normal stress. Perhaps not unexpectedly, in the model examined below we will find that this is largely dependent on the distribution of pressures, and particularly, how locally peaked the distribution is. This line of work parallels that of others, who, in the interest of studying artificially induced dynamic rupture nucleation on faults with slip-weakening [Garagash et al., 2009; Garagash and Germanovich, 2011] or rate-and-state friction [McClure and Horne, 2010], examined the effect of the along-fault diffusion of an in-plane point source of constant pore pressure or fluid flux. Indeed, in some of what will follow in Section 2.5 (particularly, ruptures far from

a free surface) we take, as a starting point for landslide representation, conditions that are comparable to those for buried earth faults. First, however, we will consider in Section 2.3 conditions by which ambient pore pressures may be elevated near the point of failure, focusing on the sedimentation of submarine slopes; and in Section 2.4 we will look for sources of perturbations to the elevated pore pressure sufficient to initiate sliding.

2.3 STEADY, LONG-TIME SEDIMENTATION WITH CONSOLIDATION AND EFFECTIVE-STRESS-DEPENDENT PERMEABILITY

Given typical sedimentation rates and sediment permeabilities, pore fluid pressures beyond hydrostatic are expected and are often observed in the field [e.g., Flemings et al., 2008]. These results generally show conditions of high pore fluid pressures with depth, often with the vertical profile near to and paralleling that of total sediment weight. That effective stress may thereby become nearly independent of depth is of interest for slope stability. Particularly, while shear stress may increase with depth, frictional strength may remain approximately constant. Therefore, there is an interest in determining how shallowly this overpressure begins and what is its magnitude. In the following, we perform a simplified consolidation-sedimentation analysis to estimate near-seafloor conditions.

We assume that the solid sediment particles and pore fluid are much less compressible than the sediment matrix under drained conditions, and that all compaction occurs in the downward, slope-perpendicular direction, z . Where q is the flux of pore fluid in the sediment and ϵ is the slope-perpendicular extensional strain, the conser-

vation of fluid mass reduces to a conservation of fluid volume

$$\frac{\partial q(z, t)}{\partial z} + \frac{\partial \epsilon(z, t)}{\partial t} = 0 \quad (2.3)$$

Additionally, the compaction rate of the sediment matrix is proportional to the rate of the effective stress $\sigma'(z, t)$ (positive in compression),

$$\frac{\partial \epsilon(z, t)}{\partial t} = -m_v \frac{\partial [\sigma(z, t) - u(z, t)]}{\partial t} \quad (2.4)$$

where $\sigma(z, t)$ is the total normal stress, $u(z, t) = p(z, t) - p_h(z)$ is the pore pressure in excess of hydrostatic, and m_v is the compressibility of the sediment under 1D consolidation conditions (strain only in z). Finally, the fluid flux q is assumed to follow Darcy's law $q(z, t) = -(k/\mu_f)\partial u(z, t)/\partial z$, where k is the permeability of the sediment (initially assumed constant here), and μ_f is the viscosity of the permeating fluid. Combining the above equations, we arrive to

$$c_v \frac{\partial^2 u(z, t)}{\partial z^2} = -\frac{\partial [\sigma(z, t) - u(z, t)]}{\partial t}$$

where $c_v \equiv k/\mu_f m_v$ is the hydraulic diffusivity.

Considering the moving-boundary problem of seafloor that aggrades uniformly with a sedimentation rate R_s , we take time derivatives in a co-moving reference, where the origin of the coordinate z rises with the seafloor. Specifically, we replace $\partial[\sigma(z, t) - u(z, t)]/\partial t$ above with $D[\sigma(z, t) - p(z, t)]/Dt$ where $D(\cdot)/Dt = \partial(\cdot)/\partial t - R_s \partial(\cdot)/\partial z$. Looking for steady-state solutions under constant sedimentation R_s , such that local

time derivatives vanish, the above reduces to an ordinary differential equation

$$c_v \frac{d^2 u(z)}{dz^2} + R_s \frac{du(z)}{dz} = R_s \gamma \quad (2.5)$$

where $R_s \partial(\sigma - p_h)/\partial z = R_s \gamma$ and $\gamma = (\gamma_b - \gamma_w) \cos \theta$ is the slope-perpendicular component of the buoyant weight, where $\gamma_b = \rho_b g$ is the specific weight of sediment with bulk density ρ_b under gravity g (typically, $\gamma_b \approx 1.5 - 2\gamma_w$, with γ_w the specific weight of water). Taking $\bar{z} \equiv z/(c_v/R_s)$, and $\bar{u} \equiv u/(c_v \gamma / R_s)$, the nondimensional equation and general solution satisfying $\bar{u} = 0$ at $\bar{z} = 0$ are

$$\frac{d^2 \bar{u}(\bar{z})}{d\bar{z}^2} + \frac{d\bar{u}(\bar{z})}{d\bar{z}} = 1 , \quad \bar{u}(\bar{z}) = \bar{z} - C(1 - e^{-\bar{z}}) \quad (2.6)$$

where $0 \leq C \leq 1$ is a constant chosen to satisfy an imposed condition $1 \geq d\bar{u}(0)/d\bar{z} \geq 0$. For a hydrostatic pore pressure gradient as \bar{z} approaches the seafloor, $C = 1$.

The above may be considered as a long-time solution of the steady sedimentation problem treated by Gibson [1958] (i.e., the base of the sedimentary basin is considered much farther than the depths of interest). The above result would suggest that the effective stress $\sigma'(z) = \gamma z - u(z)$ becomes constant at a depth of the order c_v/R_s , beyond which the pore pressure follows lithostatic stress. However for a typical range sedimentation rates ($R_s = 0.01-10$ mm/yr) and diffusivities ($c_v = 10^{-6}$ to 10^{-8} m²/s, smaller values typical for deeper sediments) of fine-grained submarine sediments, that depth to constant effective stress (and consequently, constant strength) has a great range of values of depths (nearly all >100 m). That would exclude the possibility of sedimentation-induced overpressure generating landslides (typically at depths <100 m).

As an improvement on the above, we no longer assume a constant, depth-independent

diffusivity and account for an acute effective-stress dependence of permeability. Specifically, the Darcy relation above is now written as

$$q(z, t) = -\frac{k[\sigma'(z, t)]}{\mu} \frac{\partial u(z, t)}{\partial z} \quad (2.7)$$

where here we take $k(\sigma') = k_o \exp(-\sigma'/\sigma^*)$, where k_o is the permeability at the seafloor, and σ^* is a parameter that sets the sensitivity to effective stress. Indications are that $\sigma^* = 0.1 - 0.5$ MPa for sediments from 30–70 m below the seafloor to a few 100 m below [Henry, 2000; Long et al., 2008] and damaged basin fault zones at km depth [Revil and Cathles, 2002], and $\sigma^* = 6$ MPa for sediments at basin-scale depths (> 1 km) [Tanikawa et al., 2008].

In this case, the equation governing the excess pore pressure resembles that above,

$$e^{-A(\bar{z}-\bar{u})} \left\{ -A \left[1 - \frac{d\bar{u}(\bar{z})}{d\bar{z}} \right] \frac{d\bar{u}(\bar{z})}{d\bar{z}} + \frac{d^2\bar{u}(\bar{z})}{d\bar{z}^2} \right\} + \frac{d\bar{u}(\bar{z})}{d\bar{z}} = 1 \quad (2.8)$$

now with additional nonlinear terms moderated by the nondimensional group $A \equiv c_v^o \gamma / R_s \sigma^*$, which compares typical near-seafloor pressures to the stress-sensitivity of the permeability, and for which $c_v^o \equiv k_o / \mu m_v$. Solving the equation numerically for increasing values of A , the depth to constant effective stress is reduced when compared to the previous assumption of constant permeability (when c_v of the constant permeability case corresponds to c_v^o for comparison).

As a simple case study, we consider a shallow-water (~ 20 m) location on the southern shelf of the Mississippi River delta that was the site of two independent sets of pore pressure measurements within six years and a few hundred meters of each other [Bennett et al., 1982; Prindle and Lopez, 1983]. The trend of the observations is for the pore pressure to track the lithostatic stress beginning at a depth of approximately 6

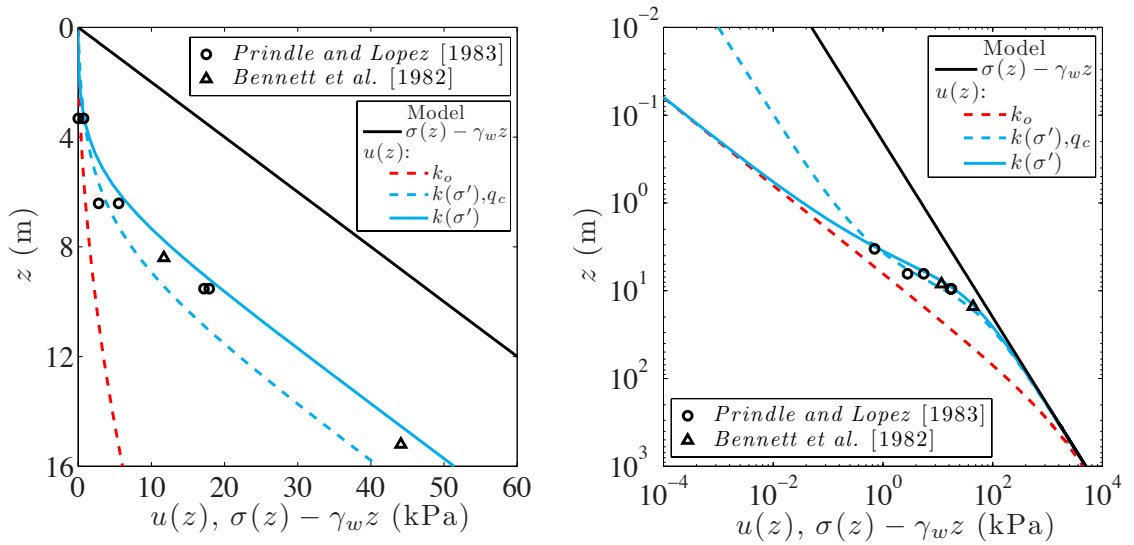


Figure 2.1: Comparison of pore pressure in excess of hydrostatic, $u(z)$, determined by separate measurements on the southern shelf of the Mississippi delta (points) and by models representing steady sedimentation (colored lines). Models treat permeability either as a constant (dashed red) or as an exponentially decreasing function of effective stress (blue). Two of the models are direct solutions of steady sedimentation-consolidation problems with a hydrostatic pore-pressure gradient at the seafloor while the third (dashed blue) is the solution to a problem of constant flow q_c (hence its departure at shallow depths). Total normal stress of model (black) plotted for comparison.

m (Figure 2.1). Assuming a hydrostatic pore pressure gradient at the seafloor, we find good agreement with the observations and the model posed by (2.8) taking $\gamma = 0.5\gamma_w$, $c_v^o = 10^{-7} \text{ m}^2/\text{s}$, $\sigma^* = 0.01 \text{ MPa}$, and $R_s = 10^{-9} \text{ m/s}$ ($\sim 30 \text{ mm/yr}$), which is of the order of rates measured in regions of the shallow western shelf [Corbett et al., 2006]. The data is not well fit by the solution (2.6) for permeability fixed at the seafloor value k_o (Figure 2.1), neither when allowing for a variation from the material properties and rates chosen above (not shown). Interestingly, the σ^* used here for the upper 20 m of near-shore sediments is an order smaller than that suggested for accretionary prism sediments at depths of several hundred meters and basin sediments on the Gulf of Mexico continental slope. While the inference of σ^* from the shallow pore pressure data may seem anomalous, perhaps due to the unaccounted for presence of biogenic gas, its order of magnitude is consistent with studies on terrestrial clays. Potts et al. [1997] arrange a compilation of prior laboratory and field tests on the overconsolidated London and Upper Lias clays as a plot of permeability with depth showing a three order of magnitude change over 20 m. Assuming the effective-stress gradient at the past maximum pressure to be anywhere from hydrostatic (γ_w) to lithostatic ($2\gamma_w$) and, as a coarse estimate, that past unloading and weathering resulted in negligible change in the gradient of permeability with depth, yields $\sigma^* = 0.03\text{--}0.06 \text{ MPa}$.

A solution approximate to this steady-sedimentation model could have been arrived at analytically by examining the case of steady seafloor-driven flow q_c (positive towards the seafloor) under a permeability that decreased exponentially with effective stress. Under these conditions

$$q_c = \frac{k[\sigma'(z)]}{\mu} \frac{du(z)}{dz} = -\frac{k[\sigma'(z)]}{\mu} \left(\frac{d\sigma'(z)}{dz} - \gamma \right) \quad (2.9)$$

which is an ordinary differential equation for σ' whose nondimensional solution [Rice,

1992] is

$$u(z) = \gamma z + \sigma^* \ln [\alpha + (1 - \alpha)e^{-\gamma z / \sigma^*}] \quad (2.10)$$

where $\alpha = q_c \mu / (\gamma k_o)$. For $\sigma^* = 0.01 \text{ MPa}$ and $\alpha = 1/50$ we find a reasonable approximation to the steady-sedimentation solution in Figure 2.1. For $\mu_f \approx 10^{-3} \text{ Pa}\cdot\text{s}$, $k_o = 10^{-15} \text{ m}^2$, and $\gamma = 0.5\gamma_w$, this implies $q_c = R_s/10 \approx 3 \text{ mm/yr}$ for the high sedimentation rate R_s chosen for steady sedimentation solutions in Figure 2.1. This flow rate is not unreasonable for the regime and may be an *a posteriori* choice.

Using the two-dimensional steady sedimentation/consolidation model, we apply it to estimate conditions on the continental slope. We assume a slightly lower sedimentation rate, but choose a value that is relatively high for continental slope sites, $R = 10 \text{ mm/yr}$. We assume a range of possible seafloor values of the coefficient of consolidation, $c_v^o = 10^{-5}$ to $10^{-8} \text{ m}^2/\text{s}$, and a conservative $\sigma^* = 0.25 \text{ MPa}$. We calculate the steady pore pressure distribution with depth, $p(z) = \gamma_w z + u(z)$ with $u(z)$ being the solution to (2.8); and we estimate a factor of safety that is the ratio of a frictional strength (taken as $\tau_{max}(z) = f_p[\sigma(z) - p(z)]$ with $f_p = 0.5$) to the shear stress $\tau(z) = (\gamma_b - \gamma_w) \sin \theta$. The shallowest depth to failure of a 4° slope is approximately 100 m (taking $\gamma_b - \gamma_w = 10 \text{ kPa}$ in this depth range) with the factor of safety being as low as 2 for half the depth of failure. While the depth of failure is shallower than predicted by a constant-permeability model using the near-seafloor permeability alone, it is comparatively deep relative to commonly observed landslides and would require long periods of high (10 mm/yr) sedimentation. This indicates that even with efficient overpressure by permeability reduction, failure of sediments on continental slopes by fast sedimentation alone may not be likely. In the subsequent section, we examine how perturbations to such elevated pore pressures may create a local failure.

2.4 SOURCES OF LOCAL INCREASES IN PORE PRESSURE ON SEAFLOOR

Localized pore pressures near the seafloor may be brought about by high-permeability pathways that facilitate the drainage of a compacting basin. The pathways may take the form of faults, or even inclined coarse-grained turbidite deposits on buried paleocanyons, and are often expressed as depressions on the seafloor [e.g., Gay et al., 2007]. Dugan and Flemings [2000] quantify potential pore pressure changes with a two-dimensional sedimentation-consolidation calculation of a nonuniform sedimentation scenario. A resulting high permeability conduit may elevate near-seafloor pore pressures to lithostatic stresses at a site with known failures. Such channelized flow may sufficiently elevate pore pressures to create liquefied sediments, like those retrieved from a deepwater core of a pockmark above an apparent fluid chimney [Gay et al., 2006]. In this instance, the 800 m-wide pockmark appeared on seismic data as the seafloor expression of a vertical fluid seep rooted in a buried paleochannel. The pore pressure path followed by the buoyant rise of fluids pressurized at depth would likely meet liquefaction conditions well below the seafloor, as shown by surface and subsurface disturbances induced by biogenic or thermogenic gas seeps [e.g., Pinet et al., 2008].

Methane hydrates may present an alternative source of quasi-statically elevated pore pressures. Implications in landsliding are driven by the coincidence of some continental slope landslide regions with gas hydrate [e.g., Kayen and Lee, 1991]. The pore pressures may come directly from hydrate decomposition, or by indirect pressurization. The excess pore pressures generated by hydrate dissociation are generally large, even when considering fluid flux and finite dissociation rates. Dissociation at the base of the stability zone by sedimentation burial, uplift, or sealevel drop, may be more than sufficient to meet a shear-strength criterion [Xu and Germanovich, 2006].

However, the base of the stability zone is often greater than 200 m below the seafloor [Haacke et al., 2007], and would imply relatively deep-seated large landslides. More favorably to landsliding, gas plumes may indicate hydrate decomposition at shallower depths along the upslope stability limit [Westbrook et al., 2009]. However, the pore pressure calculations of Xu and Germanovich [2006] indicate that levels may even exceed lithostatic stresses, which may create features of vertical fluid expulsion or sediment disturbance, like those observed in seismic data by Berndt et al. [2005] over lengths of 1–10 km coinciding with a landslide scarp. They propose that high dissociation rates accompanying the rapid erosion resulted in observed subsidence by fluid expulsion with fluidization of a finite thickness of overlying sediments, implying that pore pressures were elevated near lithostatic stresses at least 50-100m above the dissociated region over kilometer lengthscales. The loss of matrix support by hydrate dissolution or decomposition, and subsequent underconsolidation, has also been proposed to elevate pore pressures broadly at the stability base [Kvenvolden, 1993]. Sultan et al. [2010] advocated similar underconsolidation at shallower depths to explain the apparent progression of pockmark formation through observed morphological stages; there underconsolidation was presumed result from focused flow from depth carrying a transient supply of methane that stimulated first hydrate growth before dissolution.

The overpressure by gas accumulation at the base of the stability zone has often been cited as being sufficient to drive an invasive flow to the seafloor expressed as seafloor pockmarks and pipes [Bünz et al., 2003; Flemings et al., 2003; Gay et al., 2007; Liu and Flemings, 2007; Cathles et al., 2010], as well as by conduits created by induced normal faulting [Hornbach et al., 2004]. The elevated pore pressures en route to the surface may be sufficient to create liquefied sediments, like that for the cold

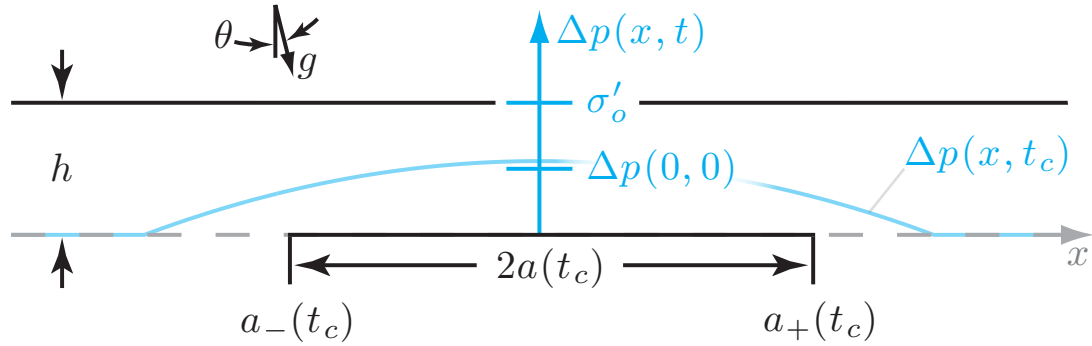


Figure 2.2: Superposition of a peaked pore pressure profile along a depth h (blue) on an illustration of a slipping region that parallels a slope surface (both black). The profile shown corresponds precisely to that which would generate the illustrated slipping region. The slipping region is enlarged by a gradual increase of pore pressure $\Delta p(x, t)$ to a critical extent, illustrated here at $t = t_c$, beyond which its growth may continue without any further pressure increase. The value $\Delta p(0, 0) = \sigma'_o - \tau_o/f_p$ is that at which a failure criterion is first met and sliding is initiated at the origin. A frictional length scale ℓ is used to denote relative depth by $H \equiv \sqrt{h/\ell}$. Here $\tau_o/\sigma'_o = 0.25$ and $f_p = 0.5$ (i.e., $\Delta p(0, 0) = 0.5\sigma'_o$), $H = 0.5$, and $K_{h\ell} = 1$ is the dimensionless profile curvature defined in text. Interestingly, in the case considered here, only a marginal increase past $\Delta p(0, 0)$ is required to bring the slope to the critical point.

seeps discussed above (as in the formation of pockmarks). Pockmark size can then be an indication of pore pressure distributions (whether sourced in hydrates or not) and range from a few tens of meters [e.g., in shallow water; Andrews et al., 2010] to kilometer lengthscales [e.g., on the continental slope; Sultan et al., 2010].

2.5 RUPTURE NUCLEATION BY LOCAL INCREASES IN PORE PRESSURE

Before local pore pressure increases begin, we assume that there is a constant shear stress τ_o , total normal stress σ_o (positive in compression), and pore pressure p_o acting along the depth of the future slip surface. The shear and total normal stress may be those of an infinite slope and in the submarine case, the initial pore pressure may correspond to that calculated in Section 2.3 at a particular depth $z = h$. The initial effective normal stress is then $\sigma'_o = \sigma_o - p_o$.

Given the variety of means to increase pore pressures, as a first step we simplify the form that a pore pressure increase takes. The purpose is to isolate the first-order characteristics, namely, the magnitude of the increase and its distribution in space. The simplified distribution is locally peaked and increases uniformly in space at a constant rate R . The amount the pore pressure falls with distance from the peak is given by a function $q(x)$. The pore pressure begins to elevate from p_o and we are first interested at the point of time when slip is initiated. For a peak friction coefficient f_p , failure will first occur when $\Delta p = \sigma'_o - \tau_o/f_p$. We take this point in time to be $t = 0$. This defines the pore pressure increase as

$$\Delta p(x, t) = [\sigma'_o - \tau_o/f_p] + Rt - q(x) \quad (2.11)$$

at x for which (2.11) is positive, with $\Delta p(x, t) = 0$ otherwise. We take a simple

symmetric function $q(x) = \kappa x^2/2$ whose single parameter $\kappa > 0$ is the sharpness of the pore pressure increase. The peak magnitude of the pore pressure is given by the nondimensional parameter

$$T \equiv \frac{f_p}{\tau_o} R t \quad (2.12)$$

$T = 0$ when slip initiates at $t = 0$ (and $x = 0$) and $T = 1$ some time later when the pore pressure reaches the total slope-normal stress ($p = \sigma_o$) at $x = 0$.

For failure to initiate at a depth 20 m below the seafloor of a 3° slope under initially hydrostatic conditions, the point of first failure ($T = 0$) corresponds to a pore pressure of approximately 90 KPa. This pore pressure represents 90% of the effective initial overburden (100KPa, corresponding to $T = 1$). For comparison, for failure to initiate at a depth 5 m below the earth surface of a 20° slope under dry, subaerial conditions, point of first failure corresponds to a pore pressure of 25 KPa ($T = 0$), representing $\sim 25\%$ of the slope-normal stress (95 KPa, $T = 1$).

Slip is presumed to start at a depth $z = h$ (in the coordinate of Section 2.3), along a surface running parallel to the seafloor or Earth's surface (Figure 2.2). The mode of failure examined here is solely the accumulation and propagation of slip: i.e., we do not consider additional modes as might occur, for instance, at pore pressures approaching the total overburden. Here, the failure surface is predetermined, as may be dictated by natural stratification or boundaries.

We take the friction coefficient at a point on that surface to weaken linearly with slip δ from a peak value f_p to a residual value f_r after slipping an amount δ_c . For slip $\delta < \delta_c$,

$$f(\delta) = f_p - w\delta \quad (2.13)$$

where $w = (f_p - f_r)/\delta_c$. The dimensionless variable for slip is $\bar{\delta} \equiv \delta w/f_p$, which

may range between 0 when $f = f_p$ and 1 when $f = 0$ (the lowest possible value for f_r). For overconsolidated sediments, f_p , f_r , and δ_c may be estimated from the ring shear experiments of *Bishop et al.* [1971]. For the London Brown and Blue Clays sampled, friction drops from $f_p = 0.45$ to $f_r = 0.2\text{--}0.25$. The friction coefficient does not strictly follow a linear drop to residual value, but the initial linear slip-weakening rates are $w = 0.08\text{--}0.3/\text{cm}$. Normally consolidated sediments may also weaken with slip and have comparable weakening rates. This is the case if we presume that the initial decrease in friction of 1) an aged, normally consolidated soil is comparable to the decrease in friction of 2) a overconsolidated clay that has a) been sheared to a residual friction and b) been allowed to regain some strength under fixed displacement. While the strength gain is time dependent, for experiments on 2) with healing times of 100–200 days the drop in friction coefficient with slip is low ($f_p - f_r \approx 0.05$), but occurs over smaller displacements, with initial slip-weakening rates in the range $w = 0.3\text{--}0.8/\text{cm}$ [*Stark et al.*, 2005; *Carrubba and Del Fabro*, 2008; and *Stark and Hussain*, 2010]. A freshly sedimented seafloor, like that presented in Section 2.3 with accumulation rates of the order of 1 mm/yr, would represent a potentially well aged, normally consolidated slope. However, if erosion and prior landslide events remove material, then the uncovered seafloor will be effectively overconsolidated.

The slip weakening introduces a length scale

$$\ell^* \equiv \frac{\mu^*}{\sigma'_o w} \equiv \frac{\mu^* \delta_c}{\tau_p - \tau_r} \quad (2.14)$$

like that in (2.2), where here $\tau_{p/r} = f_{p/r} \sigma'_o$ are nominal peak and residual strengths. We estimate ℓ^* under two conditions: a subaerial slope and a submarine one. In subaerial conditions, we presume failure occurs 5 m below the surface and estimate the initial effective normal stress as that of an infinite slope, $\sigma'_o = \gamma_b z \cos \theta$, with

a slope of $\theta = 30^\circ$, and a typical sediment unit weight $\gamma_b \approx 2\gamma_w$. For submarine conditions, we presume failure occurs 20 m below the seafloor and take hydrostatic conditions where $\sigma'_o = (\gamma_b - \gamma_w)z \cos \theta$, with a slope of $\theta = 3^\circ$, and the sediment unit weight $\gamma_b \approx 1.5\gamma_w$. The sediment's elastic stiffness is perhaps the most variable quantity, and we consider that the shear modulus μ may range between 10–100 MPa, with $\nu = 1/3$ (corresponding to shear wave speeds of a few hundred meters per second; and $\mu^* = 15 - 150$ MPa for mode-II deformation). This yields similar estimates for ℓ^* in both cases: $\ell^* = 16 - 160$ m for subaerial conditions, and $\ell^* = 15 - 150$ m for submarine conditions.

2.5.1 NUCLEATION FAR FROM A FREE SURFACE

Here we assume that the slipping length at nucleation is much shorter than the depth h below the free surface. In this case, the shear stress along the plane of the slip surface is, for a linearly elastic material [e.g., Bilby and Eshelby, 1968],

$$\tau(x, t) = \tau_o - \frac{\mu^*}{2\pi} \int_{a_-(t)}^{a_+(t)} \frac{\partial \delta(\xi, t)/\partial \xi}{x - \xi} d\xi \quad (2.15)$$

where a_+ and a_- are the endpoints of the slipping region (Figure 2.2). Over the slipping region this shear stress must meet the strength requirement

$$\tau(x, t) = [f_p - w\delta(x, t)] [\sigma'_o - \Delta p(x, t)] \quad (2.16)$$

with the prefactor replaced by f_r once slip exceeds δ_c . In this subsection we will assume that f_r is not yet engaged and will address this case in the following subsection.

In this “deep” context and for profiles of this type, a more convenient lengthscale

is

$$\ell \equiv \ell^* \frac{\tau_p}{\tau_o} \equiv \frac{f_p \mu^*}{\tau_o w} \quad (2.17)$$

The ratio ℓ/ℓ^* can be estimated assuming infinite slope conditions where either $\tau_o/\sigma'_o > \tan \theta$ when pore pressure is in excess of hydrostatic or $\tau_o/\sigma'_o = \tan \theta$ for “dry” subaerial slopes or submerged slopes with hydrostatic pressure distributions. For the last set of cases and $f_p = 0.5$, $\tau_o/\tau_p \approx 0.1 - 0.7$ for $\theta = 3^\circ - 20^\circ$, meaning that ℓ for low-angle, deepwater continental slopes is nearly an order larger than that for steeper subaerial counterparts.

It is the length ℓ with which rupture tip lengths are accordingly nondimensionalized to an average length $\bar{a}(t) \equiv [a_+(t) - a_-(t)]/2\ell$, with an asymmetry measure $\bar{b}(t) \equiv [a_+(t) + a_-(t)]/2\ell$, and also with which distance is normalized to $\bar{x}_o \equiv x/\ell - \bar{b}(t)$. For the symmetric increase (2.11), $b(t) = 0$.

The curvature of the pore pressure nondimensionalizes to

$$K \equiv \frac{f_p}{\tau_o} \kappa \ell^2 \quad (2.18)$$

The convenience of the above scaling is that the profile is solely described by parameters T and K , so long as the endpoints of the crack are within the curved portion of the pore pressure profile (as in Figure 2.2). This is reasonably assumed to be the case in this subsection. (Another parameter, $\tau_o/\tau_p \equiv \tau_o/(f_p \sigma'_o)$, determines the location where $\Delta p(x, t) = 0$; its role is highlighted in the following subsection.) Subsumed in the definition of K is the slope angle (implicitly, via τ_o). As a result, $K \sim 1/\sin^3 \theta$, implying that shallow slopes are more likely to have a large K for a wide range of dimensional curvatures κ and we will examine the consequence of this in the results that follow.

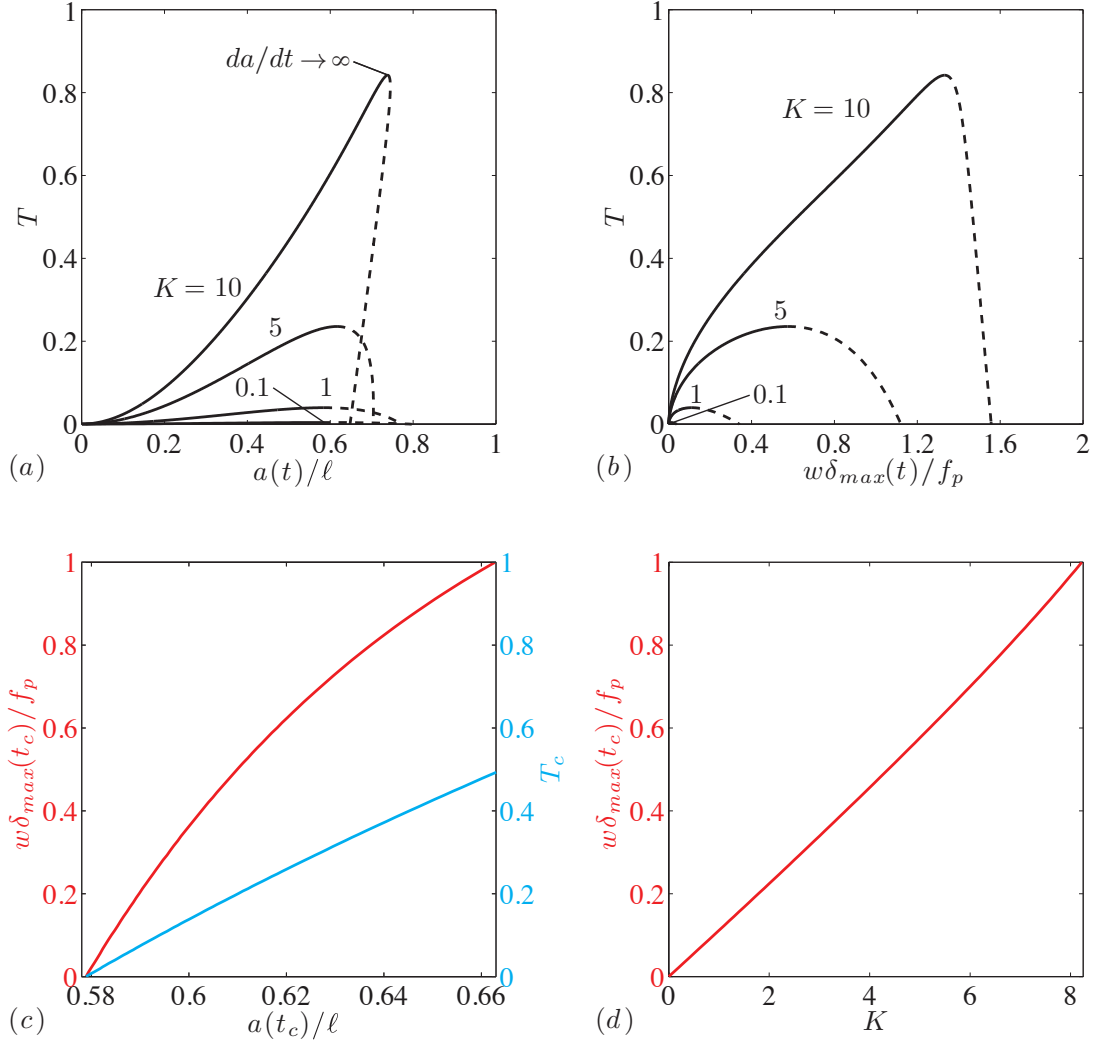


Figure 2.3: (a) Enlargement of crack length $a(t)$ with increasing pore pressure Rt , nondimensionally as T , for profiles of pore pressure with various curvatures κ , nondimensionally as K . (b) Plot of maximum slip $\delta_{max}(t)$, occurring at $x = 0$, against pore pressure increase. The nucleation of a dynamic rupture occurs at the peak of the loading paths and the crack propagates without any further increase in pore pressure. (c) Plot of peak slip (red) and pore pressure increase (blue) against the crack length at the point of nucleation. (d) Plot of peak slip at nucleation against the nondimensional profile curvature. These analyses assume that $f_r/f_p < (1 - w\delta_{max}/f_p)$, implying that solutions with $w\delta_{max}/f_p > 1$ are unphysical.

For a given curvature K , the slip distribution is solved at each stage of the pore pressure increase (T) using a Gauss-Chebyshev quadrature collocation technique (Appendix A.2). The peak slip (located at the crack center for this symmetric loading scenario) and crack length are presented in Figure 2.3. Each path corresponds to a pore pressure increase with a fixed curvature. A common feature of all the paths is the tendency for greater growth of the crack half-length $a(t)$ and peak slip $\delta_{max(t)}$ in response to a given increment of the pore pressure as the increase progresses. Eventually a point is reached where the growth rates of these quantities are unbounded (and continuation of the quasi-static solutions requires a *decrease* in pore pressure). Where the rates become unbounded (a time labeled $t = t_c$) marks the onset of the nucleation of dynamic rupture: i.e., once the pore pressure reaches the peak levels in Figure 2.3, rupture may continue to propagate as an accelerating rupture, without any further increase in pore pressure, driven by frictional weakening. The elastodynamic ruptures are expected to accelerate to a limiting speed of the order of the shear-wave speed (for sediments, typically of the order of 100 m/s).

In the limit of very broad curvatures ($K \rightarrow 0$), the quasi-static problem reduces to an eigenvalue problem like that of Uenishi and Rice [2003]. The limit of the eigenvalue problem $(a(t_c)/\ell \approx 0.579$; Appendix A.1.1) is met by the numerical solutions for small K . Such broad curvatures induce sliding over a large region for only small increases in pore pressure past that which would first start sliding at the origin ($T = 0$), and the critical increase T_c and peak slip $\delta_{max}(t_c)$ are very small. In contrast are the sharper loading profiles $K = 1, 5$ that require more substantial pore pressure increases to reach the point of nucleation, accumulating much more slip in the process.

We recall that slip is nondimensionalized such that the friction coefficient is $f = (1 - \bar{\delta})f_p$. At the nucleation point corresponding to the case $K = 5$ in Figure 2.3, the

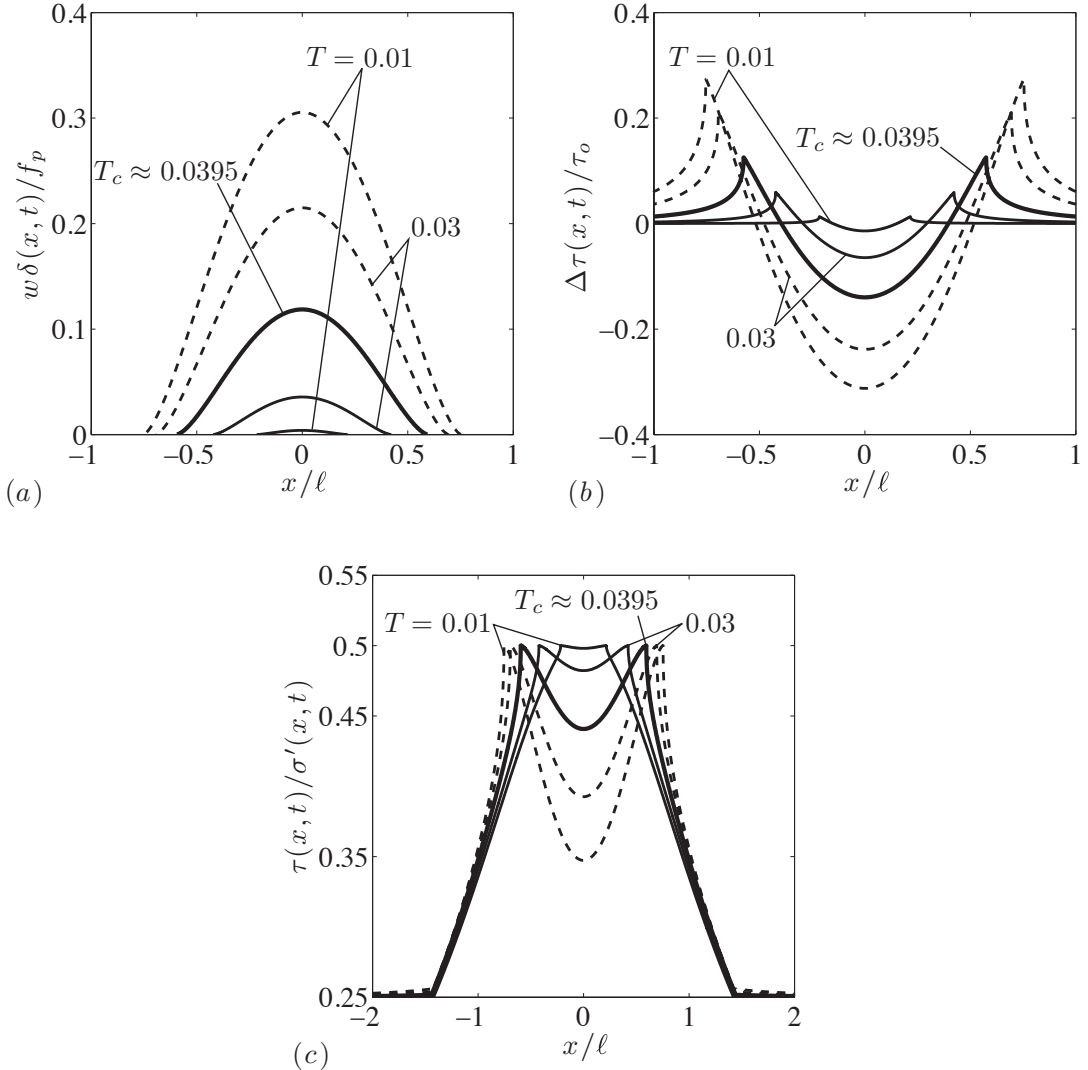


Figure 2.4: Distribution of (a) slip and (b) shear stress change for various levels of pore pressure increase $T \equiv Rtf_p/\tau_o$ and fixed curvature $K \equiv f_p\kappa\ell^2/\tau_o = 1$. (c) Ratio of shear stress to effective normal stress for $f_p = 0.6$ and $\tau_o/\sigma'_o = 0.3$. Solid curves are those distributions originating from a nucleated crack of zero length to an unstable limit (bold), dashed curves are unstable distributions beyond the point of nucleation.

friction coefficient at the center of the crack has been reduced to $f \approx 0.4f_p$. For the loading history corresponding to the sharper profile ($K = 10$), we see that so much slip accumulates that nucleation ultimately occurs for $\bar{\delta}_{max} > 1$, and the result can be dismissed as an unphysical representation (i.e., $f < 0$). However, had we imposed a residual friction, say $f_r/f_p = 0.2$, on the case $K = 10$, pore pressures reach the total slope-normal stress ($T = 1$) before nucleation occurs (case not shown). Therefore, determining the relative sharpness of a profile is important for determining if modes of failure other than pure slip can be expected (i.e., if $T = 1$ is reached), as well as the total amount of slip before dynamic rupture. Figures 2.3c,d show conditions at nucleation over a broad range of curvatures. Most remarkably, the critical length at nucleation is relatively insensitive to the profile curvature, although the accrued slip may vary widely.

Figure 2.4 takes snapshots along the depth $z = h$ at fixed points in time for the load path of the case $K = 1$ of Figure 2.3. Figure 2.4a shows the distribution of slip up to the point of nucleation (solid lines), followed by the physically unattainable, post-peak solutions (dashed lines). The approach of nucleation is noticeable in that a modest increase of pore pressure results in a significant growth of the rupture tips and of the amount of slip. Figure 2.4b shows comparable plots for the shear stress. Plotting its ratio with the effective normal stress in Figure 2.4c shows the weakening of the friction coefficient from its peak value (here arbitrarily chosen to be $f_p = 0.5$). The overall peaked structure of Figure 2.4c is owed to the peaked distribution of the pore pressure increase.

From this analysis, the most unstable form of loading is a broad increase in pore pressure, in the sense that loadings of this type require the lowest peak pore pressure and result in the shortest critical lengths (as well as the least amount of slip at nucle-

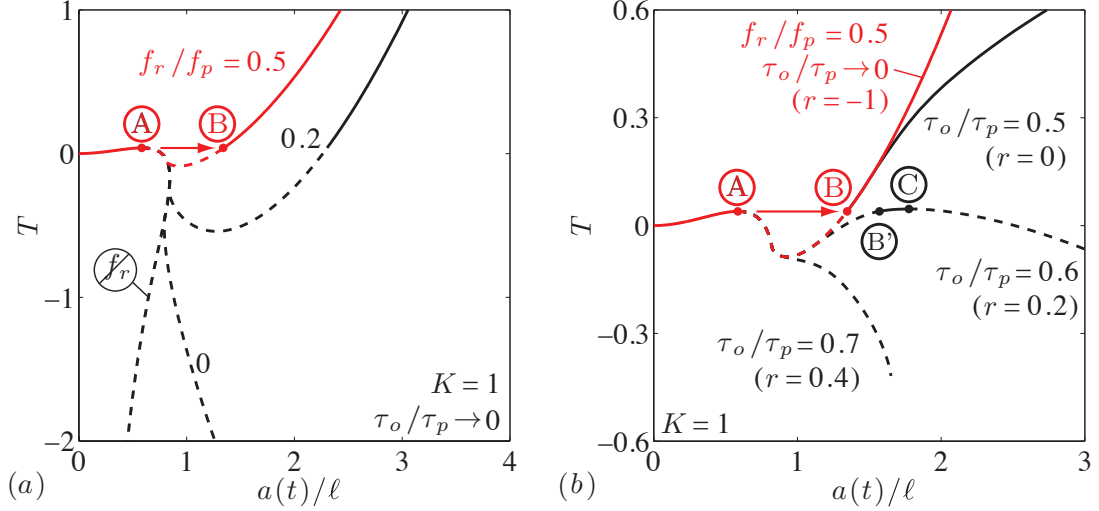


Figure 2.5: Solutions of crack length $a(t)$ with increase in pore pressure T at a fixed curvature $K = 1$. Solid and dashed lines represent stable and unstable quasistatic solutions. (a) Solutions for variable f_r/f_p , and the solution neglecting residual friction. In these solutions the shear stress is small (low τ_o/τ_p). Starting with the solution of (a), $f_r/f_p = 0.5$ (red), the solutions in (b) show the result of increasing shear stress τ_o/τ_p (black).

ation). Given that μ^* is larger in mode II than in mode III, rupture growth in mode III will reach its critical value sooner than in mode II, provided pore pressure increases have approximately equal distribution in the along-slope and across-slope directions. Additionally, for sharper pore pressure increases, the trend of their unstable points is towards the point where frictional strength of the interface is lost ($T = 1$). While our model is limited to $T < 1$, we will later briefly discuss potential modes of failure once $T = 1$.

2.5.2 RESIDUAL FRICTION AND DYNAMIC RUPTURE ARREST IMPLICATIONS

A residual friction coefficient f_r , typically a moderate fraction of f_p , is engaged at a slip of δ_c and such a cutoff affects rupture propagation. If the initial shear stress is sufficiently low such that $\tau_o < f_r\sigma'_o (\equiv \tau_r)$ and rupture is initiated with relatively

little slip with respect to δ_c (e.g., for low K) one may expect the rupture to reach instability and proceed dynamically. However, one would also expect the rupture to arrest as sufficient slip accumulates such that the strength approaches its residual value. *Garagash and Germanovich* [private communication, 2010] observed such a potential for dynamic rupture arrest for their in-plane point-source loading scenario. Furthermore, dynamic rupture may potentially be reinitiated with further increase in pore pressure when $\tau_r < \tau_o < \tau_p (\equiv f_p \sigma'_o)$.

Figure 2.5a continues solutions of Figure 2.3 now considering the possibility that slip may exceed the slip weakening distance δ_c , engaging residual friction. The solutions shown are those for slopes with very little initial shear stress, as may be the case for very shallow slope angles (low τ_o/τ_p). Under these low slope angles, the gravitational shear stress would be insufficient to drive a rupture at a nominal residual strength $\tau_r = f_r \sigma'_o$. Not surprisingly then we find that the dynamic rupture arrests once it has progressed away from the peak in pore pressure into a region that is closer to the ambient effective normal stress σ'_o . The dynamic rupture initiation and arrest are marked for the particular case $f_r/f_p = 0.5$ by the points (A) and (B), respectively. The arrest lengths are longer for lower residual strengths, f_r/f_p . Continued quasistatic slip and growth of the rupture is possible after arrest. However, this requires continued pore pressure increases that eventually would require reaching the slope-normal stress. (Also shown are unphysical solutions when a residual friction is neglected and friction is allowed to follow the linear slip-weakening path into the negative range.)

Not all ruptures will arrest and Figure 2.5b shows the effect of increasing the slope angle. Continuing with the solution for $f_r/f_p = 0.5$ in red of Figure 2.5a, we increase

the background shear stress τ_o , which is measured using a prestress ratio

$$r \equiv \frac{\tau_o - \tau_r}{\tau_p - \tau_r} \equiv \frac{1}{1 + S} \quad (2.19)$$

(as an alternative to the commonly used S -ratio in fault rupture dynamics). Here we find that by increasing τ_o/τ_p (more specifically, r), there is a transition of ruptures that arrest (e.g., the cases $r = -1$, $r = 0$) to those that may continue to propagate dynamically once initiated ($r = 0.4$).

There is an intermediate case shown in which rupture arrests (B'), and, if pore pressures continue to increase, a second nucleation event may occur (C) at which point the rupture propagates indefinitely. The instabilities of the (C)-type occur for low, positive r . At the point (C) the friction has reached residual over much of the length of the crack. Viesca-Falguieres and Rice [2010] made use of a small-scale yielding approximation (i.e., singular crack theory with critical energy release rate $(f_p - f_r)\sigma'_o\delta_c$) to examine this behavior and found the crack length at the (C)-type instability, $a_c^{(C)}/\ell^*$, scaled as $1/(4\pi r^2)$ in the small- r limit.

Arrest may be precluded if the friction at large slip is further reduced by additional mechanisms. For deep-seated landslides undergoing rapid slip, shear heating may be sufficient to elevate temperatures for thermal pressurization or material decomposition to occur [Voight and Faust, 1982; Vardoulakis, 2002; Goren et al., 2010]. In the fault nucleation context, Garagash and Germanovich [2011] estimated the expected pressurization during the dynamic phase to effectively reduce the domain over which arrest is expected. They interestingly observe that cases where fault pressurization is marginally above that needed to induce slip may be more favorable to thermal pressurization and less likely to arrest.

2.5.3 ELASTODYNAMIC SOLUTIONS WITH RUPTURE ARREST

This predicted dynamic growth and arrest may be observed in finite-element simulations of dynamic rupture propagation in response to a sudden application of the critical pore pressure increase $\Delta p(x, t_c)$. Specifically, in place of modeling the quasi-static process of nucleation to the critical crack size followed by the dynamic growth process, an elastodynamic problem is considered with $\Delta p(x, t_c)$ as the initial condition, which is discretized over the contact surface as a position-dependent, nodal pore-pressure force. This pore-pressure force reduces the effective normal force when evaluating the frictional strength of a node. We use the finite element package ABAQUS/Explicit in a similar manner as that by Templeton and Rice [2008] and Viesca et al. [2008], except to be consistent with our quasi-static model, only considering elastic behavior away from the contact surface. (Those investigations, as well as those of Viesca and Rice [2010], considered elastic-plastic response of material outside the slip surface.)

The finite-element grid spacing is $\Delta x = \ell/50$ and the domain (discretized with four-noded plane-strain, reduced integration elements) has a height and width of $10\ell \times 20\ell$, with a split-node contact surface located at half-height and absorbing boundary conditions (“infinite” elements) along the outer boundaries. Two cases are considered for which $K = 1$ and $f_r/f_p = 0.5$: Case 1) $\tau_o/\tau_p = 0.5$, and Case 2) $\tau_o/\tau_p = 0.7$. Plots of slip at constant intervals of time, $\Delta t = \ell/c_s$ (where c_s is the shear wave speed), show the gradual growth beyond the critical crack length and the subsequent propagation. Case 1) (Figure 2.6a and b) arrests at a distance close to that estimated by the quasi-static calculation and denoted by the dashed lines. Case 2) (Figure 2.6c and d), for which the sole change is an increase in background shear stress, shows indefinite rupture propagation. Such behavior is not restricted to nucleation by pore pressure, but can also be shown to occur in nucleation by local increases in shear stress as in

Ampuero et al. [2006] and Ripperger et al. [2007]. Their studies show, that for a slip-weakening rupture nucleated by a local peak in the shear stress, net increases in a heterogeneous background shear stress (i.e., an increase in a measure comparable to r) mark a sharp transition from arresting dynamic ruptures to those that rupture the entire fault surface.

2.5.4 NUCLEATION NEAR A FREE SURFACE

To account for a rupture comparable in length to its depth below the free surface, the change in shear stress due to slip requires additional terms to the integral of (2.15)

$$\tau(x, t) = \tau_o - \frac{\mu^*}{2\pi} \int_{a_-(t)}^{a_+(t)} \frac{\partial \delta(\xi, t)}{\partial \xi} \left[\frac{1}{x - \xi} + k_1(x - \xi) \right] d\xi \quad (2.20)$$

and the strength requirement in this case is

$$\tau(x, t) = [f_p - w\delta(x, t)] [\sigma'_o + \Delta\sigma(x, t) - \Delta p(x, t)] \quad (2.21)$$

where changes in the total normal stress on the surface due to slip are

$$\Delta\sigma(x, t) = -\frac{\mu^*}{2\pi} \int_{a_-(t)}^{a_+(t)} \frac{\partial \delta(\xi, t)}{\partial \xi} k_2(x - \xi) d\xi \quad (2.22)$$

The nonsingular kernel functions $k_{1,2}(x - \xi)$ account for shear and total normal stress changes, respectively, due to slip in proximity of a free surface. When the rupture length is much less than the depth, then the contributions of those kernels are negligible and (2.20) reduces to (2.15), the standard equation for shear stress (with no normal stress change) due to a distribution of dislocations along a planar surface.

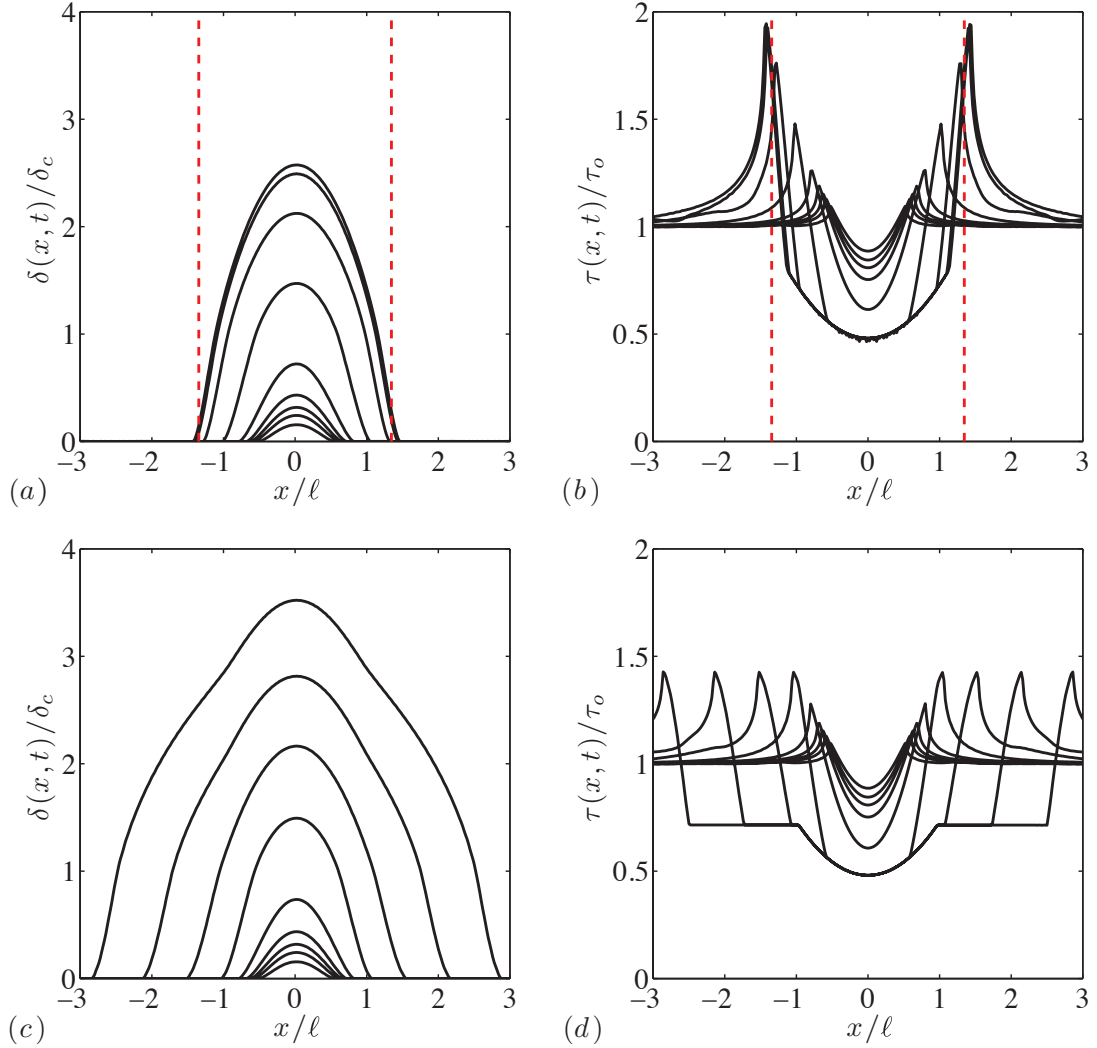


Figure 2.6: Dynamic rupture arrest (Case 1, a–b) and continuation (Case 2, c–d) as indicated by plots of slip and shear stress at time intervals of ℓ/c_s . The cases correspond to two cases of Figure 2.5b. In both cases $f_r/f_p = 0.5$, and the sole difference is an increase in shear stress from $\tau_o/\tau_p = 0.5$ for Case 1 to $\tau_o/\tau_p = 0.7$ for Case 2. Each rupture is nucleated by suddenly applying the same critical loading $\Delta p(x, t_c)$ (with profile curvature $K = 1$) as the initial condition. The dashed lines in (a–b) correspond to arrest length predicted by quasi-static solution (point (B) in Figure 2.5b).

Taking $v \equiv x - \xi$, the kernels are [e.g., Head, 1953]

$$k_1(v) \equiv \frac{-v}{4h^2 + v^2} + \frac{8h^2v}{(4h^2 + v^2)^2} + \frac{4h^2v^3 - 48h^4v}{(4h^2 + v^2)^3} \quad (2.23)$$

$$k_2(v) \equiv \frac{24h^3v^2 - 32h^5}{(4h^2 + v^2)^3} \quad (2.24)$$

For a symmetric distribution of slip near the free surface, their contribution is an antisymmetric change in normal stress and a symmetric change in the shear stress. (As summarized in Viesca and Rice [2011], misprints in early reported results for such kernels have unfortunately propagated through the literature.)

The depth h should be measured relative to a depth-independent lengthscale. This excludes ℓ (and ℓ^*), as its definition depends on τ_o (or σ'_o), which is proportional to depth for the simple infinite slope model: $\tau_o = \gamma_b h \sin \theta$. One depth-independent lengthscale is the geometric mean of frictional length ℓ and depth h

$$\sqrt{h\ell} \equiv \sqrt{\frac{\mu^* f_p}{\gamma_b \sin \theta w}} \quad (2.25)$$

which depends purely on slope orientation and material properties, which are implicitly assumed here to be independent with depth, to first approximation. This lengthscale enters naturally into shallow slope problems and are what scale the critical lengths in shallowly buried fracture analyses of slopes (e.g., l_u in Puzrin and Germanovich [2005], which corresponds to $\sqrt{4h\ell^*}$ here). The nondimensional depth is then defined as

$$H \equiv \frac{h}{\sqrt{h\ell}} \quad (2.26)$$

Estimates of H in subaerial and submarine environments yields a perhaps surprisingly narrow range, assuming similar weakening behavior in both environments when esti-

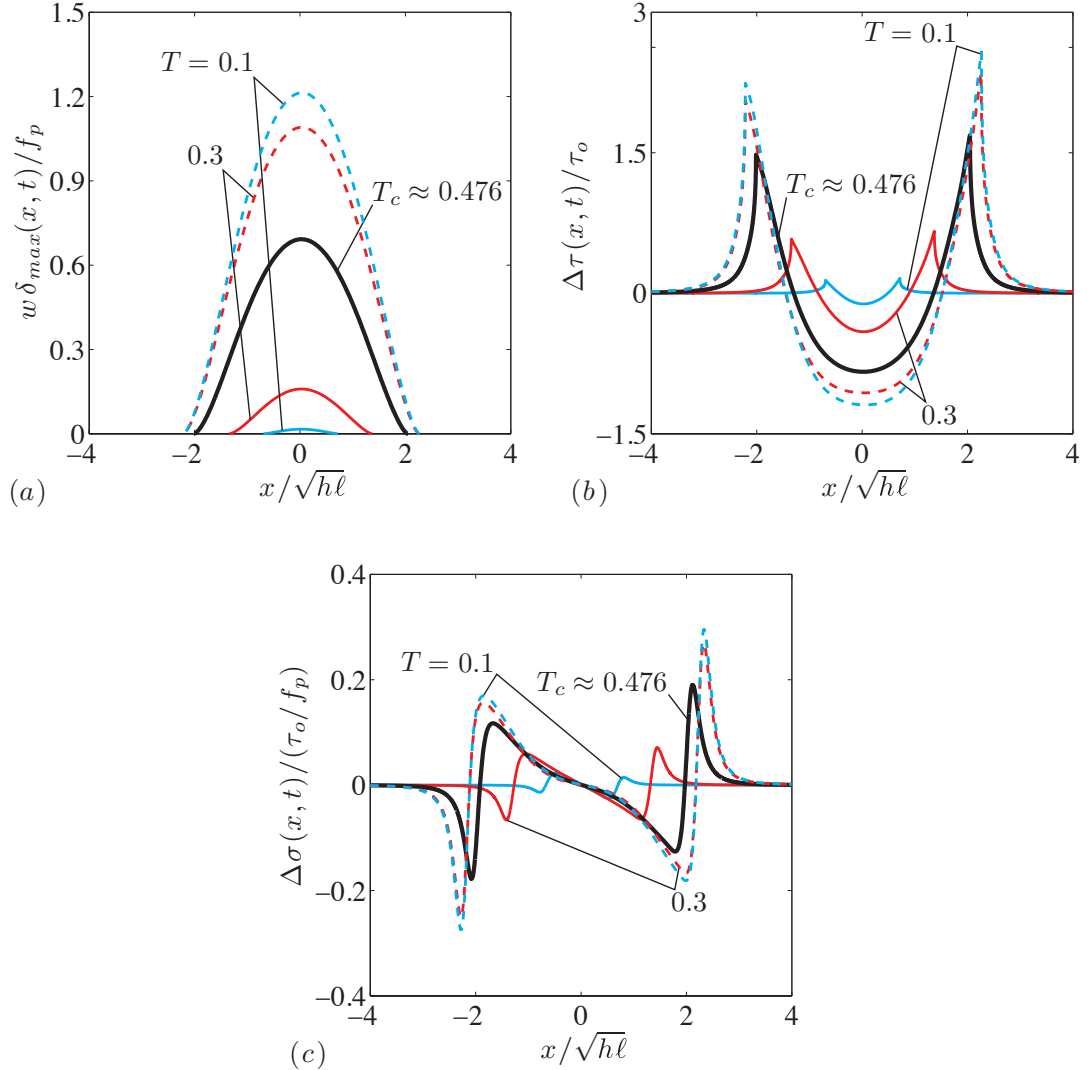


Figure 2.7: Distribution of (a) slip, (b) shear stress, and (c) total normal stress for given pore pressure increase T with a fixed curvature (normalized such that $K_{hl} \equiv f_p \kappa h \ell / \tau_o = 1$), and fixed effective depth ($H \equiv \sqrt{h/\ell} = 0.1$, such that x -axis limits are $\pm 40h$). Curves in black outline those distributions originating from a nucleated crack of zero length to an unstable limit (bold).

mating ℓ . Taking the representative scenarios used to estimate ℓ^* in Section (2.5.1), yields $\ell = 22 - 220\text{m}$ and $H = 0.15 - 0.48$ in the subaerial case and for the submarine case (hydrostatic conditions), $\ell = 140 \text{ m} - 1.4 \text{ km}$ and $H = 0.11 - 0.37$.

We look for the nucleation behavior at variable depth, with an interest in the limit of small and moderate H . We use a locally peaked pore pressure profile as in (2.11) with a spatially uniform loading at rate T , but here choose a nondimensionalization of the curvature using the depth-independent lengthscale $\sqrt{h\ell}$

$$K_{h\ell} \equiv \frac{f_p}{\tau_o} \kappa h \ell \quad (2.27)$$

Then, fixing $K_{h\ell}$, the only parameter varied is the burial depth of the sliding surface. Additionally, for the cases considered here the friction coefficient is presumed to remain on the linear portion of the slip-weakening curve (i.e., the slip remains below δ_c).

Figure 2.2 shows the geometry of the crack and the pore pressure profile at nucleation for the particular case $H = 0.5$, $K_{h\ell} = 1$, $\tau_o/\sigma'_o = 0.25$ and $f_p = 0.5$. Considering a scenario that leads to quasi-static crack lengths much longer than depth, Figure 2.7 shows slip distributions, shear stress and normal stress changes at various levels of loading T up to (solid) and beyond (dashed) the point of nucleation.

In Figure 2.8 we plot the average crack lengths $a(t_c)$, asymmetry length $b(t_c)$, peak slip $\delta_{max}(t_c)$, and pore pressure increase T_c at the point of nucleation of dynamic rupture as they depend on the depth H , considering the particular case $K_{hl} = 0.01$. Plotting nucleating crack lengths (Figure 2.8a), there is a clear transition from an effectively deep regime where $a(t_c) \sim \ell$ to a shallow regime in the limit $H \rightarrow 0$ where $a(t_c) \sim \sqrt{h\ell}$. Similarly to the deep limit for such broad increases, the nucleating pore pressure increases (beyond that required to start sliding) and peak slip are also small

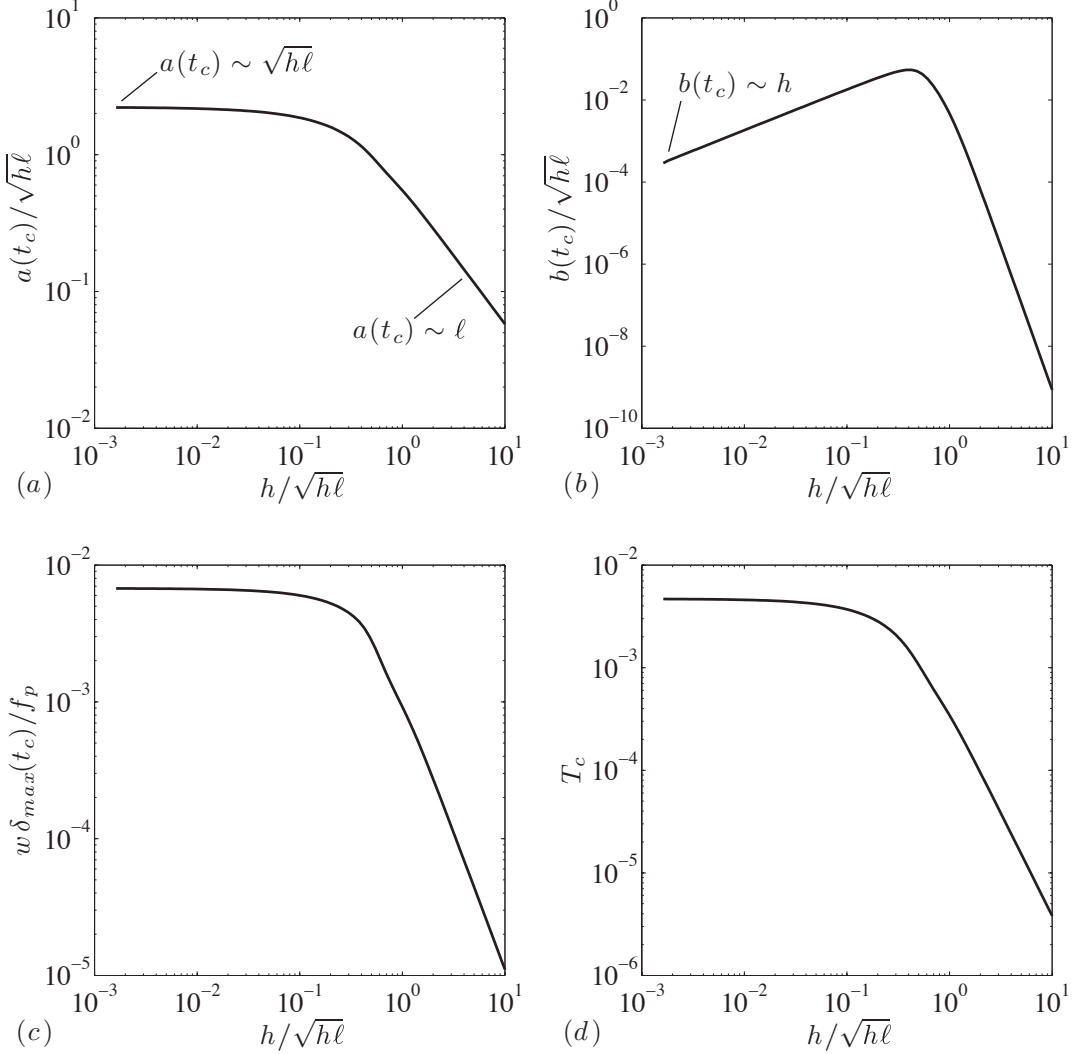


Figure 2.8: (a) Crack half-length, (b) crack asymmetry, (c) peak slip, and (d) pore pressure increase all at the nucleation condition for $f_p = 0.5$, fixed non-dimensional pore pressure curvature ($K_{hl} \equiv f_p \kappa h\ell / \tau_o = 0.01$), and variable effective depth ($H \equiv \sqrt{h/\ell}$). For such broad increases in pore pressure, the plots show a limiting behavior for ruptures much longer than their depth, and particularly a transition in nucleation behavior from an effectively deep scaling at large H , $a(t_c) \approx 0.579\ell$, to a shallow one at low H , $a(t_c) \approx 2.2\sqrt{h\ell}$. The former scaling follows from the eigenvalue problem of Uenishi and Rice [2003], and the latter from a comparable eigenvalue problem in Appendix A.1.2.

and tend towards fixed values in the shallow limit (Figure 2.8c,d). Interestingly, the rupture asymmetry measure at nucleation, $b(t_c)$, increases as rupture lengths become progressively shallower, with a peak when ℓ and h become comparable (Figure 2.8b). At shallower conditions, the asymmetry decreases and scales as $b(t_c) \sim h$ and at all depths the value $b(t_c)$ is much smaller than the length $a(t_c)$. Given that it is the normal stress change, $\Delta\sigma$, that contributes to rupture asymmetry, this implies that its contribution is comparatively small. Consequently, we neglect this term to arrive at the eigenvalue problem of Appendix A.1.2. In solving that eigenvalue problem in the limit $K_{hl} \rightarrow 0$ for a range of $a(t_c)/h$, we closely reproduce the solution of Figure 2.8a. In the shallow limit, the eigenvalue corresponds to the critical crack length $a(t_c) \approx 2.2\sqrt{h\ell}$. As for nucleation far from the free surface, the nucleation lengths in proximity to the surface are also relatively insensitive to the sharpness of the pore pressure profile. Increasing the sharpness by two orders of magnitude to $K_{h\ell} = 1$ leads to a nucleation length in the shallow limit of $a(t_c) \approx 2.5\sqrt{h\ell}$. (While the rupture length varies little, the peak slip and pore pressure increase at nucleation in this sharper case do increase: $\bar{\delta}_{max}(t_c) \approx 0.85$ and $T_c \approx 0.65$.)

As discussed in the introduction, much of the early work applying fracture mechanics to slope stability essentially assumed that conditions were such that the critical length was in this “shallow” regime. According to the results here, this seems to be a reasonable assumption provided the depth measure H is sufficiently low. Since H is the square root of ratio of h/ℓ (or alternatively, h/ℓ^*), it may be difficult to meet a condition that $H < 10^{-2}$, where results generally appear to become depth-independent and critical crack lengths scale as $\sqrt{h\ell}$ (or $\sqrt{h\ell^*}$). For example, to meet the criterion $H = 10^{-2}$ with $h = 20$ m would require $\ell = 200$ km.

2.6 DISCUSSION AND CONCLUSIONS

We modeled the growth of a landslide slip surface as a shear fracture occurring in an elastic medium. The growth is initially driven by a local high in the pore pressure distribution. Because the strength of the slip surface weakens with slip, a point is reached where the slip surface may continue to grow without any further increase in pore pressure. This growth is fast and dynamic and is taken to be the onset of gravitational acceleration of the landslide downslope.

This dynamic growth of the slip surface may arrest, and with it, the downslope acceleration of the landslide mass. Shallow slopes, like those typically found on the seafloor, are particularly susceptible to arrest. Continued acceleration of the slope is dependent either on further increases in pore pressure or dramatic weakening mechanisms during the period of rapid slip.

The relevant lengths are the depth of the slip surface, h , and a lengthscale ℓ that arises from the slip-weakening behavior of the surface. We calculate the length of the slip surface and the slip accrued at the onset of catastrophic failure, as well as the pore pressure required to reach this onset. When pore pressure increases are very broad we find that the total length of the rupture at onset, $2a(t_e)$, depends on a ratio of these two lengths, $H = \sqrt{h/\ell}$.

We plot in Figure 2.9 the expected nucleation lengths as they depend on depth of the slip surface for submarine and subaerial slope conditions. The predicted nucleation lengths for submarine conditions are nearly an order larger than subaerial. Furthermore, the few-hundred-meter lengths are comparable in size to seafloor pockmarks. As pore pressures that generate pockmarks approach lithostatic conditions, there is the potential to nucleate an event with an initial size of Figure 2.9a. In contrast, the nucleation lengths in subaerial events are predicted to be much smaller.

One limitation not considered is the effect of topography, which may limit rupture propagation across- or along-slope. In our analyses we assumed a subsurface rupture running parallel to a uniform slope.

Additionally, we have not investigated the potential continuation of solutions involving other modes of deformation, in addition to the propagation of slip, once pore pressures reach the normal stress. If the least compressive stress is instead inclined towards the slope-parallel direction (e.g., as may occur in normally consolidated slopes), then a hydraulic fracture may be initiated towards the slope surface before pore pressures reach the slope-normal stress. While this fracture would relieve pore pressure on the slip surface, the resulting stress concentrations created by the opening of the fracture may drive slip and propagate the shear rupture. If the least compressive stress is normal to the slope (e.g., in overconsolidated slopes) or if natural layering creates a preferential slope-parallel conduit for fluid flux, then a hydraulic fracture may be initiated. This fracture would be an efficient means of redistributing pore pressures at the level of the normal stress, effectively creating a region with no shear resistance. With continued fluid supply enlarging the weakened zone, the shear rupture may continue towards instability.

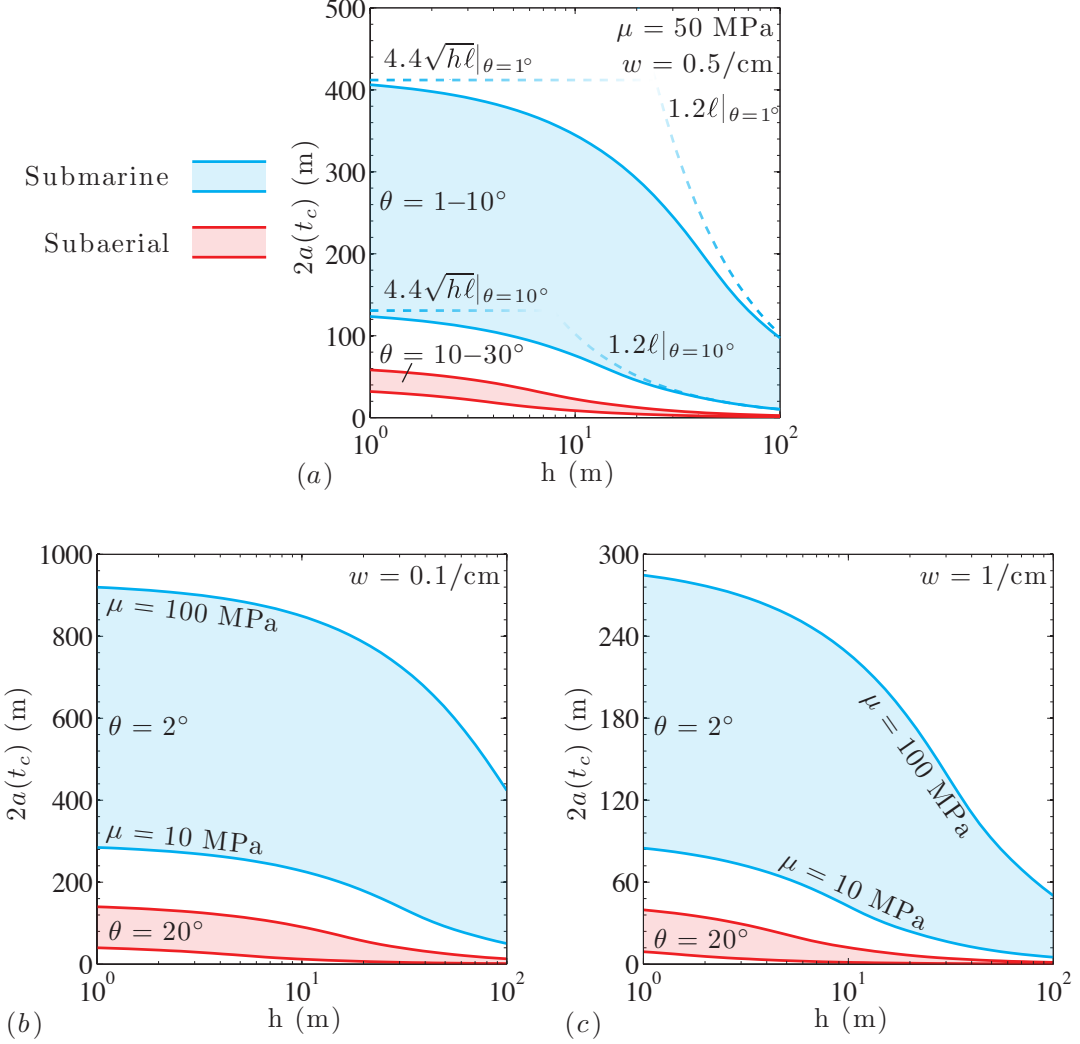


Figure 2.9: Variation of critical slip surface lengths, $2a(t_c)$, with burial depth under submarine and subaerial conditions. These lengths mark the onset of dynamic slip surface growth and downslope acceleration. Solutions presented for case where pore pressures are nearly uniformly elevated over the length $2a(t_c)$ (as in Figure 2.8a). Submarine conditions reflect a sediment bulk weight of $\gamma_b = 1.5\gamma_w$ and shallow slope angles. Subaerial conditions reflect $\gamma_b = 2\gamma_w$ and steeper slopes. In all cases the Poisson ratio is $\nu = 1/3$ and peak friction is $f_p = 0.5$. Results in (a) are for a range of slope angles in both environments; intermediate values of the slip-weakening rate w and shear modulus μ are used. The dashed lines show the scalings of nucleation lengths in the “deep” and “shallow” limits for the bounding submarine cases. Results in (b) and (c) are, respectively, for low and high slip-weakening rates w , each over a range of sediment stiffnesses.

CHAPTER 3

DYNAMIC RUPTURE IN SATURATED INELASTIC MATERIALS

3.1 ABSTRACT

We present an analysis of inelastic off-fault response in fluid-saturated material during earthquake shear rupture. The analysis is conducted for 2D plane strain deformation using an explicit dynamic finite-element formulation. Along the fault, linear slip-weakening behavior is specified, and the off-fault material is described using an elastic-plastic description of the Drucker-Prager form, which characterizes the brittle behavior of rocks under compressive stress when the primary mode of inelastic deformation is frictional sliding of fissure surfaces, microcracking and granular flow. This is a second paper in a two-part sequence, [Viesca et al., 2008; Templeton and Rice, 2008, referred to in what follows as Part 1]. In Part 1, pore pressure changes were neglected in materials bordering the fault. Here, we more fully address the effects of fluid saturation.

This chapter has been published, along with the contents of Appendices D and E, in an edited form as “Viesca, R.C., E. L. Templeton, and J. R. Rice, Off-fault plasticity and earthquake rupture dynamics: 2. Effects of fluid saturation. *J. Geophys. Res.* 113, B09307” and is reproduced here with permission from the publisher.

During the rapid stressing by a propagating rupture, the associated undrained response of the surrounding fluid-saturated material may be either strengthened or weakened against inelastic deformation. We consider poroelastic-plastic materials with and without plastic dilation. During non-dilatant undrained response near a propagating rupture, large increases in pore pressure on the compressional side of the fault decrease the effective normal stress and weaken the material, and decreases in pore pressure on the extensional side strengthen the material. Positive plastic dilatancy reduces pore pressure, universally strengthening the material. Dilatantly strengthened undrained deformation has a diffusive instability on a long enough time scale when the underlying drained deformation is unstable. Neglecting this instability on the short time scale of plastic straining, we show that undrained deformation is notably more resistant to shear localization than predicted by neglect of pore pressure changes.

3.2 INTRODUCTION

3.2.1 PREVIOUS MODELING

Rice et al. [2005] modeled a finite slipping region propagating at steady rupture velocity in an elastic medium and used the resulting stress field about the rupture tip to predict regions which would undergo Coulomb failure. They extended the work of Poliakov et al. [2002], in which the stress field was studied about a propagating semi-infinite rupture, to include not only the stress field about a slip-pulse, but to also include the effects of undrained pore pressure generation. They found that propagation in undrained conditions, in which the timescale for fluid to leave a particular length scale is longer than the time scale of stressing a similar length scale, led to pore pressure increases in the compressional side and pore pressure decreases on the ex-

tensional side. The coseismic pore pressure rise increased the extent of the predicted regions of failure there, whereas the drop decreased it (Figure 3.1). Recent work by de Borst et al. [2006], Rudnicki and Rice [2006], Réthoré et al. [2007], and Dunham and Rice [2008] on dynamic rupture propagation in a fluid saturated linear poroelastic medium with slip-weakening fault friction shows the evolution of rupture and the pore pressure increase and decrease respectively on the compressive and extensional sides of the rupture tip.

3.2.2 OBJECTIVES OF THE PRESENT WORK

In Part 1 of this study, Templeton and Rice [2008] considered dynamic rupture in an elastic-plastic material, which was considered to be dry, or simply to have negligible changes in pore pressure during rupture. They considered a Mohr-Coulomb type of plasticity in the form of the Drucker-Prager model and presented several key results; specifically, that the extent and distribution of the off-fault inelastic deformation is dependent on the initial loading direction of the fault, and the initial proximities of the fault and off-fault material to failure. They also noted the propensity of elastic-plastic laws in that class to exhibit shear localization, and studied features of such localization in modeling of the present type without an explicit localization-limiting procedure (other than the ad-hoc limitation by finite computational grid spacing).

Noting that the cracked/granulated damage zones bordering major crustal faults are expected to be porous and fluid-saturated, we extend this work to include water saturation of off-fault material. We present a linear poroelastoplastic constitutive relationship for undrained behavior (i.e., stressing on a time scale much shorter than the time scale for fluid to leave the length scale of interest), based upon the constitutive relationship for drained behavior (i.e., no change in pore pressure, readily the

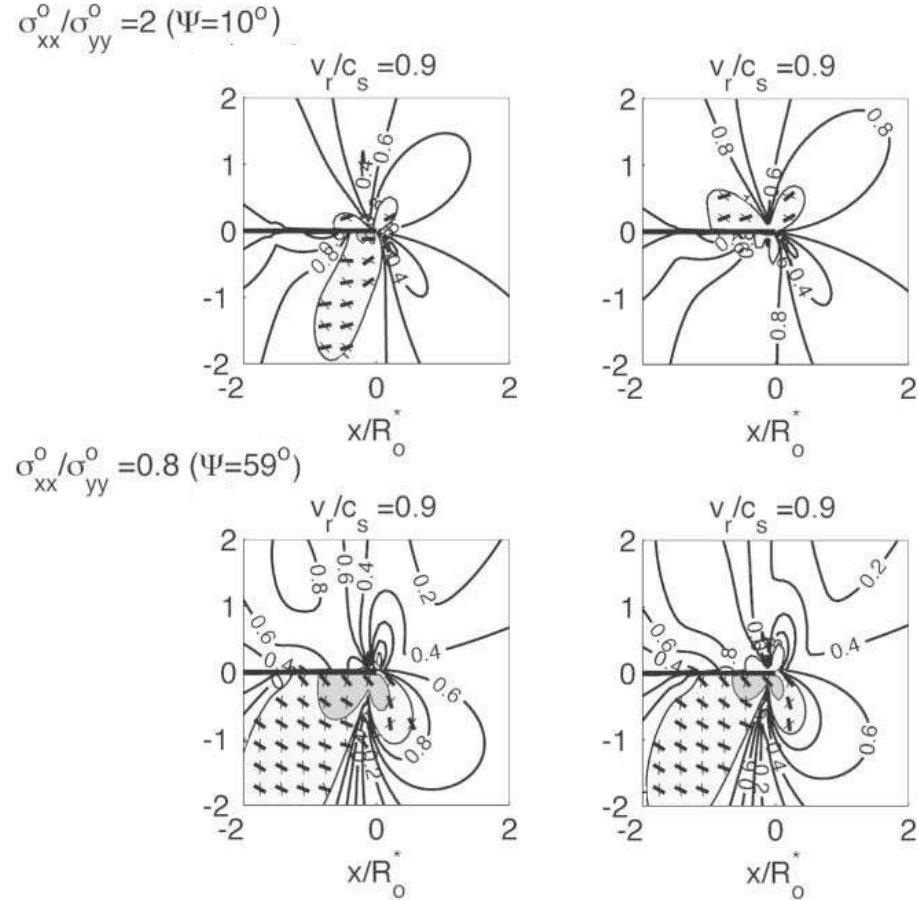


Figure 3.1: Adapted from Rice et al. [2005]. Contour plot of ratio of maximum shear stress to maximum Coulomb strength as a function of position around tip of a propagating right-lateral slip pulse for different inclination angles of the initial most compressive stress, $\Psi = (1/2) \tan^{-1}[2\sigma_{xy}^0 / (\sigma_{xx}^0 - \sigma_{yy}^0)]$, with the fault in a medium without and with undrained poroelastic response (left column, Skempton $B = 0$; right column, $B = 0.6$, respectively). The seismic S ratio is 6.4 and $f_r/f_d = 0.2$. Rupture speeds are scaled with the shear wave speed C_s (so that these cases are very near the Rayleigh wave speed, $0.92C_s$), and distance with the scale length R_o^* (called R_o in the text) that the slip-weakening zone would have at very low propagation speed and under a pre-stress corresponding to a large value of the seismic S ratio.

case for “dry” materials) of Part 1. Subsequently, we study how undrained behavior affects the distribution and magnitude of off-fault plastic deformation, the rupture dynamics, and the localized deformation.

3.3 BACKGROUND AND THEORY

We proceed in two stages in developing our fault model to be representative of saturated porous media. We first consider linear poroelastic behavior. We then go on to consider poroelastoplastic response, including the occurrence of plastic dilatancy, and the consequent feedback on pore pressure.

3.3.1 LINEAR POROELASTICITY

The rate of change in fluid mass, \dot{m} (mass of fluid per unit bulk volume of porous material, with that volume being measured in the reference state from which we take strain as zero) is

$$\frac{\dot{m}}{\rho_f} = \frac{\alpha}{KB} \left(B \frac{\dot{\sigma}_{kk}}{3} + \dot{p} \right) \quad (3.1)$$

where K is the drained bulk modulus of the porous material (i.e., $p = \text{constant}$) and B is Skempton’s coefficient. Under well-known conditions, both B and α may be expressed in terms of the respective bulk moduli of the solid and fluid components, K_s and K_f , and the porosity n (pore space per unit bulk volume in the reference state)

$$B = \frac{1 - K/K_s}{1 - (1+n)K/K_s + nK/K_f} \quad \alpha = 1 - \frac{K}{K_s} \quad (3.2)$$

and α is Biot’s coefficient. The α coefficient appears in the stress measure controlling strain rate in the elastic regime: $\dot{\sigma}_{ij} + \alpha \dot{p} \delta_{ij}$ [Biot, 1941; Nur and Byerlee, 1971; Rice and Cleary, 1976; Wang, 2000].

The interpretation of Skempton's coefficient is that, under undrained conditions ($\dot{m} = 0$), the change in pore pressure is directly proportional to the change in total stress on an element:

$$\dot{p} = -B \frac{\dot{\sigma}_{kk}}{3} \quad (3.3)$$

For elastic-plastic response, the strain rate may be decomposed into elastic and plastic contributions:

$$\mathcal{D}_{ij} = \mathcal{D}_{ij}^e + \mathcal{D}_{ij}^p \quad (3.4)$$

The linear poroelastic constitutive relations give the elastic strain rate of the bulk material, \mathcal{D}_{ij}^e , as a function of the rates of total stress on the bulk material, $\dot{\sigma}_{ij}$, and pore pressure, \dot{p} :

$$\mathcal{D}_{ij}^e = \frac{\dot{s}_{ij}}{2G} + \frac{\delta_{ij}}{3K} \left(\frac{\dot{\sigma}_{kk}}{3} + \alpha \dot{p} \right) \quad (3.5)$$

where G is the shear modulus and $s_{ij} = \sigma_{ij} - \delta_{ij}\sigma_{kk}/3$ is the deviatoric stress tensor.

For drained behavior $\dot{p} = 0$, (3.5) simplifies to

$$\mathcal{D}_{ij}^e = \frac{\dot{s}_{ij}}{2G} + \frac{\delta_{ij}}{3K} \frac{\dot{\sigma}_{kk}}{3} \quad (3.6)$$

For undrained behavior ($\dot{m} = 0$), using (3.3) simplifies (3.5) to

$$\mathcal{D}_{ij}^e = \frac{\dot{s}_{ij}}{2G} + \frac{\delta_{ij}}{3K_u} \frac{\dot{\sigma}_{kk}}{3} \quad (3.7)$$

where K_u is the undrained bulk modulus [Rice and Cleary, 1976]:

$$K_u = \frac{K}{1 - \alpha B} \quad (3.8)$$

Given the short time of stressing associated with rupture propagation, we can

reasonably expect undrained deformation of the off-fault material for large enough lengths. The propagation speed of the rupture is generally of the order of the shear wave speed C_s and the region about which significant deformation occurs is expected [Poliakov et al., 2002; Rice et al., 2005; Templeton and Rice, 2008] to be on the order of the slip-weakening scale length R_o (see captions of Figures 3.1 and 3.3), argued from seismic constraints to be of the order of a few tens of m at mid-seismogenic zone depths Rice et al. [2005]. Rice [2006] has shown based on lab data for intact ultracataclastic gouge that such material is expected to have a hydraulic diffusivity, α_{hy} , of order of 10^{-6} m²/s at mid-seismogenic depths. The hydraulic diffusivity is $\alpha_{hy} = k/(\eta_f \beta_{st})$ where k is the permeability (the component of greatest uncertainty), η_f is the fluid viscosity, and β_{st} is a storage coefficient. Even allowing for up to 10^6 more permeability for other, less finely grained, materials of the damage zone, would allow for diffusivities of order 10^{-6} to 1 m²/s. To consider deformation as effectively undrained, we compare the diffusive length associated with the time R_o/C_s of coseismic stressing to the expected lengthscale of deformation

$$\frac{\sqrt{\alpha_{hy} R_o / C_s}}{R_o} = \sqrt{\frac{\alpha_{hy}}{R_o C_s}} \quad (3.9)$$

which is $\ll 1$ for the estimated values of R_o and α_{hy} and the shear wave speed being of order of km/s. Therefore, we can reasonably expect undrained deformation except down to short diffusive lengthscales of order of a few mm to cm.

3.3.2 POREOELASTOPLASTICITY

Using results from Rice [1977] and Rudnicki [1984a, 2000] (see also Appendices D and E), we extend the equations governing plastic increments in strain introduced in Part 1 of this paper to the fluid-saturated state.

The first result is that plastic dilatational strain appears only as a plastic increment in pore space and consequently, (3.1) may be written as

$$\dot{m} = \rho_f \frac{\alpha}{KB} \left(\dot{p} + B \frac{\dot{\sigma}_{kk}}{3} \right) + \rho_f \mathcal{D}_{kk}^p \quad (3.10)$$

The additional result of Rice [1977] is that the appropriate effective stress measure for evaluating plastic strain increments is the Terzaghi effective stress

$$\sigma'_{ij} = \sigma_{ij} + p\delta_{ij} \quad (3.11)$$

Consequently, using the flow-rule and pressure-dependent yield criterion introduced in Part 1 of this paper, we find that

$$\mathcal{D}_{ij}^p = \frac{1}{h} \left(\frac{s_{ij}}{2\bar{\tau}} + \delta_{ij} \frac{\beta}{3} \right) \left(\frac{s_{kl}}{2\bar{\tau}} + \delta_{kl} \frac{\mu}{3} \right) (\dot{\sigma}_{kl} + \dot{p}\delta_{kl}) \quad (3.12)$$

where $\bar{\tau}$, the scalar measure of shear stress, is the second invariant of s_{ij}

$$\bar{\tau} = \sqrt{\frac{1}{2} s_{ij} s_{ij}} \quad (3.13)$$

and where h is a measure of material hardening, μ is the internal friction parameter in the Drucker-Prager yield criterion (Appendix E, and β is the measure of inelastic dilatancy taken to be the ratio of \mathcal{D}_{kk}^p to the equivalent plastic shear strain, $\dot{\gamma}^{pl}$, defined in Appendix E. For drained behavior (i.e., $\dot{p} = 0$), the plastic strain increments are readily seen to be

$$\mathcal{D}_{ij}^p = \frac{1}{h} \left(\frac{s_{ij}}{2\bar{\tau}} + \delta_{ij} \frac{\beta}{3} \right) \left(\frac{s_{kl}}{2\bar{\tau}} + \delta_{kl} \frac{\mu}{3} \right) \dot{\sigma}_{kl} \quad (3.14)$$

like used in Part 1.

For undrained behavior (i.e., $\dot{m} = 0$), the plastic strain increment expression has been shown to be identical in form to that for drained increments, but with replacement of the drained parameters h , μ , and β with new effective undrained parameters h_u , μ_u , β_u . This undrained inelastic behavior was first noted in the analysis of simple shear deformation to affect the hardening term ($h_u > h$ is characterized as “dilatant hardening”) [Rice, 1975b; Rice and Rudnicki, 1979]. Later work [Rudnicki, 1984b, 2000; Benallal and Comi, 2002, 2003] investigated the general constitutive response of eqs. (3.5), (3.10), and (3.12) with $\dot{m} = 0$ and found that in all such (undrained) deformations with plasticity the total strain rate is

$$\mathcal{D}_{ij} = \mathcal{D}_{ij}^e + \mathcal{D}_{ij}^p = \frac{\dot{s}_{ij}}{2G} + \frac{\delta_{ij}}{3K_u} \frac{\dot{\sigma}_{kk}}{3} + \frac{1}{h_u} \left(\frac{s_{ij}}{2\bar{\tau}} + \delta_{ij} \frac{\beta_u}{3} \right) \left(\frac{s_{kl}}{2\bar{\tau}} + \delta_{kl} \frac{\mu_u}{3} \right) \dot{\sigma}_{kl} \quad (3.15)$$

where h_u , β_u , and μ_u are effective undrained plastic material parameters, defined as

$$h_u = h + \frac{\mu\beta KB}{\alpha} \quad (3.16)$$

$$\beta_u = (1 - B)\beta \quad (3.17)$$

$$\mu_u = (1 - B)\mu \quad (3.18)$$

If we normalize strain by $\tau_p/2G$ and stress by τ_p in eqs. (3.15–3.18), noting that $K/G = 2(1+\nu)/[3(1-2\nu)]$ and similarly for K_u/G replacing ν with ν_u , the undrained Poisson ratio, we find that for a given σ_{ij}^o/τ_p , the relevant parameters describing increments in strain are: ν_u , h_u/G , μ_u , and β_u , or equivalently in terms of more primitive drained and poroelastic properties, ν , h/G , μ , β , α , and B .

As part of deriving eqs. (3.15–3.18) the undrained change in pore pressure in a poroelastic-plastic material with plastic dilatancy can be decomposed into a regular

elastic undrained response and an additional term due to plastic dilatancy,

$$\dot{p} = -B \frac{\dot{\sigma}_{kk}}{3} - \beta \frac{KB \dot{\tau} + \mu(1-B)\dot{\sigma}_{kk}/3}{h + \mu\beta KB/\alpha} \quad (3.19)$$

In addition to these undrained parameters, when considering the yield function in the undrained state [see Part 1, Templeton and Rice, 2008, or Chapter 4, for a more complete introduction]

$$\bar{\tau} + \mu \frac{\sigma_{kk}^o}{3} - b = 0 \quad (3.20)$$

an effective cohesion, b_u , must be included to fully represent undrained behavior

$$b_u = b - B\mu \frac{\sigma_{kk}^o}{3} \quad (3.21)$$

where σ_{kk}^o is the trace of the initial effective stress. That is, the stresses σ_{ij} , defined as the initial effective stress σ_{ij}^o plus the change $\Delta\sigma_{ij}$ in total stress associated with the rapid undrained deformation, $\sigma_{ij} = \sigma_{ij}^o + \Delta\sigma_{ij}$, will, at the onset of plastic response, satisfy

$$\bar{\tau} + \mu_u \frac{\sigma_{kk}^o}{3} - b_u = 0 \quad (3.22)$$

Figure 3.2 shows a drained and the corresponding undrained yield function. Note the material becomes easier to yield during undrained deformation when the mean normal stress is more compressive than the initial value. Similarly, the material becomes stronger when the mean normal stress is more tensile than the initial value.

The derivation of the undrained material parameters is available in Appendix E. Clearly, the transformation of parameters embodied in eqs. (3.8), (3.16–3.18), and (3.22), transforms the undrained elastic-plastic problem into one of precisely the same form as the solutions of Part 1 that neglected changes of pore pressure. Any solution

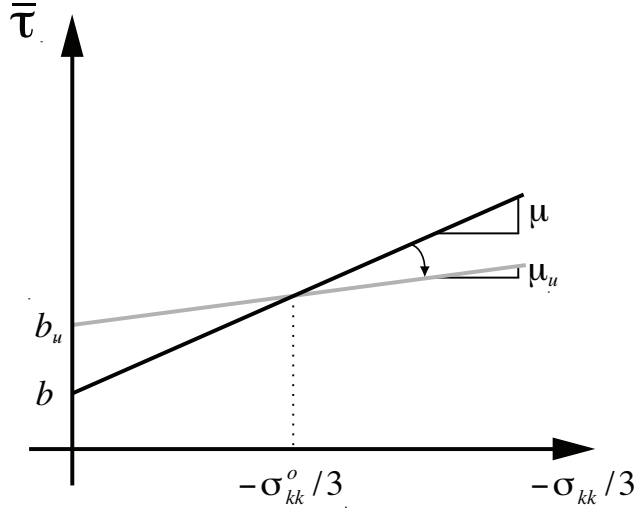


Figure 3.2: Illustration of the effective undrained cohesion, b_u , and internal friction coefficient, μ_u , for a given initial effective stress state, σ_{ij}^o , drained cohesion, b , and drained internal friction, μ . Here $\sigma_{kk} = \sigma_{kk}^o + \Delta\sigma_{kk}$ where $\Delta\sigma_{kk}$ is the total stress change that occurs under undrained conditions; and here $\bar{\tau}$ is based on s_{ij} , where $s_{ij} = s_{ij}^o + \Delta s_{ij}$ where s_{ij}^o is independent of initial pore pressure.

given in that Part 1 may be re-interpreted as an undrained solution for a material of different parameters, and conversely for the solutions given in this Part 2.

3.3.3 SLIP-WEAKENING FRICTION

We approximate the shear strength of the fault during rupture as a normal stress-dependent Coulomb friction law with a peak strength τ_p that degrades with slip Δu to a residual strength, τ_r over a characteristic length scale D_c (Figure 3.3b) [Ida, 1972; Palmer and Rice, 1973]:

$$\tau = \begin{cases} \tau_p - (\tau_p - \tau_r) \frac{\Delta u}{D_c}, & \Delta u \leq D_c \\ \tau_r, & \Delta u > D_c \end{cases} \quad (3.23)$$

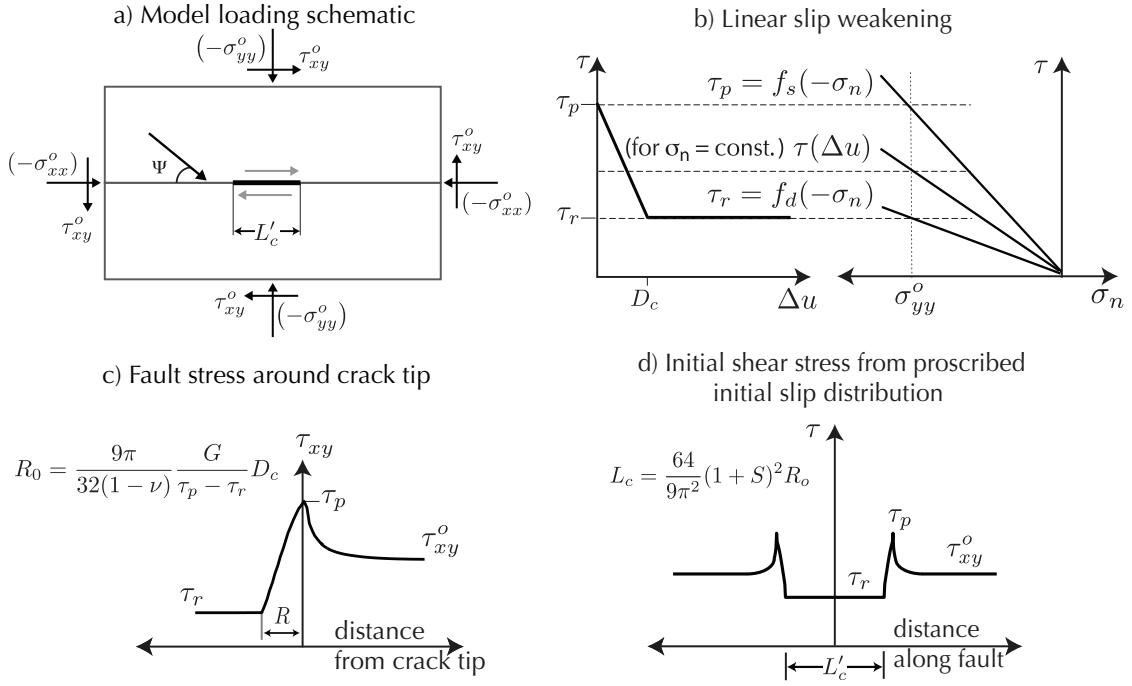


Figure 3.3: a) 2D Model geometry with initial stresses resulting in an angle of most compressive stress to the fault, Ψ . The right-lateral rupture is nucleated in the center of the fault along length L'_c . b) Linear slip-weakening friction model used to describe the degradation of the shear strength of the fault from a peak to a residual strength as a function of slip along the fault. c) Example stress distribution around crack tip during propagation; R_o is the size of R in the limit of low rupture speed and large seismic S ratio, G is shear modulus. d) Fault shear stresses resulting from proscribed initial slip distribution over length L'_c slightly greater than static nucleation length estimate L_c .

where we take the peak and residual strengths to be the product of the fault-normal effective stress, $\sigma'_n = \sigma_n + p_f$, and peak and residual friction coefficients f_p and f_r , respectively, where p_f is the pore fluid pressure on the fault plane. A measure of the initial fault shear stress relative to the fault peak and residual strengths is the seismic S ratio:

$$S = \frac{\tau_p - \sigma_{xy}^o}{\sigma_{xy}^o - \tau_r} = \frac{1}{r} - 1 \quad (3.24)$$

where r is the relative measure of the shear stress used in Chapter 2.

For the elastic case, in which there are no contrasts in hydraulic diffusivities and poroelastic properties across the fault, there is no change in the on-fault pore pressure due to the antisymmetry of the change in mean-normal pressure on each side of the fault. However, for that elastic case, where there is a contrast of properties across the fault, the pore pressure change on the fault itself would depend on the respective permeabilities and storage coefficients on the compressional and extensional side of the fault [Rudnicki and Rice, 2006; Dunham and Rice, 2008]. As an example, a rupture through a fault with more permeable material on the compressional side of the fault than on the extensional side would induce a net pore pressure increase on the fault, favoring further instability and rupture. For a dynamic rupture with crack-like response, this effect can either compete against or enhance the effect of an elastic property contrast.

For our first investigations as reported here, for simplicity we neglect change in pore fluid pressure on the fault. Their full inclusion, left to future study, requires an alteration from standard finite-element analysis for rupture dynamics. As already clear from the elastic analyses cited, whether the fault pore pressure p_f increases or decreases will be sensitive to material properties, especially permeability, on the few mm to cm scale within the damage zones on the two sides of the slip surface. As

shown in Part 1, plastic deformation occurs asymmetrically about and near the fault and consequently introduces a deviation from pure anti-symmetry in the fault-parallel stress changes and in the amount of plastic dilatation. We would therefore expect some change in pore pressure on the fault, even for similar poroelastic properties and permeabilities across the fault; if dilatancy had the dominant effect on pore pressure change, we may expect a stabilization on the fault through an increase in the effective fault-normal stress. While changes to rupture acceleration will change the development over distance of the extent and magnitude of stress around the crack-tip (being functions of rupture velocity), we focus here on the effect of saturated off-fault material on plastic deformation patterns in comparison with those patterns found in the dry counterparts, as in Part 1. Therefore we neglect in this study the effects of pore pressure increases or decreases on the fault itself on the slip-weakening response of the fault. Such slip-weakening, as conventionally assumed, may in fact be a proxy for much more significant but highly localized pore pressure changes along the fault due to thermal pressurization [Sibson, 1973; Lachenbruch, 1980; Mase and Smith, 1987; Andrews, 2002; Noda and Shimamoto, 2005; Rice, 2006; Rempel and Rice, 2006; Suzuki and Yamashita, 2006; Bizzarri and Cocco, 2006].

For a stationary crack, this fault constitutive relation results in a length scale, R_0 , over which the strength drops from peak to residual behind the crack tip (Figure 3.3c), given approximately by [Palmer and Rice, 1973]

$$R_0 = \frac{9\pi}{16(1-\nu)} \frac{G\mathcal{G}}{(\tau_p - \tau_r)^2} \quad (3.25)$$

where \mathcal{G} is the fracture energy ($\mathcal{G} = (\tau_p - \tau_r)D_c/2$ for linear slip-weakening) and ν is the Poisson ratio. R_0 is within a multiplicative factor ($9\pi/32 \approx 0.88$) of the definition of ℓ^* in Chapter 2. Rice et al. [2005] estimated R_0 to range from approximately 1 m

to 40 m at mid-seismogenic crustal depth based on estimates of \mathcal{G} using seismic slip inversion results of Heaton [1990] and an assumed fault strength drop $\tau_p - \tau_d$ based on $f_s = 0.6$ and much smaller f_d .

3.4 NUMERICAL PROCEDURE

3.4.1 IMPLEMENTATION

As outlined in Part 1, we use the finite element method, in the form of ABAQUS/Explicit, [ABAQUS, Inc., 2005] to model dynamic mode-II shear rupture propagation in elastic-plastic material. The rupture direction and slip direction coincide and are in the x direction (Figure 3.3a). The fault plane is parallel to the intermediate principal stress direction of the tectonic pre-stress, σ_{ij}^o . A 2D rectangular mesh composed of linear 4-noded linear reduced integration plane strain elements and containing a horizontal fault is used to model shear rupture propagation along the fault and the resulting off-fault stresses and deformation.

Initial effective stress in the material surrounding the fault is σ_{ij}^o , taken here for the reasons explained to be the effective pre-stress, $\sigma_{ij}^{o,total} + p^o\delta_{ij}$, which is based on the total pre-stress and p^o as an ambient pore pressure prevailing at mid-seismogenic depth. We compare ruptures in “dry” material to those in saturated material at the same initial effective stress. The angle of the most compressive effective stress to the fault is Ψ (Figure 3.3a). The initial effective stress state is uniform and the out of plane principal stress is $\sigma_{zz}^o = (\sigma_{xx}^o + \sigma_{yy}^o)/2$, meaning that $s_{zz}^o = 0$, so the Mohr-Coulomb and Drucker-Prager failure criteria intially coincide (see Part 1). The deformation of the off-fault material in response to stress change $\Delta\sigma_{ij}$ follows the undrained constitutive law outlined in Section 3.3, with σ_{ij} identified as $\sigma_{ij}^o + \Delta\sigma_{ij}$.

All stresses in the analyses are non-dimensionalized by the initial fault-normal

effective stress, σ_{yy}^o , and lengths are non-dimensionalized by R_0 , the length of the static, low stress drop, slip-weakening zone, as given in (3.25). The element spacing Δx is chosen so that the static slip-weakening zone is well resolved, with $\Delta x = R_0/20$.

A mode II shear rupture is nucleated on the fault by altering the initial shear stress distribution along a portion of the fault of length L'_c in Figure 3.3a. The initial shear stress distribution prescribed along the nucleation zone is produced using linear slip-weakening for an initial slip distribution like in Kame [2003]. The length of the nucleation zone, L'_c , is slightly greater than the critical nucleation length,

$$L_c = \frac{16}{3\pi} \frac{G\mathcal{G}}{(\sigma_{xy}^0 - \tau_r)^2} = \frac{64}{9\pi^2} \left(\frac{\tau_p - \tau_r}{\sigma_{xy}^0 - \tau_r} \right)^2 R_0 \quad (3.26)$$

at which a static crack becomes unstable for the large S limit coinciding with singular elastic crack mechanics with small scale yielding. The initial alteration in shear stress along length L'_c results in a stress concentration slightly larger than the peak strength at the tips of the static nucleation zone. This initiates a dynamic rupture at both ends of the nucleation zone at the start of the simulation to produce a bilateral right-lateral shear rupture. Along the predefined fault, a split-node contact procedure is used to prescribe the shear strength, whose evolution follows (3.23). Details of the implementation of the split-node procedure are given in the Appendix B of Part 1.

The entire mesh is surrounded by absorbing elements to minimize reflections from the boundaries. These elements introduce normal and shear tractions on the boundary of the finite element mesh that are proportional to the normal and shear components of velocity at the boundary, with damping constants chosen as the wave impedance factors to minimize reflections of dilational and shear wave energy. These elements perform best when the incident waves arrive perpendicular to the absorbing elements. Forces are applied between the boundary of the plane strain elements and the infinite

elements consistent with the prescribed initial stress state.

3.4.2 PARAMETER SELECTION

Data for intact ultracataclasite fault gouge, summarized by Rice [2006], Table 1, as well as corrections for increased damage by order of magnitude increase in permeability and a doubling of drained compressibility give B values ranging from 0.6–0.9 and α values ranging from 0.65–0.96. Rice and Cleary [1976] provide data in their Table 1 for a variety of sandstones and granites. After correcting the fluid compressibility to a more representative value for mid-seismogenic depth conditions, the B values range from 0.4–0.8 and values of α are between 0.24 and 0.78. In our simulations, we use $\nu = 0.25$, $\alpha = 0.45$ and values of B ranging from 0.5 to 0.9. The undrained Poisson ratios corresponding to values of the Skempton coefficient $B = 0.5, 0.7, 0.9$ are, respectively, $\nu_u = 0.30, 0.32, 0.34$. In results shown here we treat the drained response as ideally plastic, taking $h/G = 0$. Values for the inelastic internal friction and dilatancy coefficients μ and β are given by Rudnicki and Rice [1975] based on rock triaxial experiments conducted by Brace et al. [1966]. The values for μ and β of Westerley granite, over a range of confining pressures, are respectively 0.4–0.9 and 0.2–0.4. Here we use an intermediate value for internal friction ($\mu = 0.6$, consistent with $\tan \phi = 0.75$ in the Mohr-Coulomb criterion, using $\mu = \sin \phi$) and when we consider inelastic dilatancy, we examine the the range of values, $\beta = 0–0.4$. In Section 3.5.1, we compare the effects of varying the Skempton coefficient and plastic dilation.

We define the initial effective stress state using the angle the most compressive initial effective stress makes to the fault, Ψ , the fault frictional parameters, f_s and f_d , and the ratio S relating the initial fault shear stress to the peak and residual fault strength. Additionally, we verify that the initial stress state does not violate

our Drucker-Prager yield criterion. We define a measure of closeness to failure (see Part 1 for additional discussion) as

$$CF = \frac{\bar{\tau}}{-\mu\sigma_{kk}^o/3 + b} \quad (3.27)$$

If $CF > 1$ the initial state of stress violates the yield criterion. Note, the definition of b_u is such that using the undrained material parameters μ_u and b_u in place of the drained parameters would not change CF .

3.5 RESULTS AND DISCUSSION

3.5.1 EFFECT OF UNDRAINED PORE PRESSURE GENERATION ON EXTENT OF INELASTIC DEFORMATION

Initially considering the off-fault material to be poroelastic-plastic with no plastic dilatation, we find that changes in pore pressure significantly increase or decrease the amount of off-fault inelastic deformation. Assuming zero plastic dilatation, the only source of changing pore pressure is from the elastic part of the response. Therefore, the pore pressure response to stressing under undrained conditions is then described by values of the Skempton coefficient, B . Since the changes in pore pressure are proportional to changes in mean normal stress on the bulk material, one may expect during rupture propagation that pore pressure increases on the compressional side of the fault and a pore pressure decreases on the extensional side. These increases and decreases in pressure respectively decrease or increase the effective normal compressive stress, and bring the material closer or further from failure.

In Figure 3.4, we plot the distribution of inelastic deformation (in terms of the equivalent plastic shear strain γ^{pl} defined as the time-integral of $\dot{\gamma}^{pl}$, defined in Ap-

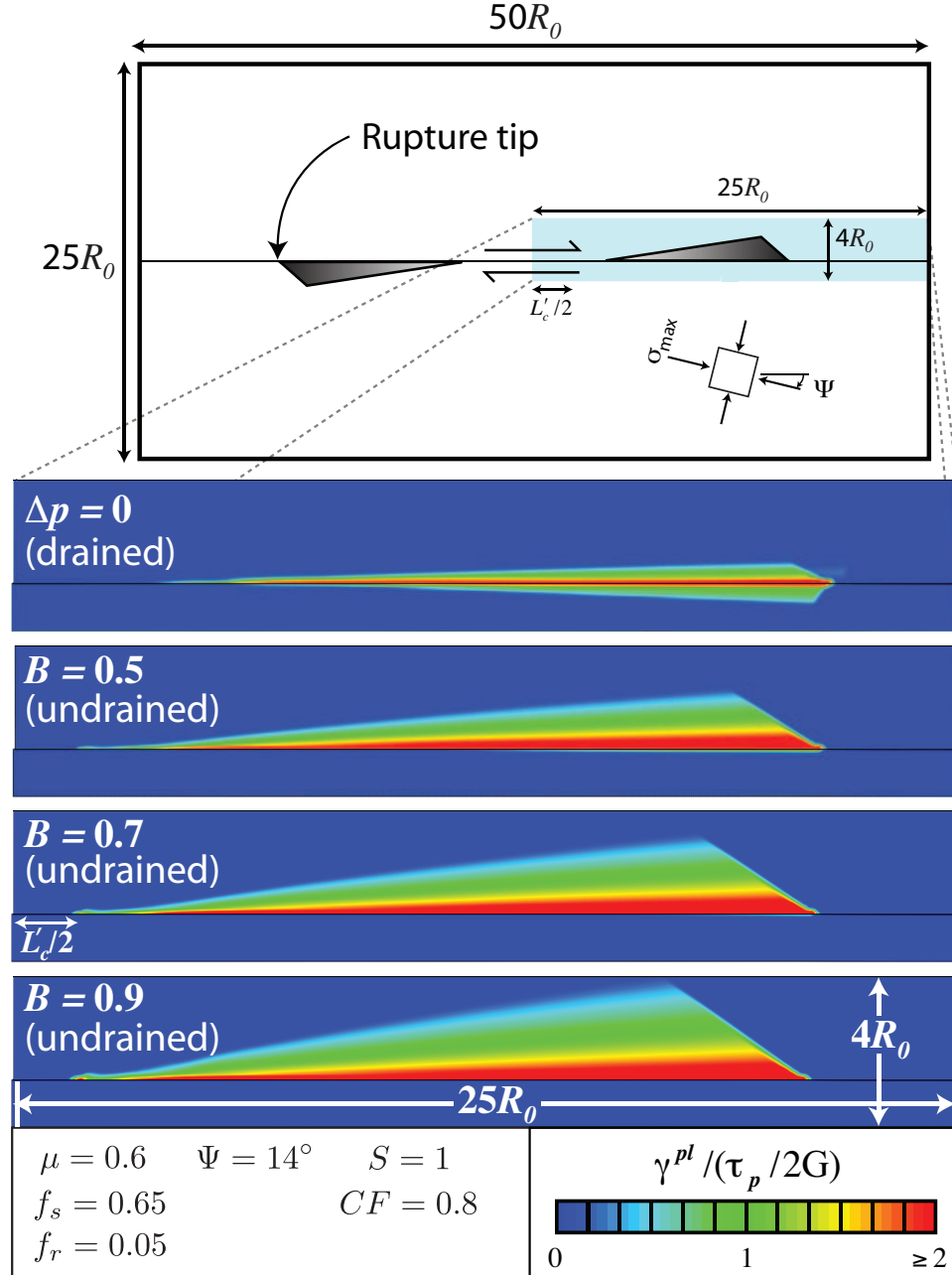


Figure 3.4: Contour plots of $\gamma^{pl}/(\tau_p/2G)$ as a function of distance from the fault for $S = 1$, for $\Psi = 14^\circ$, fixed on- and off-fault strength parameters ($f_s = 0.65$, $f_d = 0.05$; $\mu = 0.6$ ($\tan \phi = 0.75$)), fixed closeness of the initial stress state to off-fault failure ($CF = 0.8$), and no plastic dilation. We consider a case in which pore pressure changes are neglected ($\Delta p = 0$) and undrained cases for which an increase of the Skempton coefficient ($B = 0.5, 0.7, 0.9$) illustrates the role of undrained pore pressure generation in increasing the extent of inelastic deformation.

pendix B) about one side of a bilateral rupture on a right-lateral fault. Here we consider a single, shallow angle (14°) of the initial most compressive stress, and the initial effective stress state is further characterized by a seismic S ratio value of 1.0, with fixed fault frictional parameters $f_s = 0.65$, $f_d = 0.05$, and off-fault material friction parameter $\mu = 0.6$. We consider the drained response (i.e., neglecting changes in p) and undrained response, for three cases in which we vary the value of the Skempton coefficient ($B = 0.5, 0.7, 0.9$). When pore pressure changes are neglected or absent, the inelastic deformation occurs on both the compressional and extensional side of the fault. Considering saturated off-fault material (and momentarily neglecting inelastic dilatation), we find that the extensional side is completely strengthened against inelastic deformation and the compressional side is weakened by respective coseismic pore pressure decreases and increases. The compressional side is further weakened, as expected, with increases of the Skempton coefficient.

In Figure 3.5, we plot the distribution of inelastic deformation for a steeper Ψ (56°), holding the same values of f_s , f_d , μ , and varying over the same values of B as in Figure 3.4. Unlike in the case for a shallower Ψ , here we find that, to the extent the fault has ruptured, for a steeper Ψ and the absence of pore pressure changes, the inelastic deformation occurs on the extensional side of the fault. As expected, increasing values of B leads to an increasing reduction in the extent of the plastically deforming region.

In Figure 3.6, we consider the effect of undrained response with inelastic dilatancy and plot the equivalent plastic shear strain about one side of a bilateral rupture on a right-lateral fault. Here we again consider a single, shallow angle (14°) of the initial most compressive stress, with the same initial stress state and material parameters, except here we allow inelastic dilatancy ($\beta = 0.2\text{--}0.4$) for the case of Figure 3.4

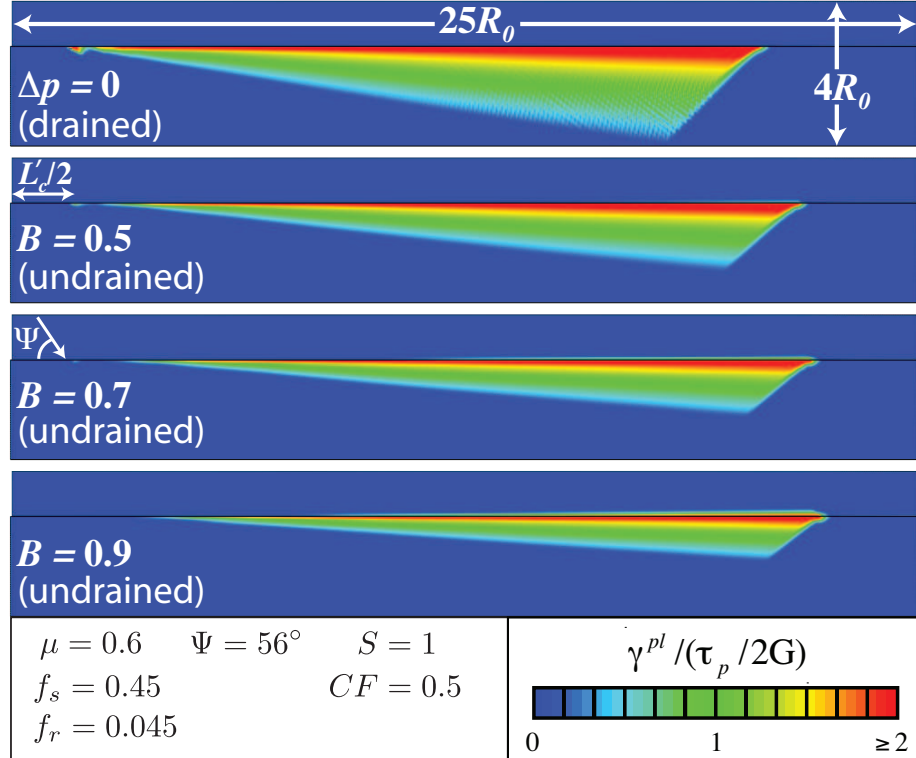


Figure 3.5: Contour plots of $\gamma^{pl} / (\tau_p / 2G)$ as a function of distance from the fault for $S = 1, \Psi = 56^\circ$, fixed on- and off-fault strength parameters ($f_s = 0.45, f_d = 0.045; \mu = 0.6$), fixed closeness of the initial stress state to off-fault failure ($CF = 0.5$), and no plastic dilation. We consider a case in which pore pressure changes are neglected ($\Delta p = 0$) and undrained cases for which an increase of the Skempton coefficient ($B = 0.5, 0.7, 0.9$). As a contrast to a shallower angle ($\Psi = 14^\circ$, Figure 3.4), the drained response exhibits deformation on the extensional side of the fault. Here the undrained cases ($B = 0.5, 0.7, 0.9$) show a decrease in inelastic deformation.

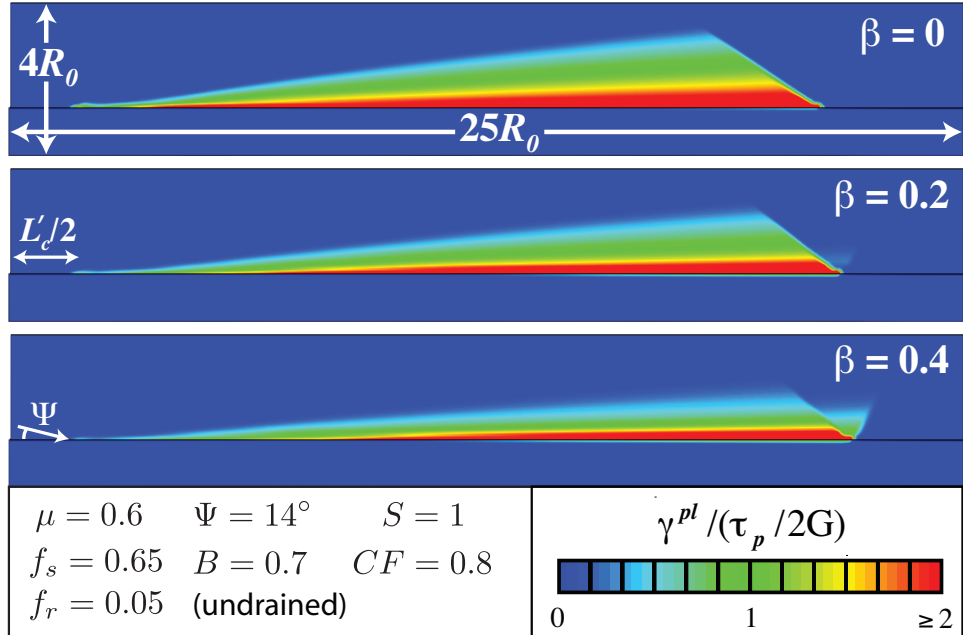


Figure 3.6: Contours of $\gamma^{pl}/(\tau_p/2G)$ as a function of distance from the fault, with all parameters the same as in Figure 3.4, except here we consider the effects of inelastic dilatancy on the undrained response. For the case of Figure 3.4 in which $B = 0.7$ (repeated at top here), increasing plastic dilatancy ($\beta = 0, 0.2, 0.4$) has significant effect on reducing the extent of inelastic deformation.

that formerly had no such dilatancy and $B = 0.7$. Here we might expect that the pore pressure reduction due to plastic dilatancy would work against the pore pressure increase on the compressional side of the fault due to the elastic response. In comparison with the case of no inelastic dilatancy, we find that there is a significant decrease in magnitude and extent of inelastic deformation left behind by the rupture front. Additionally, we see an increase of inelastic deformation occurring at acute angles ahead of the rupture front. For a large value of β , 0.4, we find that the increase in plastic deformation due to pore pressure increases is reduced by plastic dilatancy to the point of reducing the extent of deformation approximately to the original, drained ($\Delta p = 0$) calculation in Figure 3.4.

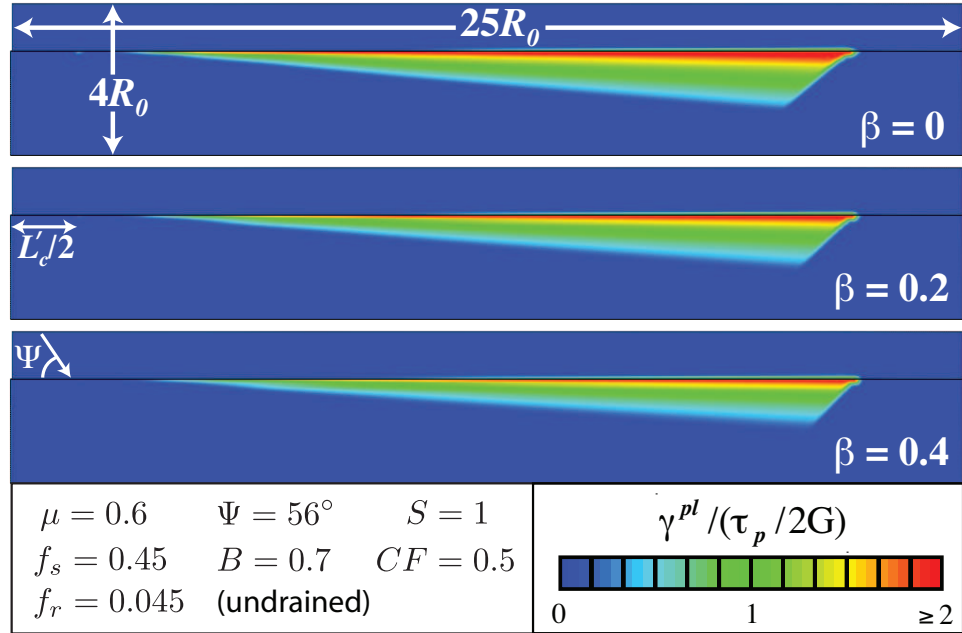


Figure 3.7: Contours of $\gamma^{pl} / (\tau_p / 2G)$ as a function of distance from the fault, with all parameters the same as in Figure 3.5, except here we consider the effects of inelastic dilatancy on the undrained response. For the case of Figure 3.4 in which $B = 0.7$ (repeated at top here), introducing plastic dilatancy serves to reduce the extent plasticity, but does not have as significant effect as in Figure 3.6

In Figure 3.7, for the steep (56°) pre-stress angle, we plot the distribution of inelastic deformation holding the same values of f_s , f_d , μ , and examine the effect of inelastic dilatancy as in Figure 3.6. Here, pore pressure reductions from dilatancy act in conjunction with those reductions due to the poroelastic material response to reduce the extent and magnitude of the inelastic deformation. The further reduction from the introduction of inelastic dilatancy is slight relative to the reductions due to changes of pressure from solely poroelastic behavior.

With the additional allowance for plastic dilatancy (i.e., the creation of pore space through inelastic deformation), we find that the overall effect is to reduce inelastic deformation (note that the equivalent plastic shear strain, to which the dilation is

proportional, is small and of order τ_p/G in the off-fault region). The creation of additional pore space due to plastic dilatation under undrained conditions creates a decrease in pore pressure, irrespective of whether a point is considered on the extensional or compressional side of the fault. Thus, plastic dilatation serves as a mechanism to increase the effective stress and reduce initiated inelastic deformation. Equivalently, we may say that the material is dilatantly hardened.

3.5.2 EFFECT OF PORE PRESSURE-INDUCED CHANGES IN INELASTIC DEFORMATION ON RUPTURE PROPAGATION

The reduction or increase in the amount of off-fault plastic work being done as the rupture passes affects the rupture propagation [Andrews, 2005]. In the cases presented in Figures 3.4 and 3.5, where undrained pore pressure generation controlled by the material Skempton coefficient prohibits or encourages failure, the varying amount of plastic work is readily evident by the changing extent and magnitude of plastic deformation. Figure 3.8 plots the position of the rupture front versus time for the cases presented in Figure 3.4 and for the case of rupture in an elastic material not including changes in pore pressure. Here, the net effect of the undrained response, not considering inelastic dilation, is an increase in the extent and magnitude of inelastic deformation. Consequently, the rupture propagates slightly more slowly with increasing extent. For the cases of Figure 3.6 in which we evaluate inelastic dilatancy during the rupture under undrained conditions, the net effect is a reduction in the extent in deformation. Here in Figure 3.9 the result is a speeding up of rupture propagation that approaches the undrained poroelastic solution as the extent is decreased. Additionally, there is found a suppression (or delay) of the transition to supershear in some cases evaluated where plasticity was incorporated in Part 1 of this paper,

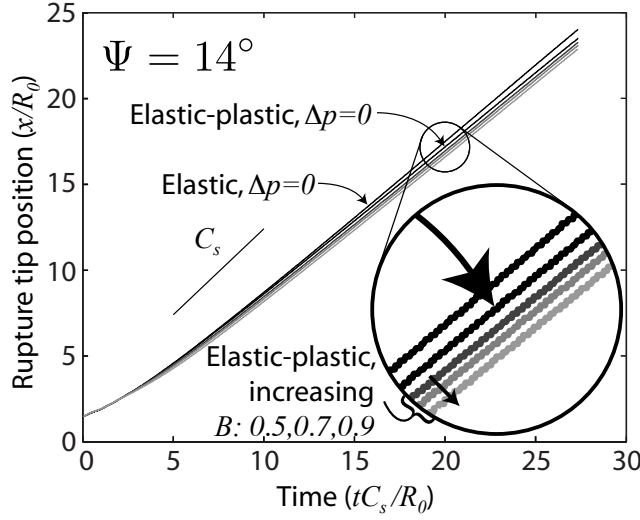


Figure 3.8: Plot of normalized rupture tip position versus normalized time for drained and undrained $\Psi = 14^\circ$ cases of Figure 3.4 (i.e., without inelastic dilatancy). Here C_S is the shear wave speed. The increasing extent of inelastic deformation from drained to undrained responses is reflected in the slight delay for the rupture tip to reach a particular distance of the fault.

[Templeton and Rice, 2008].

3.5.3 ROLE OF UNDRAINED CONDITIONS AND PLASTIC DILATANCY IN THE ELIMINATION OF PLASTIC LOCALIZATION.

Part 1 has shown strain localization to be pervasive in the off-fault inelastic deformation during dynamic rupture when neglecting fluid saturation, at least for zero or even low positive values of hardening h . When fluid saturation is considered and the material is treated as undrained (i.e., no fluid diffusion occurs), these localization features apparently disappear (we have not done the extreme mesh refinements of Part 1). On the basis of the work of Rudnicki and Rice (1975), it was shown in Part 1 that the occurrence of these localization features stemming from the fault is essentially determined by the drained inelastic hardening modulus, h . Localization occurs when

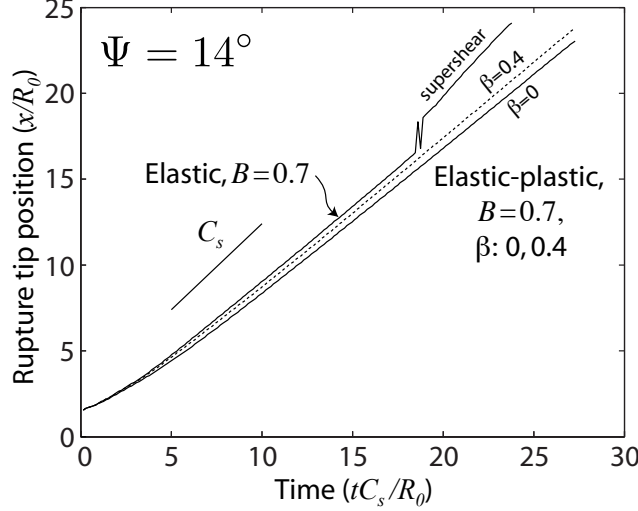


Figure 3.9: Plot of normalized rupture tip position versus normalized time for undrained $\Psi = 14^\circ$ cases of Figure 3.6 with and without dilatancy. Here, the decreasing extent of inelastic deformation with increasing dilatancy is reflected in the slight decrease in time for the rupture tip to reach a particular distance of the fault. In addition to the cases presented in Figure 3.6, we also consider a case of rupture in an undrained elastic medium. In Figure 3.8 we considered a similar elastic case neglecting pore pressure changes. Here we find that under undrained conditions, the rupture transitions to supershear.

h falls below a critical hardening value, h_{cr} , which is determined by μ , β , and the normalized direction of the intermediate principal deviatoric stress, N

$$\frac{h_{cr}}{G} = \frac{1+\nu}{9(1-\nu)}(\beta - \mu)^2 - \frac{1+\nu}{2} \left(N + \frac{\beta + \mu}{3} \right)^2 \quad (3.28)$$

where

$$N = s_2 / \sqrt{\frac{1}{2} s_{ij} s_{ij}} \quad (3.29)$$

This mode of localization (as opposed to compaction banding) is the only mode expected for low-porosity, dilating rocks, such as that considered in Sections 3.5.1 and 3.5.2.

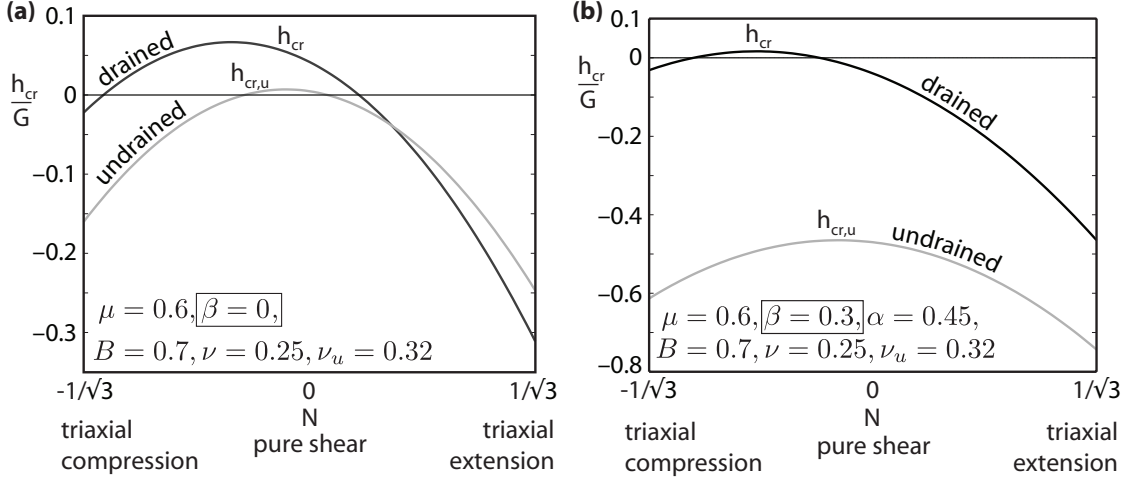


Figure 3.10: Plots of the normalized critical value of hardening h_{cr} , at which localization is expected to occur for static loading, versus the stress state parameter N . No localization of deformation is expected if $h \geq h_{cr}$. (a) Here, we neglect effects of inelastic dilatancy ($\beta = 0$). (b) Here, we consider a dilatancy $\beta = 0.3$ and hold all other parameters fixed. Note the effect of dilatant hardening in the reduction of $h_{cr,u}$.

We have shown that for undrained conditions, effective undrained parameters replace their drained counterparts. The consequence of this is that a critical undrained hardening may naively be calculated based on (3.28). The result is that the critical hardening h_{cr} , now called $h_{cr,u}$, seems to be reduced drastically for most stress states (Figures 3.10a and 3.10b):

$$\frac{h_{cr,u}}{G} = \frac{1 + \nu_u}{9(1 - \nu_u)} (1 - B)^2 (\beta - \mu)^2 - \frac{1 + \nu_u}{2} \left(N + (1 - B) \frac{\beta + \mu}{3} \right)^2 - \frac{K \mu \beta B}{G \alpha} \quad (3.30)$$

(the ratio K/G may be written $2(1 + \nu)/[3(1 - 2\nu)]$ where ν is the Poisson ratio under drained conditions). Here for $\beta = 0$, as $B \rightarrow 1$, $h_{cr,u} \leq 0$, indicating that localization would not be as pervasive (or exist at all) for undrained cases, when the drained $h \geq 0$. Of course, this does not eliminate the possibility that the actual h may be large and negative (e.g., due to a loss of a cohesive strength component

gained through cementation processes on the interseismic time scale), so that even undrained assumptions could make a negative $h_{cr,u}$ larger than h and the localization issue would remain.

However, consideration of $h_{cr,u}$ must additionally be tempered by the fact that the undrained material is diffusively unstable [Rice, 1975a; Rudnicki, 1984b] when $h < h_{cr}$ (the drained value of eq. (3.28)), meaning that since fluid does diffuse over some sufficiently small length scale the material will tend towards drained behavior as time for the diffusion of fluid mass passes. Therefore, there is a competition between the timescale of stressing from the rupture tip and the timescale for fluid diffusion to a potential source of localized failure. For a high hydraulic diffusivity estimate for no longer intact granite of $\alpha_{hy} \approx 10^{-4} \text{ m}^2/\text{s}$ and a low estimation of expected localized failure thickness on the order of $100 \mu\text{m}$, the characteristic timescale for diffusion is of the order of 10^{-4} s . If the region over which significant stressing occurs is on the order of R_o , thought to be a few tens of m, and the rupture propagation is on the order of the shear wave speed, the corresponding timescale for stressing is 10^{-2} s . In such case this would be an issue requiring further examination, which we defer to future work. However, for an immature shear zone with a thickness of order 10 mm, the timescale for diffusion will increase with thickness and rise to the order of the stressing timescale. Therefore, for localized deformation on these larger lengthscales, $h_{cr,u}$ may begin to be the representative hardening value, not considering the effects of significant softening.

3.6 CONCLUSION

Response of fluid-saturated materials is assumed to be effectively undrained on the short time scale of stress concentration near a passing rupture front along a fault.

Poroelastic behavior and inelastic dilation then change the location and spatial extent of inelastic deformation patterns created by dynamic rupture. Undrained pressure changes due to the poroelastic response, which oppose isotropic changes in stress and are proportional to the Skempton coefficient B , strengthen the extensional side of the fault and weaken the compressional side against inelastic yielding. Inelastic dilatation, controlled by β , reduces pore pressure under undrained conditions and strengthens both sides. The undrained response can determine which side of the fault experiences inelastic deformation. For a case examined with a shallow pre-stress angle Ψ , inelastic deformation during rupture occurs on both sides of the fault when drained conditions are assumed. However, the undrained response can have the remarkable effect of completely strengthening the extensional side of the fault, leaving inelastic deformation to occur and increase in extent on the compressional side. For a steep angle Ψ , for which deformation occurs on the extensional side, the effect of undrained pore pressure change only serves to reduce the extent on the extensional side and are not sufficient to weaken the compressional side to the point of yielding. The changed pattern of inelastic deformation between drained and undrained cases only moderately affects the rupture propagation: for significant increases in plastic deformation (e.g., for low Ψ), the rupture in undrained material requires slightly more time to propagate to a comparable distance.

CHAPTER 4

SLIP-SURFACE PORE PRESSURE CHANGES DUE TO INELASTIC DEFORMATION OF ADJACENT MATERIAL

4.1 ABSTRACT

When a region of intense shear in a slope is much thinner than other relevant geometric lengths, this shear failure may be approximated as localized slip, as in faulting, with strength determined by frictional properties of the sediment and effective stress normal to the failure surface. Peak and residual frictional strengths of submarine sediments indicate critical slope angles well above those of most submarine slopes—in contradiction to abundant failures. Because deformation of sediments is governed by effective stress, processes affecting pore pressures are a means of strength reduction. However, common methods of examining slope stability neglect dynamically variable pore pressure during failure. We examine elastic-plastic models of the capped Drucker-Prager type and derive approximate equations governing pore pressure about a slip surface when the adjacent material may deform plastically. In the process we

This chapter has been published in an edited form as “Viesca, R., Rice, J., 2010. Modeling slope instability as shear rupture propagation in a saturated porous medium. In: Mosher, D. C., Shipp, R. C., Moscardelli, L., Chaytor, J. D., Baxter, C. D. P., Lee, H. J., Urgeles, R. (Eds.), Submarine Mass Movements and Their Consequences. Springer-Verlag, New York, pp. 215–225” and is reproduced here with permission from the publisher.

identify an elastic-plastic hydraulic diffusivity with an evolving permeability and plastic storage term analogous to the elastic term of traditional poroelasticity. We also examine their application to a dynamically propagating subsurface rupture and find indications of downslope directivity.

4.2 INTRODUCTION

How sediments deform and pore fluid flows during the shearing process has not been precisely determined for the variety of styles of landslides. While some failures may occur at a stratigraphic discontinuity, others may occur within the sediment column. When failure is within the sediment, to what extent that failure is localized is uncertain. Not knowing when and where failure may start hampers field observations of failure initiation and progression. However, a failure location and time can be constrained by artificially creating failure conditions. For example, Cooper et al. [1998] induced slump failure in a naturally deposited clay slope by artificially elevating pore pressures. Excavation revealed an O(mm) thick intense shear zone within an O(cm) thick disturbed region.

Observations of local deformation and apparent progressive failure [Bjerrum, 1967; Bishop, 1971] inspired treating the shear zone as a slipping fracture and examining criteria for unstable rupture propagation – i.e., criteria for rupture to continue propagation without further loading, presumably the inception of complete slope failure. Palmer and Rice [1973] examined the propagation of rupture from the base of a cut within an overconsolidated clay slope and estimated the rupture length required to initiate unstable growth by gravitational loading. Puzrin et al. [2004] and Puzrin and Germanovich [2005] similarly examined the case of a rupture paralleling the slope surface with the intention of extending the analysis of Palmer and Rice to the failure of

slopes composed of normally consolidated clay or incohesive soil. With experimental observations of shear bands in such soils in mind, they postulate that slope failure in these soils would ultimately occur in local deformation-weakening shear zones similar to the failure of overconsolidated clays. Such an analysis lends itself towards examining effective stress controls on slope stability. This is an appealing approach for studying failure in the submarine environment, where slopes are often too shallow for failure to be explained by infinite slope or limit equilibrium analyses. In this environment, processes affecting pore pressure such as local fluid flux [Dugan and Flemings, 2000] or methane hydrate dissociation [Xu and Germanovich, 2006] have been proposed as mechanisms for initiating failure. The works of Palmer and Rice, and Puzrin and Germanovich, considered the shear strength on the surface to degrade with the amount of slip, assumed that the length of the rupture was much greater than its depth and that the stress-strain relationship of the overlying sediments was linearly elastic until passive or active failure.

The role of fluid in rupture initiation, propagation, and runout is often central in landslide processes. In the experiment of Cooper et al. [1998], decreases in measured pore pressure during early-stage slope movement indicate a stabilizing dilative suction preceding total slope failure. Subaerial flume studies of densely or loosely packed sandy sediment also show a tendency for dilatant stabilization in the case of dense sediments and transition to debris flow when loosely packed [Iverson et al., 2000]. Monitoring shearing rates and pore pressures in a ring shear apparatus, Moore and Iverson [2002] observe the diffusive nature of such stabilization in relatively coarse- and fine-grained sediments.

The question remains how to appropriately determine the pore pressure within a finite thickness shear zone approximated by a sliding surface. Specifically, contribu-

tions from processes within the shear zone may be lumped into the surface behavior in addition to contributions from material deformation beyond the shear zone. When concerned with slip-surface pore pressures, current modeling of dynamic rupture propagation has included inelastic porosity changes as either a slip-proportional porosity change [Rice, 1980; Suzuki and Yamashita, 2008] or a transition to a rate-dependent steady-state porosity [Segall and Rice, 1995; Bizzarri and Cocco, 2006]. Other work has examined slip propagating quasi-statically or dynamically in a saturated poroelastic or poro-elastic-plastic media, but neglected the effect of pore pressure changes on the fault on shear strength [de Borst et al., 2006; Réthoré et al., 2007; Viesca et al., 2008].

4.3 DETERMINING PORE PRESSURES AT A SLIDING INTERFACE WITH PLASTICALLY DEFORMING SURROUNDINGS

The saturated porous material deforms elastically until a yield condition is met. The condition is given by a function F of the effective stress (positive in tension) $\bar{\sigma} = \sigma + p\mathbf{I}$, where σ is the total stress tensor and p is the pore fluid pressure, and potentially a function of other state variables, such as the void ratio or a magnitude of plastic strain. $F(\bar{\sigma}) = 0$ is the yield condition. Here the yield function is expressed in terms of the stress invariants $\text{tr } \bar{\sigma}/3$ and $\bar{\tau} = \sqrt{\mathbf{s} : \mathbf{s}/2}$; where $\mathbf{s} = \sigma - \text{tr } \sigma \mathbf{I}$ is the deviatoric part of the stress tensor. Figure 1 is an illustration of such a function where $\mu = \partial F/\partial(\text{tr } \bar{\sigma}/3)$ is the local measure of the pressure-dependence of the criterion and b is the cohesive strength. During continued plastic deformation, the stress state must satisfy either $\partial F/\partial \bar{\sigma} : \bar{\sigma} = 0$ to move along the yield surface or $\partial F/\partial \bar{\sigma} : \bar{\sigma} > 0$ to follow the outward evolution of the yield surface. Here, we allow the yield surface to evolve with plastic strain and define the hardening modulus,

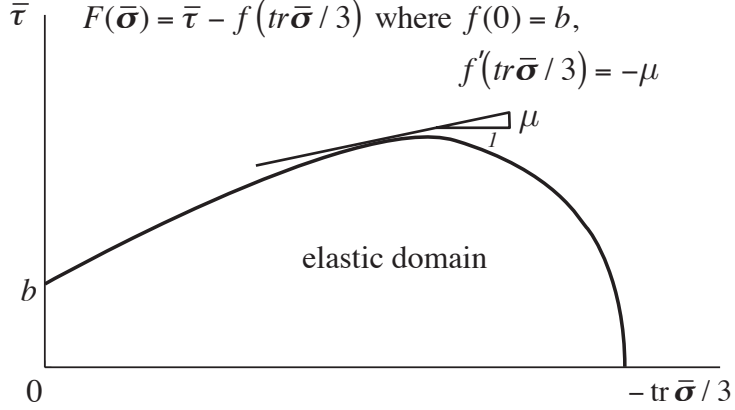


Figure 4.1: Illustration of pressure-dependent yield criterion F .

$\partial F/\partial \bar{\sigma} : \bar{\sigma} = hd\gamma^{pl}$, where $d\gamma^{pl} = \sqrt{2d\epsilon^{pl} : d\epsilon^{pl}}$ and $d\epsilon^{pl} = d\epsilon^{pl} - (\text{tr } d\epsilon^{pl})\mathbf{I}/3$. A second potential $H(\bar{\sigma})$ (here, of similar form to F) indicates the direction of plastic strain increments: $d\epsilon^{pl} = d\gamma^{pl}\partial H/\partial \bar{\sigma}$. From the potentials F and H , we define the second order tensors

$$\mathbf{Q} = \frac{\partial F}{\partial \bar{\sigma}} = \frac{\mathbf{s}}{2\bar{\tau}} + \frac{\mu}{3}\mathbf{I} \quad \mathbf{P} = \frac{\partial H}{\partial \bar{\sigma}} = \frac{\mathbf{s}}{2\bar{\tau}} + \frac{\beta}{3}\mathbf{I} \quad (4.1)$$

where $\beta = \partial H/\partial(\text{tr } \bar{\sigma}/3)$ is the ratio $\text{tr } d\epsilon^{pl}/d\gamma^{pl}$. More explicitly, we decompose the total strain increment into elastic and plastic components $d\epsilon = d\epsilon^{el} + d\epsilon^{pl}$, and the plastic strain increments may be written as $d\epsilon^{pl} = \mathbf{P}(\mathbf{Q} : d\bar{\sigma})/h$. Increments in the Biot effective stress $d\sigma + \alpha dp\mathbf{I}$ are determined by increments in elastic strain, $d(\sigma + \alpha p\mathbf{I}) = \mathbf{L} : (d\epsilon - d\epsilon^{pl})$, were \mathbf{L} is the elastic stiffness tensor described below.

The increments of elastic-plastic total stress and pore fluid mass m (with fluid density ρ) may be written in terms of those of strain and pore pressure [e.g., Rudnicki, 2000]

$$d\sigma = \left(\mathbf{L} - \frac{(\mathbf{L} : \mathbf{P})(\mathbf{Q} : \mathbf{L})}{h + \mathbf{Q} : \mathbf{L} : \mathbf{P}} \right) - \left(\alpha\mathbf{I} + \frac{(1 - \alpha)\text{tr } \mathbf{Q}(\mathbf{Q} : \mathbf{L})}{h + \mathbf{Q} : \mathbf{L} : \mathbf{P}} \right) dp \quad (4.2)$$

$$\frac{dm}{\rho} = \left(\frac{\alpha(1 - \alpha B)}{KB} + \frac{(1 - \alpha)^2 \operatorname{tr} \mathbf{P} \operatorname{tr} \mathbf{Q}}{h + \mathbf{Q} : \mathbf{L} : \mathbf{P}} \right) - \left(\alpha \mathbf{I} + \frac{(1 - \alpha) \operatorname{tr} \mathbf{P} (\mathbf{Q} : \mathbf{L})}{h + \mathbf{Q} : \mathbf{L} : \mathbf{P}} \right) : d\boldsymbol{\epsilon} \quad (4.3)$$

In all bracketed terms preceding dp and $d\boldsymbol{\epsilon}$, the first term corresponds to the elastic response and the second to the contribution of plastic deformation. The elastic coefficients are \mathbf{L} , the fourth-order linear-elastic stiffness tensor (i.e., for isotropic elasticity and a second-order symmetric tensor \mathbf{A} , $\mathbf{L} : \mathbf{A} = \mathbf{A} : \mathbf{L} = K\mathbf{I} \operatorname{tr} \mathbf{A} + 2G \operatorname{dev} \mathbf{A}$, where K and G are the bulk and shear moduli), and B , the poroelastic Skempton coefficient.

Taking the boundary-layer approximation and considering gradients parallel to the slip surface to be much smaller than the normal gradients, the conservation of fluid mass near the surface requires $\partial q / \partial y = -\partial m / \partial t$, where q is the pore fluid mass flux given by Darcy's law $q = -(\rho k / \eta) \partial p / \partial y$, k being the permeability and η the permeating fluid viscosity. Combining fluid conservation and Darcy's law

$$\frac{\rho k}{\eta} \frac{\partial^2 p}{\partial y^2} = \frac{\partial m}{\partial t} \quad (4.4)$$

In calculating the rate of the fluid mass, we consider the region around the slip surface as consisting of material that may differ in mechanical behavior (e.g., elastic stiffness, dilation, and internal friction) from the typical response of the sediment further away from the slip surface (i.e., a disturbed region about the slip surface). The adjoining materials are coupled by the continuity of certain components of stress σ_c (σ_{xy} , σ_{yy} , σ_{yz}) and strain ϵ_c (ϵ_{xx} , ϵ_{zz} , ϵ_{xz}), the remaining free components of stress and strain are designated as σ_f (σ_{xx} , σ_{zz} , σ_{xz}) and ϵ_f (ϵ_{xy} , ϵ_{yy} , ϵ_{yz}). With this in mind we rearrange (4.2) and (4.3) into vector and matrix notation where

$$\{d\sigma\} = d \begin{Bmatrix} \{d\sigma_c\} \\ \{d\sigma_f\} \end{Bmatrix} \quad \text{and} \quad \{d\epsilon\} = d \begin{Bmatrix} \{d\epsilon_c\} \\ \{d\epsilon_f\} \end{Bmatrix} \quad (4.5)$$

such that

$$\{d\sigma_c\} = \{U_1\} dp + [N_{11}] \{d\epsilon_c\} + [N_{12}] \{d\epsilon_f\} \quad (4.6)$$

$$\{d\sigma_f\} = \{U_2\} dp + [N_{21}] \{d\epsilon_c\} + [N_{22}] \{d\epsilon_f\} \quad (4.7)$$

$$\frac{dm}{\rho} = C dp + \{M_1\}^T \{d\epsilon_c\} + \{M_2\}^T \{d\epsilon_f\} \quad (4.8)$$

$[N]$, $\{M\}$, $\{U\}$, C are the matrix, vector, and scalar coefficients whose components are determined by the constitutive relationships (4.2) and (4.3). For example, in xy plane strain

$$\{U_1\}^T = \left\{ -\left(\alpha + \frac{(1-\alpha)\mu(Gs_{xy}/\bar{\tau})}{h+G+\mu\beta K} \right) \quad -\frac{(1-\alpha)\mu(\beta K + Gs_{yy}/\bar{\tau})}{h+G+\mu\beta K} \right\} \quad (4.9)$$

Expressing $\{d\epsilon_f\}$ in terms of $\{d\epsilon_c\}$, $\{d\sigma_c\}$, and dp , (4.8) reduces to

$$\frac{dm}{\rho} = \beta_{stor} dp + \{R\}^T \{d\epsilon_c\} + \{S\}^T \{d\sigma_c\} \quad (4.10)$$

where $\beta_{stor} = C - \{M_d\}^T [N_{12}]^{-1} \{U_1\}$, $\{R\}^T = \{M_1\}^T - \{M_2\}^T [N_{12}]^{-1} [N_{11}]$, and $\{S\}^T = \{M_2\}^T [N_{12}]^{-1}$.

During elastic response, β_{stor} is the poroelastic storage coefficient under 1D consolidation ($d\epsilon_{xx} = d\epsilon_{zz} = 0$), $\beta_{stor} = \beta_{stor}^{el} = [(K_u + 4G/3)/(K + 4G/3)] \alpha / BK_u$ where $K_u = K/(1 - \alpha B)$ is the undrained bulk modulus. During plastic deformation, $\beta_{stor} = \beta_{stor}^{pl}$ is a plastic storage coefficient for one-dimensional straining that reflects a compressibility increase with yielding. We see from (4.2) and (4.3) that during plastic loading the components depend not only on the elasticplastic material parameters, but also on the scaled deviatoric stress components. For plane conditions ($s_{xz} = s_{yz} = 0$) and $s_{zz} = 0$ ($s_{xx} = -s_{yy}$), $\bar{\tau} = s_{xx}^2 + s_{xy}^2$. Deviatoric stress states

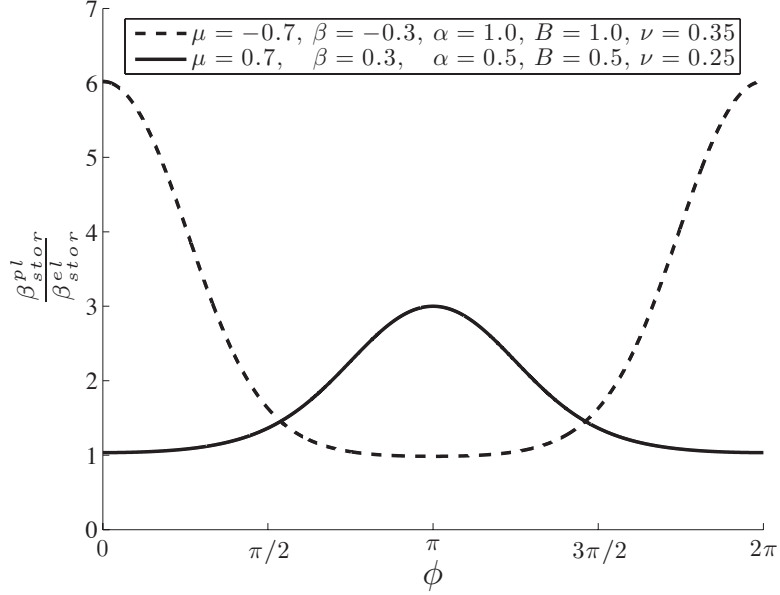


Figure 4.2: Plot of factor of increase in storage coefficients (compressibilities) with onset of ideally plastic ($h = 0$) yielding for compacting sediment (dashed) and dilating rock (solid) over a range of stress states for which $s_{zz} = 0$, $s_{xy}/\bar{\tau} = \sin \theta$, and $s_{xx}/\bar{\tau} = -s_{yy}/\bar{\tau} = \cos \theta$.

can then be characterized by an angle ϕ ($s_{xx} = -s_{yy} = \bar{\tau} \cos \phi$, $s_{xy} = \bar{\tau} \sin \phi$), and then expression for β_{stor}^{pl} is reduced to a dependence on ϕ and material parameters. Considering poro-elasticplastic parameters representative of a low-porosity rock [e.g., Rudnicki and Rice, 1975; Rice and Cleary, 1976], for which yielding will occur on the dilative side of the yield surface ($\mu u > \beta > 0$) for some stress states, the storage may increase threefold (Figure 2). For sediment with pore fluid and component particles much stiffer than the matrix as a whole ($\alpha = B = 1$) yielding on the compacting side of the yield surface (right side of Figure 1), we find the plastic storage may increase sixfold.

Setting $dm = 0$ in (4.10) defines the undrained pore pressure increment dp_u adjacent to the slip surface. (4.10) can be rewritten $dm/\rho = \beta_{stor} d(p - p_u)$ and (4.4)

reduces to

$$\frac{k}{\beta_{stor}\eta} \frac{\partial^2 p}{\partial y^2} = \frac{\partial}{\partial t} (p - p_u) \quad (4.11)$$

In the poroelastic case, $dp_u = -[2G(d\epsilon_{xx} + d\epsilon_{zz}) + d\sigma_{yy}]B(1 + \nu_u)/3(1 - \nu_u)$ where the increments in these stresses and strains can be considered explicitly as functions of time (i.e., within the boundary layer of the disturbed region there is no y -dependence of these increments, which are determined by the coupling to the bulk). Consequently, (4.11) can be rewritten such that the pressure difference from the undrained value satisfies

$$\alpha_{hy} \frac{\partial^2}{\partial y^2} (p - p_u) = \frac{\partial}{\partial t} (p - p_u) \quad (4.12)$$

where $k/\beta_{stor}^{el}\eta$ is the hydraulic diffusivity α_{hy} . Keeping fluid flux and pore pressures continuous across the slip surface, the pore pressure across the surface can be determined. Rudnicki and Rice [2006] found an analytical solution for the surface pressure based on the undrained pressures and hydraulic properties above (+) and below (-) the surface

$$dp_s = \zeta^+ dp_u^+ + \zeta^- dp_u^- \quad \zeta^\pm = \frac{\left(\sqrt{k\beta_{stor}^{el}}\right)^\pm}{\left(\sqrt{k\beta_{stor}^{el}}\right)^- + \left(\sqrt{k\beta_{stor}^{el}}\right)^+} \quad (4.13)$$

In mode-II shear rupture, one side of the ruptured surface undergoes compression (pressurization) and the other extension (suction). The influence of each side on the surface pressure is determined by the hydraulic property contrast in the weighting (4.13). Dunham and Rice [2008] modeled plane-strain bilateral dynamic ruptures with the above solution and found preferences in rupture direction for hydraulic property contrasts thought to be typical of faults.

However, this solution breaks down once the material begins to yield. Most no-

table is the expected change in permeability with plastic deformation. For some fine-grained sediment, moderate changes in void ratio (0.1–0.2) can produce 1–2 order of magnitude changes in permeability Lambe and Whitman [1969]. For low-porosity rock, monitoring of permeability and inelastic deformation during triaxial tests of intact granodiorite and granite shows 1–2 orders of magnitude increases in permeability for axial inelastic strains of the order 0.1% [e.g., Mitchell and Faulkner, 2008]. This effect on its own introduces a time-dependence to the hydraulic diffusivity not accounted for in (4.13). More subtle effects may result when considering changes in pore pressure across the slip surface. One such effect may be that these changes result in some slip surface adjacent material moving away from yield (i.e., some material within each boundary layer deforms plastically, and some elastically). An even more subtle effect with plastic deformation is the effect that the changes in pressure have in determining deviatoric stress components. The poroelastic expression for dp_u could explicitly be written as a function of time (i.e., no y -dependence) and as a result the diffusion equation could be reached. This is generally not the case during plastic deformation. In the expression for dp_u there is a dependence on the components of $\mathbf{s}/\bar{\tau}$, which will vary with the changes in pressure across the slip surface introducing a y -dependence of dp_u .

Solving for the pore pressure at the slip surface requires addressing these deviations from the poroelastic diffusion equation. However, such a solution is nontrivial and we seek to make it more tractable. One such simplification is to assume that permeability changes are uniform within each boundary layer. Consistent with this is to neglect switching between elastic or plastic deformation within each boundary layer (i.e., the boundary layer undergoes either elastic or plastic deformation). Lastly, we neglect surface-normal variations in $\mathbf{s}/\bar{\tau}$ such that dp_u and β_{stor}^{pl} are determined by the coupled

stress components (i.e., depend explicitly on time alone). With these assumptions (4.11) becomes

$$\alpha_{hy}^{pl}(t) \frac{\partial^2}{\partial y^2} (p - p_u) = \frac{\partial}{\partial t} (p - p_u) \quad (4.14)$$

where $\alpha_{hy}^{pl}(t) = k(t)/\beta_{stor}^{pl}(t)\eta$ is an elastic-plastic diffusivity.

4.4 FINITE ELEMENT MODEL OF A DYNAMIC SUBSURFACE RUPTURE

We use the finite element method (with ABAQUS/Explicit) to examine the dynamic propagation of a subsurface shear rupture. Dynamic rupture propagation (i.e., where inertial effects are in the equation of motion and shear rupture speeds are of the order of the shear wave speed c_s), while not typically considered for slope stability, is actively investigated in the earthquake rupture community. We use such an approach here to gain insights into influential processes at the rupture front. The treatment of the model domain is similar to that described in Templeton and Rice [2008] and Viesca et al. [2008], who examined rupture in an unbounded medium. Four-noded plane-strain, reduced-integration elements compose the bulk and a predefined split-node interface represents a likely failure plane. The surface corresponds to the slope surface, and absorbing elements (infinite elements in ABAQUS) are applied downslope and upslope, and at a slope-perpendicular depth to simulate infinite slope conditions and minimize reflections other than from the free surface.

The shear strength τ at the slip surface is effective-stress dependent, $\tau = f\bar{\sigma} = f(\sigma - p_s)$ where the scalar total and effective surface-normal stresses (σ and $\bar{\sigma}$) are positive in compression. The friction at the slip surface follows a slip-weakening description and drops from static f_s to dynamic f_d linearly over a characteristic slip D_c : $f_{sw} = f_s - (f_s - f_d) \min(\delta, D_c)/D_c$. In addition to the depth of the slip surface H , the friction law sets a second model length proportional to $GD_c/\bar{\sigma}_o(f_s - f_d) \equiv \tilde{R}$.

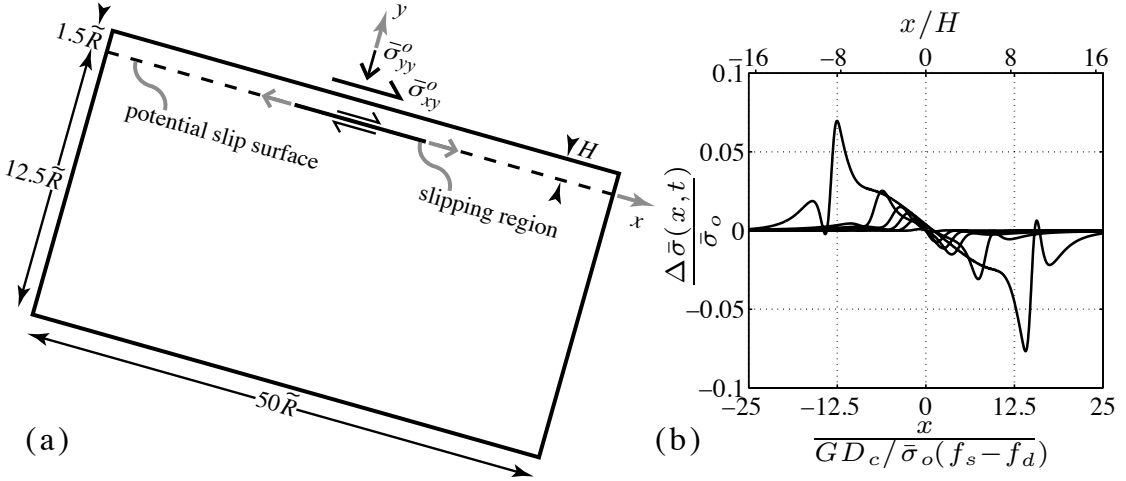


Figure 4.3: (a) Schematic of portion of model domain (actual downdip length \tilde{R}), initial stresses, and subsequent behavior. (b) Snapshots of effective normal stress along the slip surface at intervals of $3.75\tilde{R}/c_s$ for a subsurface rupture at depth $H = 1.5\tilde{R}$ in a saturated poroelastic body. Rupture shows preferred downslope propagation and significant normal stress changes. Model initial stress state is defined as $\bar{\sigma}_{yy}^o = (\gamma_b - \gamma_w)H \cos \theta$, $\bar{\sigma}_{xy}^o = (\gamma_b - \gamma_w)H \sin \theta$, $\bar{\sigma}_{xx}^o = K_o \bar{\sigma}_{yy}^o$, and $\bar{\sigma}_{zz}^o = (\bar{\sigma}_{xx}^o + \bar{\sigma}_{yy}^o)/2$, where $\gamma_b = 1.75\gamma_w$, $\theta = 15.75^\circ$, and $K_o = 1$. Surface frictional parameters are $f_p = 0.45$, $f_r = 0.2$, and $t^* = 0.015\tilde{R}/c_s$. Bulk poroelastic parameters are $G = 600\bar{\sigma}_{yy}^o$, $\nu = 0.35$, and $\nu_u = 0.483$, and $B = 0.4$.

Rupture is nucleated by the Andrews [1985] forced expansion of slip as described by Dunham and Rice [2008], $f_e(x, t) = \max [f_d + A(|x| - v_e t), f_d]$ where $A = (f_s - f_d)/\tilde{R}$ and $v_e = 0.144c_s$. The imposed friction coefficient is $f = \min(f_{sw}, f_e)$ such that the friction coefficient is determined by f_{sw} beyond nucleation. Furthermore, the slip-surface strength is time-regularized to follow $d\tau/dt = -[\tau - f(\sigma - p)]/t^*$ where t^* is the associated timescale, here small in comparison to a physical slip-surface timescale \tilde{R}/c_s .

The initial state of stress is uniform, consistent with the components of stress of a material element in a submerged infinite slope at a depth H (consistent shear and normal tractions are applied at the surface to maintain the initial state). A nonuniform stress state of depth-dependent stresses would not affect slope-parallel rupture

if the surroundings deform elastically. The material away from the slip surface may deform elastically or elastic-plastically. The material yield strength model is based on a heavily overconsolidated clay assuming changes of stress occur in the dilative region of the yield surface where strength is approximated by a linear dependence on effective pressure (i.e., constant μ) and neglecting drained cohesion (i.e., $b = 0$). Under dynamic rupture the rapid deformation leaves little time for fluid flux and undrained conditions are assumed away from the surface. To calculate the pore pressure change on the surface, in the elastic regime we use (4.13), and during elasticplastic deformation (localized at the rupture tip), we approximate the surface pressure with a similar weighting, replacing β_{stor}^{el} with β_{stor}^{pl} given at the onset of yielding and neglect changes in permeability. We calculate the undrained pore pressure increment used in that expression as that resulting from (4.11) with $dm = 0$. Near surface (disturbed region) material parameters are consistent with far-field parameters, except for a twofold reduction of the shear modulus near the slip surface. Model poroelastic parameters and stress state are summarized in the caption of Figure 3.

The effects of the slope surface on the slip surface become significant when the lengths become comparable. For $H/\tilde{R} \rightarrow \infty$ the solution approaches that of a crack in an unbounded medium under uniform initial loading, the case typically considered in earthquake source physics. In that limit, there is no effective normal stress change on the slip surface and no preferred rupture direction for a poroelastic medium when there is no contrast in material properties across the surface. For the poroelastic case when H and \tilde{R} are comparable, total normal stress changes on the fault induce corresponding pore pressure changes and the net effective stress change induces a downslope preference for rupture (Figure 3b). Here, rupture propagation is below the Rayleigh wave speed c_r (for $\nu_u = 0.483$, $c_r \approx 0.95c_s$) until about the last time step

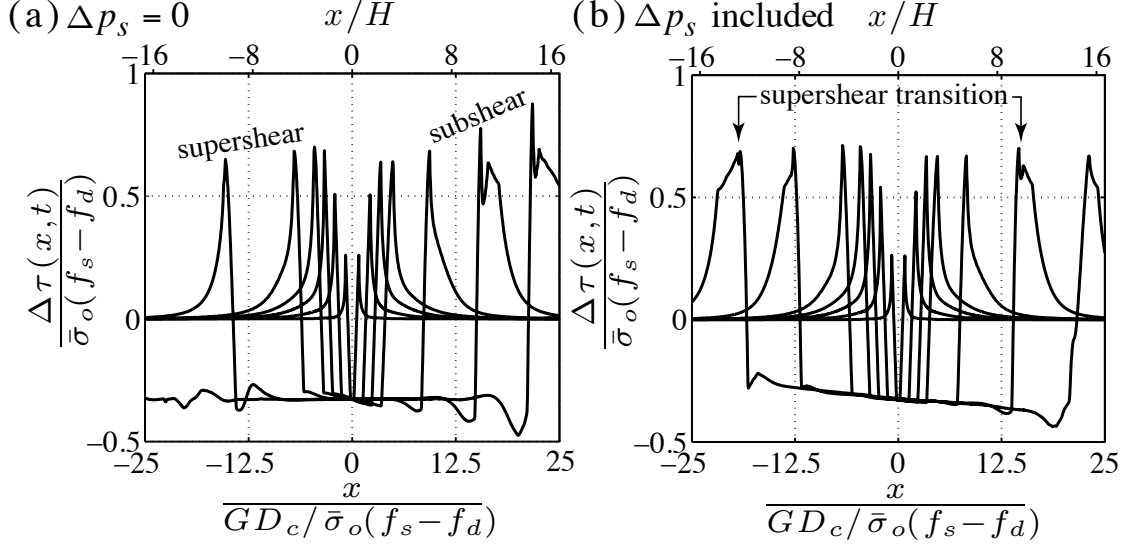


Figure 4.4: Snapshots of slip surface shear stress changes in elasticplastic saturated medium (a) neglecting slip surface pore pressure changes and (b) including elastic-plastic effects on pore pressure changes

plotted in Figure 3b where the rupture begins a transition to rupture propagation beyond the shear wave speed (so-called supershear rupture), first in the downslope direction and shortly followed by a transition in the upslope direction (not shown). These transitions are remarkable since in an unbounded elastic medium this would normally occur for initial slip-surface shear stress states satisfying $r = (\bar{\sigma}_{xy}^o/\bar{\sigma}_{yy}^o - f_r)/(f_p - f_r) \gtrsim 0.36$ Andrews [1976] and here $r = 0.32$ (note $r = 1/(1 + S)$ where S is a similar measure commonly used in earthquake rupture studies).

With the introduction of plasticity, we find the preference for downslope rupture propagation is enhanced when pressure changes at the slip surface are included compared to when they are not. For initial simplicity, we maintain the conditions as in Figure 3 and take $\mu = 0.42$, $\beta = 0.3$, and $b = 0$. Neglecting surface pore pressure changes (Figure 4a) results in a preference to upslope rupture, which reaches supershear propagation speeds first, while the downslope rupture continues at subshear

speeds. In the case considering surface pore pressure change (Figure 4b) there is longer delay to the supershear transition and a slight downslope preference with an initial transition to supershear occurring in the downslope direction, followed shortly by an upslope transition.

4.5 CONCLUSIONS

We considered a slip surface within a saturated, porous elasticplastic medium and derived an approximate equation governing the pore pressure around that surface. That equation takes the form of a diffusion equation with a plastic hydraulic diffusivity, which, in addition to an evolving permeability, also includes a plastic storage coefficient. The storage coefficient may be several times larger than the original elastic storage, which decreases the diffusivity for fixed permeability. We applied this consideration to the dynamic propagation of a slope-parallel subsurface shear rupture. We found that considerable surface effects, most notably normal stress changes, provide a downslope directionality.

CHAPTER 5

CONCLUSIONS

The general aim of this thesis is to understand the role pore fluids play in the deformation of geomaterials. The focal point is the deformation surrounding shear ruptures, as occur in landslides and earthquakes. Below we summarize the questions raised and addressed by each chapter.

Chapter 2

- Can landsliding occur as a thin rupture within the sediment column?
- If the rupture starts locally and spreads, how does it do so?
- Is there a limit to how far a rupture may spread stably?
- What are the lengths at which stability is lost and dynamic rupture initiated?
- If the slope is uniform, will dynamic rupture propagate indefinitely or can it arrest?
- Can the discrepancy of landslide size between submarine and subaerial slopes be accounted for?

Yes, field observations show that landslides can occur as a thin localization of deformation [e.g., Cooper et al., 1998; Pellegrino et al., 2004]. We represent the rupture as a slipping fracture that occurs within an elastic medium, running parallel to an overlying free surface. We impose a slip-weakening friction coefficient on the fracture, consistent with ring shear experiments [e.g., Bishop, 1971; Stark et al., 2005]. Rupture may initiate and spread by local, gradual increases in pore pressure. We find that the rupture may spread quasi-statically and stably as the pore pressure increases. However, we do find a limit at which point rupture growth may continue without any further increase in pore pressure. At this point dynamic rupture is nucleated, marking the onset of acceleration of the overlying slope mass due to the suddenly rapid enlargement of the slip surface. At the time of nucleation, broadly distributed increases in pore pressure result in the shortest lengths, the least amount of accumulated slip, and the lowest peak pore pressure. This dynamic rupture may arrest. Whether arrest occurs is dependent on a measure of shear stress relative to peak and residual strengths. For given peak and residual friction coefficients, arrest is more likely for low-angle slopes (low shear stress). Representing landsliding as a slipping fracture does result in a discrepancy in landslide sizes at the onset of acceleration: for submarine slopes, the nucleation sizes are of the order of several hundred meters along slope, whereas nucleation sizes for subaerial slopes are up to an order of magnitude less.

Chapter 3

- Once dynamic rupture is nucleated, how does material away from the rupture deform in response?
- How do we account for pore fluid effects during undrained, elastic-plastic defor-

mation?

- What effect does this have on the plastic deformation generated away from the slip surface during dynamic rupture?
- What effects do these changes have on rupture propagation?
- Does strictly undrained behavior limit localization of deformation?

As dynamic rupture propagates, stress concentrations near the rupture tip lead to plastic deformation [e.g., Andrews, 2005; Templeton and Rice, 2008]. For an earthquake rupture, the timescale over which this deformation takes place allows for fluid diffusion over lengthscales of a few mm to cm. Because plastic deformation is expected to occur over much larger lengths [e.g., Templeton and Rice, 2008], deformation is under effectively undrained conditions (i.e., no fluid flow). We show that accounting for fluid saturation is simplified under undrained conditions: changes in pore pressure need not be explicitly accounted for. Instead, we may relate increments in stress directly to increments in strain using a set of undrained material parameters based on their counterparts under drained conditions (i.e., no pore pressure change) and poroelastic parameters [as also shown by Rudnicki, 2000; Benallal and Comi, 2002, 2003]. Accounting for fluid saturation, the extent and location of plastic deformation may change. Poroelastic changes in pore pressure reduce plastic deformation on extensional sides of the fault and increase it on compressive sides; and plastic dilatancy reduces plasticity on both sides. These reductions in plasticity cause slight advances in rupture propagation. Furthermore, under drained conditions, Templeton and Rice [2008] found that mesh-dependent localization of the plastic deformation could occur. Benallal and Comi [2002, 2003] proposed that undrained conditions

may suppress such localizations and in the undrained cases studied here, we find an absence of localization.

Chapter 4

- How does dynamic rupture propagation differ when it occurs in a poroelastic medium near a free surface?
- How does plastic deformation affect fluid diffusion on lengthscales close to the slip surface?
- How much does the storage coefficient of a porous material change once plastic yielding occurs?
- How does this affect dynamic rupture propagation near a free surface?

The pore pressure on the slip surface may change due to the deformation of the abutting material. Rudnicki and Rice [2006] and Dunham and Rice [2008] considered changes when the rupture occurred at the interface between two poroelastic medium. They found that a rupture could prefer to propagate in one direction as a result of a combined change in slip surface pore pressure and normal stress. Such a directivity also occurs for rupture propagation parallel to the free surface within a homogeneous poroelastic medium. There, the net effect of pore pressure and slope-normal stress changes is a slight downslope preference for propagation. However, the abutting saturated material is expected to yield, as in Chapter 3 (where slip-surface pore pressure changes are neglected). We extend the poroelastic analysis of near slip-surface fluid movement into the plastic regime. Plasticity may increase or decrease permeability (facilitating or impeding fluid movement). We also highlight the effect that accompanies the increase in material compliance: the fluid storage coefficient may increase,

impeding fluid movement. The coefficient increase is dependent on the stress state, but may be up to a factor of 3-6 for the cases considered. With approximations, we find that the pore pressure in the direction normal to the slip surfaces satisfies a diffusion equation similar to the poroelastic case; however, the hydraulic diffusivity is now dependent on the variable permeability and storage coefficient, and pore pressure changes may include plastic dilatancy. Using approximate solutions for the pore pressure during dynamic rupture propagation, we find similar directivity to the poroelastic case.

APPENDIX A

METHODS FOR DETERMINING PORE-PRESSURE INDUCED NUCLEATION LENGTHS: EIGENVALUE PROBLEMS, NUMERICAL QUADRATURE, AND A VARIATIONAL APPROACH

A.1 NUCLEATION LENGTHS FOR BROAD-CURVATURE PORE PRESSURE PROFILES AND THE CORRESPONDING EIGENVALUE PROBLEMS

A.1.1 NUCLEATION LENGTHS MUCH SMALLER THAN DEPTH

Following a similar procedure outlined in greater detail in Uenishi and Rice [2003], we combine (2.11) with (2.15–2.16), using $q(x) = \kappa x^2/2$,

$$[f_p - w\delta(x, t)] \left[\frac{\tau_o}{f_p} - Rt + \frac{1}{2}\kappa x^2 \right] = \tau_o - \frac{\mu^*}{2\pi} \int_{a_-(t)}^{a_+(t)} \frac{\partial\delta(\xi, t)/\partial\xi}{x - \xi} d\xi \quad (\text{A.1})$$

We take a derivative with respect to time, noting that in the derivative of the integral the terms evaluated at the boundary vanish by the requirement of non-singular

stresses at the crack tip

$$\begin{aligned} -wV(x, t) \left[\frac{\tau_o}{f_p} - Rt + \frac{1}{2}\kappa x^2 \right] - R[f_p - w\delta(x, t)] = \\ -\frac{\mu^*}{2\pi} \int_{a_-(t)}^{a_+(t)} \frac{\partial V(\xi, t)/\partial\xi}{x - \xi} d\xi \end{aligned} \quad (\text{A.2})$$

where $V(x, t)$ is the slip velocity. We use $a(t) = (a_+ - a_-)/2$, $b(t) = (a_+ + a_-)/2$, $X = [x - b(t)]/a(t)$, and scale slip velocity by its rms value, $\mathcal{V} = V(x, t)/[\sqrt{2}V_{rms}(t)]$ to arrive at

$$\begin{aligned} -\frac{w}{\mu^*} a(t) \mathcal{V}(x, t) \left[\frac{\tau_o}{f_p} - Rt + \frac{1}{2}\kappa x^2 \right] - \\ \frac{Ra(t)}{\mu^* \sqrt{2}V_{rms}} [f_p - w\delta(x, t)] = -\frac{1}{2\pi} \int_{-1}^{+1} \frac{\partial \mathcal{V}(s, t)/\partial s}{X - s} ds \end{aligned} \quad (\text{A.3})$$

For the quasi-static problem, $V_{rms}(t)$ diverges at the onset of the nucleation of dynamic rupture. Consequently, we can neglect the second term in the above. After dropping explicit mention of the time-dependence of variables and nondimensionalizing, we find at nucleation that the slip velocity satisfies

$$\left[1 - T + K \frac{(\bar{a}X + \bar{b})^2}{2} \right] \bar{a}v(X) = \frac{1}{2\pi} \int_{-1}^{+1} \frac{v'(s)}{X - s} ds \quad (\text{A.4})$$

The term in brackets is the normalized effective normal stress $\sigma'(x, t)f_p/\tau_o$. In the limit that the normalized curvature is very broad ($K \rightarrow 0$), the problem reduces to the eigenvalue problem of Uenishi and Rice [2003] for which the critical length $\bar{a}(t_c)$ approaches its shortest length at the smallest eigenvalue $\lambda_o \approx 0.579$, when the pore pressure increase is minimally beyond that required to initiate sliding (i.e., $T \rightarrow 0$). Similarly, Garagash and Germanovich [2011] reduce their fault injection problem to

such an eigenvalue problem to conveniently calculate critical conditions for variable pressurization scenarios.

A.1.2 NUCLEATION LENGTHS APPROACHING AND EXCEEDING DEPTH

Following the same steps that lead to (A.4), except here accounting for the free surface (i.e., now using (2.21), but neglecting $\Delta\sigma$ as a negligible contribution) we arrive at a similar eigenvalue problem

$$\begin{aligned} & \left[1 - T + \frac{K_{h\ell}}{2} \left(\frac{aX + b}{hl} \right)^2 \right] \frac{a}{\ell} v(X) \\ &= \frac{1}{2\pi} \int_{-1}^1 v'(s) \left\{ \frac{1}{X-s} + k_1[a(X-s)]a \right\} ds \end{aligned} \quad (\text{A.5})$$

When $K_{h\ell} \rightarrow 0$, the problem reduces to the same eigenvalue problem as would result for the shear-stress loading scenario considered by Uenishi and Rice [2003] had the fault in that scenario lain parallel to the free surface and been driven to slip over a region much longer than its depth. Returning to the pore pressure scenario here and to the limit $K_{h\ell} \rightarrow 0$ of (A.5), the lowest eigenvalue corresponds to the nucleation length $a(t_c)/\ell$ for a given $h/a(t_c)$. In the broad curvature limit, solution of the eigenvalue problem for variable $h/a(t_c)$ reproduces remarkably closely the full numerical solution (Figure A.1), such that the critical length may be expressed as

$$\frac{a(t_c)}{\sqrt{h\ell}} \approx \lambda_{h,o}(H) \quad (\text{A.6})$$

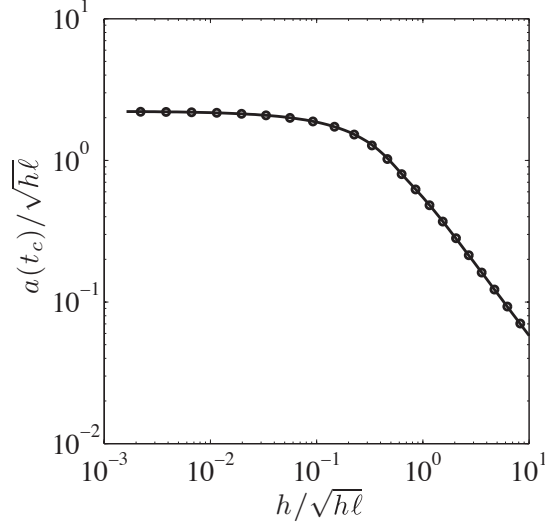


Figure A.1: Comparison of numerical solutions for crack length at nucleation, $a(t_c)/\sqrt{h\ell}$ with dimensionless depth $h/\sqrt{h\ell}$ of Figure 2.8a (solid line) against solutions to the eigenvalue problem of (A.5) in the limit of very broad pore pressure increases, $K_{hl} \rightarrow 0$ (open circles).

where $\lambda_{h,o}$ is the lowest eigenvalue of (A.5) (after dividing by $H \equiv \sqrt{h/\ell}$). To highlight the limit of small $h/a(t_c)$, the smallest eigenvalue in that limit is

$$\frac{a(t_c)}{\sqrt{h\ell}} \approx \lambda_{h,o}(H \rightarrow 0) \approx 2.2 \quad (\text{A.7})$$

In the case of shear-stress loading, this nucleation length is $a(t_c)/\sqrt{\mu^*h/W} \approx \lambda_{h,o}(H)$. The key result of the deep-fault case of Uenishi and Rice [2003] is maintained: namely that this nucleation length is independent of the shape the elevated shear stress profile takes.

A.2 SOLUTION BY COLLOCATION METHOD USING GAUSS-CHEBYSHEV QUADRATURE

Here we outline the numerical method used to solve for crack lengths and slip distributions for given increases in pore fluid pressure. We rely on methods commonly used in fracture problems where the evaluation of the integrals appearing in (2.15), (2.20), and (2.22) is approximated by Gauss-Chebyshev quadrature [e.g., Erdogan and Gupta, 1972; Erdogan et al., 1973]. We find that these direct numerical solutions are favorable to a variational approximation [e.g., Rice and Uenishi, 2010], which, while a fairly accurate approximation for broadly peaked profiles, break down as the curvature increases (see Appendix A.3). Furthermore, this means of numerical solution is preferred other over common methods, such as approximating the slip distribution by piecewise-continuous domains of constant slip [e.g., Rice and Uenishi, 2010] or more involved quadratures such as that of Gerasoulis and Srivastav [1981]. The advantage over the former method is owed to the higher accuracy accompanying a higher order of convergence (second order versus first), and the preference over the latter, in which both accuracy and order are comparable, is owed to the relative ease of implementation.

Gauss-Chebyshev quadrature approximates an integral

$$\int_{-1}^1 \frac{F(\xi)}{\sqrt{1 - \xi^2}} d\xi \approx \frac{\pi}{n} \sum_{j=1}^n F(\xi_j) \quad (\text{A.8})$$

where $\xi_j \equiv \cos[\pi(2j - 1)/(2n)]$. When $F(\xi)$ takes the form of the singular kernel $1/(x - \xi)$, or some bounded kernel $k(x - \xi)$, the quadrature approximation holds at collocation points $x = x_i \equiv \cos(\pi i/n)$ where $i = 1, 2, \dots, n - 1$.

A.2.1 RUPTURES WITH NO RESIDUAL FRICTION

We use the above quadrature rule to simplify the integral in (2.15). With a change of variable $X = (x - b)/a$, where $a = (a_+ - a_-)/2$ and $b = (a_+ - a_-)/2$

$$\int_{a_-}^{a_+} \frac{d\delta(\xi)/d\xi}{x - \xi} d\xi = \frac{1}{a} \int_{-1}^1 \frac{d\delta(s)/ds}{X - s} ds \quad (\text{A.9})$$

We may reduce the latter integral to the form of (A.8) defining a function $\phi(s)$

$$\frac{d\delta(s)}{ds} \equiv \frac{\phi(s)}{\sqrt{(1 - s^2)}} \quad (\text{A.10})$$

such that

$$\int_{-1}^1 \frac{1}{\sqrt{1 - s^2}} \frac{\phi(s)}{X_i - s} ds \approx \frac{\pi}{n} \sum_{j=1}^n \frac{\phi(s_j)}{X_i - s_j} \quad (\text{A.11})$$

where X_i and s_j are defined respectively as x_i and ξ_j are defined above.

Implicit in this quadrature is the approximation

$$\phi(s) \approx \sum_{m=0}^p B_m T_m(s) \quad (\text{A.12})$$

where $p < n$ and $T_j(s)$ is the j -th Chebyshev polynomial of the first kind. With $\phi(s_j)$ abbreviated ϕ_j , this may be rewritten (with summation implied by repeated indices in what follows)

$$\phi_j = C_{jm} B_m \quad (\text{A.13})$$

where $C_{jm} = T_m(s_j)$. Using (A.10) and (A.12), an approximate expression for the

slip at X_i (abbreviated δ_i) is

$$\begin{aligned}\delta_i &\approx \int_{-1}^{X_i} \frac{B_m T_m(s)}{\sqrt{1-s^2}} ds \\ &= \left[\arcsin(X_i) + \frac{\pi}{2} \right] B_o + \frac{\sin [k \arccos(X_i)]}{k} B_k \\ &= D_{im} B_m\end{aligned}\tag{A.14}$$

($k = 1, 2, \dots, p$). Using (A.12) and (A.14),

$$\delta_i = S_{ij} \phi_j \tag{A.15}$$

where $S_{ij} = D_{im} C_{jm}^{-1}$.

(Alternatively, we may have taken the simpler approximation

$$\delta_i = \int_{-1}^1 \frac{\phi(s)}{\sqrt{1-s^2}} H(X_i - s) ds \approx \tilde{S}_{ij} \phi_j \tag{A.16}$$

where $H(x)$ is the Heaviside step function and \tilde{S}_{ij} is a strictly upper triangular matrix of entries π/n . The advantage of S_{ij} over \tilde{S}_{ij} is that, for cases where $\phi(s)$ may be expressed as a finite sum of Chebyshev polynomials and ϕ_j is provided exactly, S_{ij} will provide exact values of slip δ_i . However, in practical application the two yield close results since S_{ij} and \tilde{S}_{ij} differ only slightly.)

As a result of the preceding, we may combine (2.15–2.16) to arrive at the following integral equation (for ruptures *far from the free surface*)

$$[f_p - w\delta(x)] [\sigma'_o - \Delta p(x)] = \tau_o - \frac{\mu^*}{2\pi} \int_{a_-}^{a_+} \frac{d\delta(\xi)/d\xi}{x - \xi} d\xi \tag{A.17}$$

which then may be considered at discrete points $x_i \equiv aX_i + b$ and reduced to the

form

$$[f_p - wS_{ij}\phi_j] [\sigma'_o - \Delta p(aX_i + b)] = \tau_o - K_{ij}\phi_j \quad (\text{A.18})$$

where $K_{ij} = \mu^*/[2\pi a(X_i - s_j)]$. For a given pore pressure increase $\Delta p(x)$, the index i provides a set of $n - 1$ equations for $n + 2$ unknowns ϕ_j , a , and b . One additional condition is that there is no net dislocation beyond the crack:

$$0 = \int_{-1}^1 \frac{\phi(s)}{\sqrt{1-s^2}} ds \approx \frac{\pi}{n} \sum_{j=1}^n \phi_j \quad (\text{A.19})$$

and the remaining two are the conditions that the stress intensity factor at each crack tip is zero. From (A.10) it is evident that the stress intensity factors at the left and right ends are proportional to $\phi(\pm 1)$. As we seek solutions that have nonsingular stresses, we require that $\phi(\pm 1) = 0$. Using interpolation to approximately determine $\phi(\pm 1)$ from ϕ_j [Krenk, 1975], we arrive at the the following constraints on ϕ_j

$$0 = \phi(1) \approx \frac{1}{n} \sum_{j=1}^n \frac{\sin [\pi(2n-1)(2j-1)/(4n)]}{\sin [\pi(2j-1)/(4n)]} \phi_j \quad (\text{A.20})$$

$$0 = \phi(-1) \approx \frac{1}{n} \sum_{j=1}^n \frac{\sin [\pi(2n-1)(2j-1)/(4n)]}{\sin [\pi(2j-1)/(4n)]} \phi_{n-j+1} \quad (\text{A.21})$$

For symmetric $\Delta p(x)$, it can be anticipated that $b = 0$, and only one stress intensity condition need be imposed.

We may define $n + 2$ functions F_r where, from (A.18),

$$F_i \equiv \tau_o - K_{ij}\phi_j - [f_p - wS_{ij}\phi_j] [\sigma'_o - \Delta p(aX_i + b)] \quad (\text{A.22})$$

and F_n , F_{n+1} , and F_{n+2} are simply the right hand sides of (A.19–A.21). The arguments of the functions are taken as Y_r where $Y_j = \phi_j$, $Y_{n+1} = a$ and $Y_{n+2} = b$ and the

Jacobian of F_r may be expressed as

$$J_{rs} = \frac{\partial F_r}{\partial Y_s} \quad (\text{A.23})$$

For example, the entries J_{rs} over $1 \leq r, s \leq n$ are

$$\frac{\partial F_i}{\partial \phi_j} = -K_{ij} + wS_{ij} [\sigma'_o - \Delta p(aX_i + b)] \quad (\text{A.24})$$

We seek solutions to $F_r = 0$ and do so using the Newton-Raphson method. Starting with an initial guess Y_r^0 , we calculate the resulting F_r^0 and J_{rs}^0 and a corresponding correction ΔY_r^0 by solving

$$-F_r^0 = J_{rs}^0 \Delta Y_s^0 \quad (\text{A.25})$$

and updating $Y_r^1 = Y_r^0 + \Delta Y_r^0$. This process is repeated until an N -th increment for which $\max(|\Delta Y_r^N|)$ is below a chosen tolerance.

To account for slip occurring near the free surface the additional changes to shear and normal stress are included. As a result, (A.18) becomes

$$[f_p - wS_{ij}\phi_j] [\sigma'_o - \Delta p(aX_i + b) + M_{ij}\phi_j] = \tau_o - (K_{ij} + L_{ij})\phi_j \quad (\text{A.26})$$

where $L_{ij} = k_1[a(X_i - s_j)]\mu^*/(2\pi)$ and $M_{ij} = k_2[a(X_i - s_j)]\mu^*/(2\pi)$ and in the Newton-Raphson scheme, F_i are changed accordingly. While an increment in pore pressure may be symmetric about the origin, due to the symmetry-breaking effect of the free surface, rupture growth will be asymmetric and b nonzero.

A.2.2 RUPTURES WITH RESIDUAL FRICTION

For accurate results once residual friction is engaged along the crack, the point in space at which friction transitions from a linearly decreasing function to a residual value must occur at a collocation point X_D , providing an additional constraint:

$$S_{Dj}\phi_j = \delta_c \quad (\text{A.27})$$

where $\delta_c \equiv (1 - f_r/f_p)f_p/w$. To add an corresponding unknown variable, we free a parameter of the pore pressure profile to vary. For the example of the load of type (2.11): at fixed load curvature K we seek the magnitude of the increase T that corresponds to the slip weakening distance occupying the position (relative to the crack length) X_D , taking advantage of the monotonic relation apparent from solutions in which the slip weakening position is freely determined. In terms of the Newton-Raphson procedure, we introduce

$$F_{n+3} \equiv S_{Dj}\phi_j - \delta_c \quad (\text{A.28})$$

$$Y_{n+3} \equiv T \quad (\text{A.29})$$

In cases of symmetric rupture growth the position of both slip weakening points will be at the collocation points of $\pm X_D$. However, for asymmetric ruptures, this method suffers from the deficiency that only one slip weakening position will be constrained by (A.27), however the accuracy is still considerably improved.

A.3 APPROXIMATE SOLUTION BY A VARIATIONAL METHOD

Here we follow an energy approach similar to that outlined by Rice and Uenishi [2010] to estimate the crack length at which its growth rate becomes unbounded when far from the surface. In doing so, we define a functional M of slip $\delta(x)$ (at a given instant in time— t -dependence suppressed in below notation) that is $\Delta\tau(x) = -M[\delta(x)]$ where this functional is the integral term in (2.15).

Correspondingly, the functional of change in elastic energy in the body due to slip δ can be written as an integral over the slipped region

$$s[\delta(x)] = \frac{1}{2} \int_{a_-}^{a_+} M[\delta(x)]\delta(x)dx - \int_{a_-}^{a_+} \tau_o(x)\delta(x)dx \quad (\text{A.30})$$

The energy dissipated on the crack surface due to slip-weakening friction is

$$\Phi(\delta) = \int_0^\delta \tau(\zeta)d\zeta \quad (\text{A.31})$$

where the shear strength $\tau(x)$ is given by (2.16).

For a system with initial energy U_o , the total energy after slipping is

$$U = U_o + s[\delta(x)] + \int_{a_-}^{a_+} \Phi[\delta(x)]dx \quad (\text{A.32})$$

and for a given pore pressure loading, the system will reach equilibrium when $\Delta U = 0$ for arbitrary variations in slip ($\Delta\delta$) and crack length (Δa).

To reach an estimate of the crack length and slip at which growth rate becomes unbounded, we will use an assumed slip distribution that satisfies nonsingular crack tip stresses. In nondimensional form (where $\bar{x} = x/\ell$ and $\bar{\delta} = \delta w/f_p$), one such slip distribution is $\bar{\delta}(\bar{x}) = D (A^2 - \bar{x}^2)^{3/2} / A^3$ with length A and slip parameter D , both

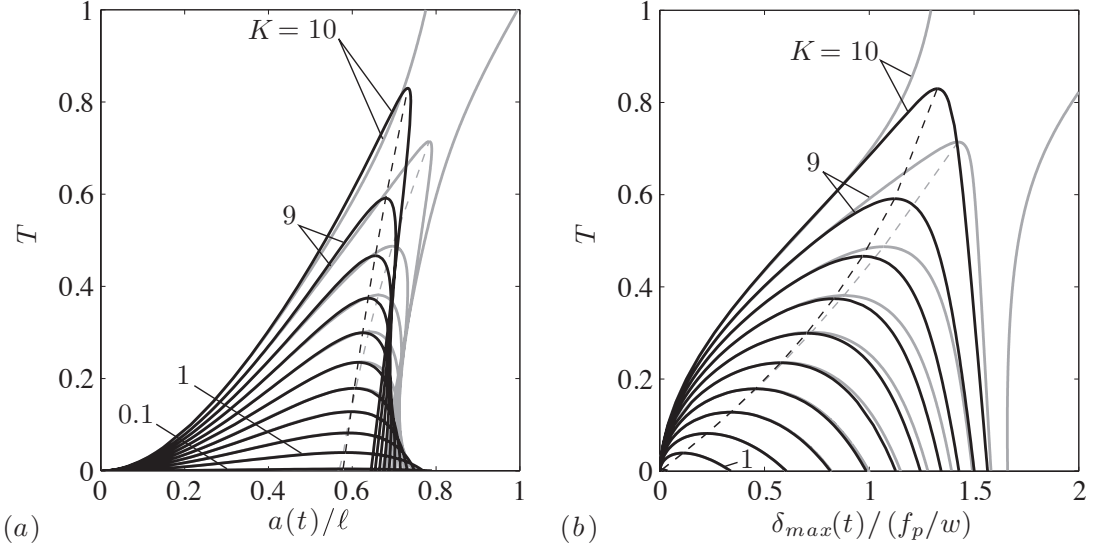


Figure A.2: Comparison of solutions for (a) crack length and (b) peak slip arrived at directly by Chebyshev-Gauss quadrature (black), as in Figure 2.3, and approximately by the simpler variational approach (grey). Dashed lines highlight the divergence, between methods, of the dynamic rupture nucleation point for increasingly peaked pore pressures.

of which will be determined for a given loading profile shape and time.

Evaluating the assumed slip and pore pressure profiles within the energy equation, and defining $\bar{U} = U/(\tau_o \ell f_p / w)$, we find

$$\begin{aligned} \bar{U} = & \frac{U_o}{\tau_o L f_p / w} + \frac{3\pi}{32} D^2 - \frac{3\pi}{8} D A \\ & + (1 - T) \left(\frac{3\pi}{8} D - \frac{16}{35} D^2 \right) A \\ & + \frac{1}{2} K \left(\frac{\pi}{16} D - \frac{16}{315} D^2 \right) A^3 \end{aligned} \quad (\text{A.33})$$

For a given load increase T and curvature K , determining A and D by the simultaneous solution of $\partial U / \partial D = 0$ and $\partial U / \partial A = 0$ provides an approximate solution of the slip profile. Figure A.2 shows the good agreement between the variational approxi-

mation and solutions arrived at using the Gauss-Chebyshev quadrature of Appendix A.2 if pore pressure is only shallowly peaked.

APPENDIX B

ADDITIONAL RESULTS ON DYNAMIC RUPTURE

NUCLEATION:

NUCLEATION UNDER LINEAR SLIP-DEPENDENT STRENGTH, SMALL-SCALE YIELDING, AND POROELASTIC RESPONSE

B.1 ADDITIONAL SLIP-DEPENDENT BEHAVIOR: COHESION LOSS AND UNDRAINED PORE PRESSURE GENERATION

Shear strength may more generally be described as having frictional and cohesive components $\tau(x, t) = f(x, t)\sigma'(x, t) + c(x, t)$. In the above cohesive strength was neglected and slip-weakening presumed solely to come from a reducing friction coefficient. We may also consider a linearly slip-weakening cohesive strength $c(x, t) = c_p - W_c\delta(x, t)$ under constant friction $f(x, t) = f_p$. For a rupture driven by a local increase in pore pressure far from the free surface ($\Delta p(x, t)$) as in (2.11), where the term in brackets replaced with $\bar{\sigma}_o - (\tau_o - c_p)/f_p$, this problem reduces to the form of Uenishi and Rice [2003] (with $R^{UR} \rightarrow f_p R$, $\kappa^{UR} \rightarrow f_p \kappa$, and $W^{UR} \rightarrow W_c$), for which the criti-

cal rupture length a_c is independent of the shape of the pore pressure increase and $a_c \approx 0.579\mu^*/W_c$.

This universal nucleation length is also preserved if, additionally, undrained pore pressure changes are linearly associated with increments of slip, $\Delta p_u(x, t) = W_u\delta(x, t)$. In other words, in addition to the environmentally imposed pore pressure increase $\Delta p(x, t)$, the deformation of shear zone material (approximated as a slipping plane) may cause increases or decreases in pore pressure. These changes may be sustained, if the deformation rate is greater than the rate at which these pore pressure changes can be relieved, with the undrained limit that of no fluid flow. For the simple linear expression for $\Delta p_u(x, t)$, $a_c \approx 0.579\mu^*/(W_c + f_p W_u)$, such that slip-induced reductions (increases) of pore pressure, $W_u < 0$ ($W_u > 0$), result in longer (shorter) critical lengths. However, in the case of undrained pore pressure drops, this seemingly apparent increase in the critical length is inherently unstable, in a manner comparable to dilatant hardening effects in continuous deformation [e.g., Rice, 1975b]: because of an underlying instability when deformation is drained (i.e., when pore pressure changes due to deformation are neglected), accounting for local fluid diffusion allows for the relief of dilatant pore pressure drop and the development of the drained instability.

B.2 ARREST AND RENUCLEATION UNDER SMALL-SCALE YIELDING CONDITIONS

Rupture arrest may not be the final stage if pore pressures continue to increase. Figure B.1a shows instability onset at point (A) followed by two possibilities: indefinite dynamic rupture propagation (i.e., without arrest predicted from quasistatic calculations); or, arrest at point (B) and a second instability developing at point (C) as a result of continued increase in pore pressures. The increase at which an equilibrium rupture is expected to proceed dynamically, without arrest, is denoted by time t_f :

e.g., for the grey curve of Figure B.1a t_f occurs at point (C). For localized increases of pore pressure the instabilities of the type of point (C) occur for low r (eq. 2.19) and are expected to become independent of the profile shape for small r . This is because, for long crack lengths and local increase in pore pressure the stress behind the slip-weakening zone of the crack is, at first approximation, $\tau_r \equiv f_r \sigma'_o$, in which case, when the slip-weakening zone size is negligible compared to the length of the crack, the mode-II stress intensity factor K_{II} is

$$K_{II} = (\tau_o - \tau_r) \sqrt{\pi a} \quad (\text{B.1})$$

(or equivalently in what follows, the factor K_{III} for mode-III loading). In this small scale yielding limit the energy release rate is

$$G = \frac{K_{II}^2}{2\mu^*} \quad (\text{B.2})$$

The criterion for propagation is that [Rice, 1968; Palmer and Rice, 1973]

$$G = \int_0^{\delta_c} [\tau(\delta) - \tau_r] d\delta = (\tau_p - \tau_r) \frac{\delta_c}{2} \quad (\text{B.3})$$

where the latter equality holds for linear slip-weakening friction and a constant effective stress in the weakening zone (here, σ'_o). Combining (B.1–B.3) and arranging we find that the propagation criterion is met for crack lengths satisfying

$$\frac{\tau_p - \tau_r}{\mu^* \delta_c} a \equiv \frac{a}{\ell^*} = \frac{1}{\pi} \frac{1}{r^2} \quad (\text{B.4})$$

that is, the ultimate critical crack length is dependent only on r . In Figure B.1(b–c), we plot the normalized critical crack lengths (beyond which there is no quasistatic

solution) for $0 \leq r \leq 1$. At large r critical crack lengths correspond to values determined by the nucleating pore pressure. For small r we see an abrupt transition to values well approximated by the scaling relationship (B.4) assuming small-scale yielding with the further introduction of a factor of $1/4$ on the right hand side. This factor is a consequence of the variability of the effective stress: the shear stress is τ_r over most of the crack, except for a region around the origin where the reduction in effective stress increases the stress intensity factor nearly twice that of (B.1). While $K = 1$ for the solutions shown, the asymptotic behavior at small r holds for a wide range of K .

B.3 METHOD TO ACCOUNT FOR LARGELY UNDRAINED POREOELASTIC RESPONSE TO SUBSURFACE RUPTURE

Here we outline the integral equation formulation to account for the undrained pore pressure changes on the slip surface induced by slip near a free surface in a poroelastic material. In the limit in which those changes are faster than their dissipation, the pore fluid is effectively under undrained conditions. Due to the discontinuity in deformation across the slip surface, there is a consequent discontinuity in the undrained pore pressure. However, for well-connected systems pore pressure is continuous and the across-surface profile can be found as a solution to the poroelastic equations, as considered by Rudnicki and Rice [2006] and Dunham and Rice [2008] for their respective problems of a steadily propagating slip pulse and an accelerating crack with a bimaterial poro-elastic contrast across the surface. Those authors assumed negligible fluid flow except for surface-normal flow along boundary layers adjacent to the slip surface. Where c_v is the coefficient of consolidation (alternatively, the hydraulic diffusivity), that assumption is reasonable provided the diffusive lengthscale ($\propto \sqrt{c_v t}$),

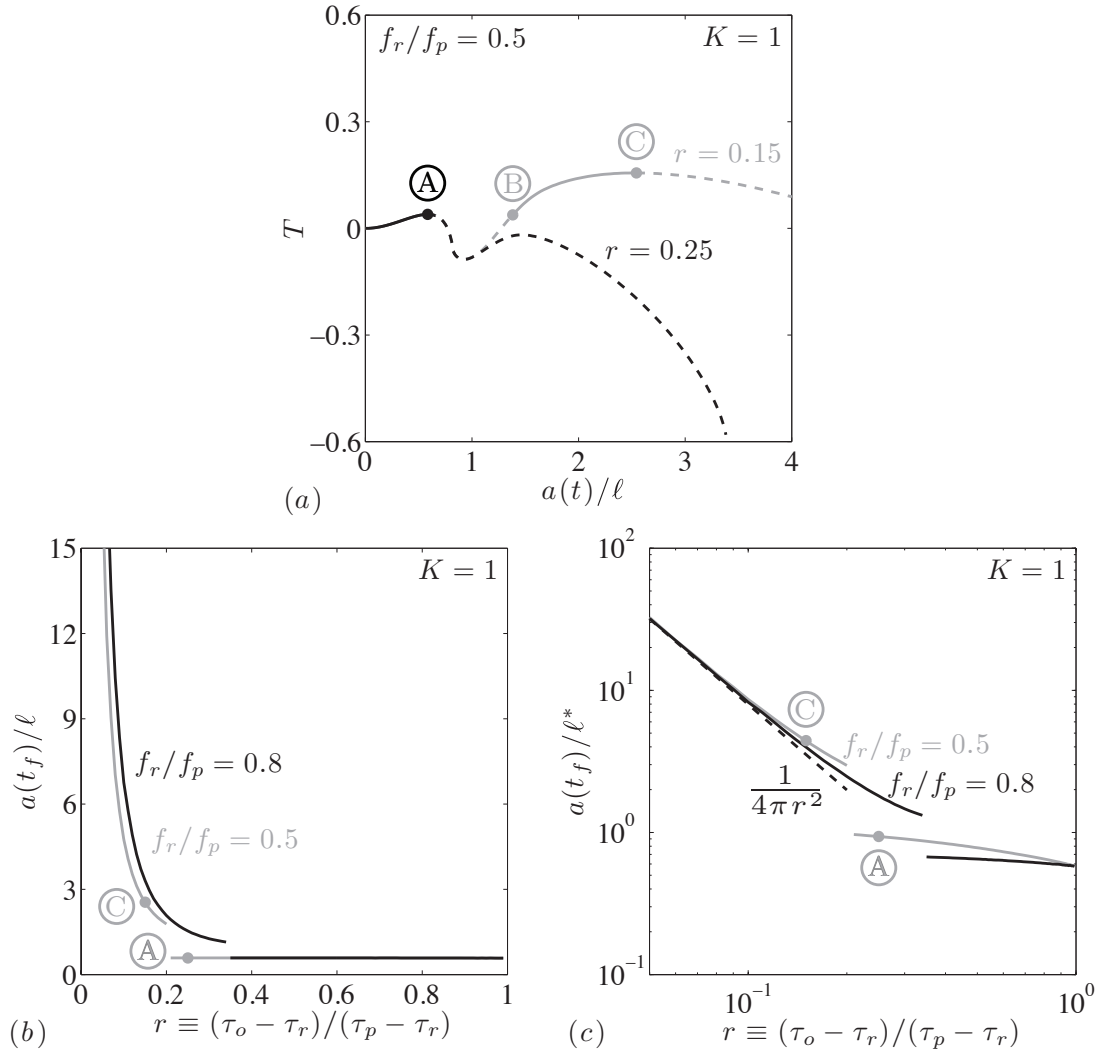


Figure B.1: (a) Two predicted possibilities for crack growth for different prestress measures r : (black) quasistatic growth to point (A) followed by indefinite dynamic rupture, or (grey) quasistatic growth followed by dynamic rupture (A) and arrest at point (B), and continued quasistatic growth to point (C) where dynamic rupture may proceed indefinitely. (b) Crack lengths at time $t = t_f$ beyond which dynamic rupture proceeds dynamically. (c) Small-scale yielding behavior is evident at small r .

is much shorter than other typical problem lengths for stress variation (i.e., h or ℓ). Given the short timescales of stressing in fault rupture propagation, that assumption should hold even for the rather large c_v of 10^{-4} m²/s typical for damaged rock. For landslide rupture propagation in fine silts or clayey material where c_v may be of the order of 10^{-8} m²/s, the assumption of undrained behavior with a small boundary layer may be valid for stress changes occurring over several hours. An extension of these concepts to the case of elastic-plastic off-fault response was developed by Viesca and Rice [2010].

Here, the undrained, poroelastically induced change in pore pressure along the slip surface $\Delta p_u^{el}(x, t)$ may be calculated and superimposed to the background pore pressure increase for use in determining surface frictional strength. For a slope with uniform properties, the change on the slip surface is simply the average of the undrained responses on each side of the surface (denoted by the superscripts \pm): $\Delta p_u^{el}(x, t) \equiv [\Delta p_u^+(x, t) + \Delta p_u^-(x, t)]/2$ and, for plane strain, $\Delta p_u^\pm(x, t) \equiv B(1 + \nu)[\Delta\sigma(x, t) + \Delta\sigma_x^\pm(x, t)]/3$ where B is Skempton's coefficient, $\Delta\sigma(x, t)$ is the normal stress change of (2.22), and $\Delta\sigma_x^\pm(x, t)$ are the different changes in the surface-parallel stress (also taken as positive in compression). When a rupture on a plane is far from the free surface, $\Delta\sigma(x, t) = 0$ and $\Delta\sigma_x^\pm(x, t)$ are antisymmetric and their average amounts to no pore pressure change on the plane. However, for a slip plane near a free surface the response on each side is shifted such that

$$\Delta p_u^{el}(x, t) = \frac{B(1 + \nu)}{3} [\Delta\sigma(x, t) + \Delta\sigma_x^{av}(x, t)] \quad (\text{B.5})$$

where $\Delta\sigma_x^{av}(x, t) = [\Delta\sigma_x^+(x, t) + \Delta\sigma_x^-(x, t)]/2$ contains only the nonsingular contrib-

bution of the free surface

$$\Delta\sigma_x^{av}(x, t) = -\frac{\mu^*}{2\pi} \int_{a_-(t)}^{a_+(t)} \frac{\partial\delta(\xi, t)}{\partial\xi} k_3(x - \xi) d\xi$$

$$k_3(v) \equiv \frac{4hv^4 + 8h^3v^2 + 32h^5}{(4h^2 + v^2)^3} \quad (\text{B.6})$$

Cominbing (2.22), (B.5–B.6), the undrained pore pressure change reduces to a single integral expression

$$\Delta p_u^{el}(x, t) = -\frac{B(1 + \nu)}{3} \frac{\mu^*}{2\pi} \int_{a_-(t)}^{a_+(t)} \frac{\partial\delta(\xi, t)}{\partial\xi} k_4(x - \xi) d\xi$$

$$k_4(v) \equiv k_2(v) + k_3(v) = \frac{4hv^2(v^2 + 8h^2)}{(4h^2 + v^2)^3} \quad (\text{B.7})$$

Free surface effects on the effective normal stress, accounting for both Δp_u^{el} and $\Delta\sigma$, were examined by Viesca and Rice [2010] during dynamic rupture propagation. This was used as a basis for comparison with a model considering plastic deformation within and beyond the boundary layer and its influence, through plastic dilatancy and changes in compressibility and permeability, on the effective coefficient of consolidation blue(hydraulic diffusivity) and slip-surface pore pressure.

APPENDIX C

RESOLVING CONFLICTING SOLUTIONS FOR AN EDGE DISLOCATION NEAR A FREE SURFACE: ELASTIC RECIPROCITY AND SYMMETRY CONSTRAINTS

C.1 BACKGROUND

There is currently a variance in the literature regarding the solution for an edge dislocation near a free surface which has persisted for more than 40 years. With reference to Figure C.1, the point of disagreement is whether, at a point along the x axis, the change of the surface-normal stress σ_{yy} due to the dislocation of Figure 1a is *opposite* or *equal* to the change of shear stress σ_{yx} due to the dislocation of Figure 1b, for the same magnitude of Burgers vector (displacement discontinuity) in both C.1a and C.1b. The original solution of the dislocation problem by Head [1953], consistently with an independent solution by Dundurs and Sendecky [1965], indicated the relation to be *opposite* (as drawn in Figure C.1). However, among his influential body of work on reducing crack and contact problems to singular integral equations and devising

This Appendix has been published in an edited form as “Viesca, R. C., Rice, J. R., 2011. Elastic reciprocity and symmetry constraints on the stress field due to a surface-parallel distribution of dislocations. *J. Mech. Phys. Solids* 59 (4), 753–757” and is reproduced here with permission from the publisher.

effective numerical solution techniques, one special case addressed by Erdogan [1969] required that same dislocation solution. His result, repeated in Erdogan et al. [1973], can be seen to match the original Head solution with the exception of a difference of sign in one term. That difference indicates the relation discussed above to, instead, be *equal*.

This discrepancy became apparent when examining the stress intensity factors for a uniformly pressurized subsurface crack, represented as a continuous distribution of such dislocations. These factors were first numerically calculated in the case of the equal relation by Erdogan [1969] and Erdogan et al. [1973], and in that of the opposite relation by Ashbaugh [1975], who first suggested the solution in Erdogan et al. [1973] required correction. Subsequently, Chen et al. [1980] also suggested the same correction, and, in addition to Higashida and Kamada [1982], also calculated the intensity factors in agreement with those of Ashbaugh [1975]. It is the results of Higashida and Kamada [1982] that feature ambiguously alongside and in contrast with those of Erdogan et al. [1973] in a handbook of stress intensity solutions [Murakami, 1987, p. 167].

However, there are indications that one of the solutions may be correct. Examining the stress intensity factors, K_I and K_{II} , in the limit of a very shallow crack using a beam approximation, Dyskin et al. [2000] note agreement with Higashida and Kamada [1982] over Erdogan et al. [1973]. Additionally, several other authors have presented consistent solutions [Thouless et al., 1987; Yang and Li, 1997; the latter claim a misprint in the solution of Head, 1953, although we find no such misprint when comparing their solutions]. Additionally, work by Erdogan [1971] for a crack parallel to a bimaterial interface between joined half-spaces indicates an opposite relation. Because that configuration reduces, in the limit of zero stiffness for the uncracked

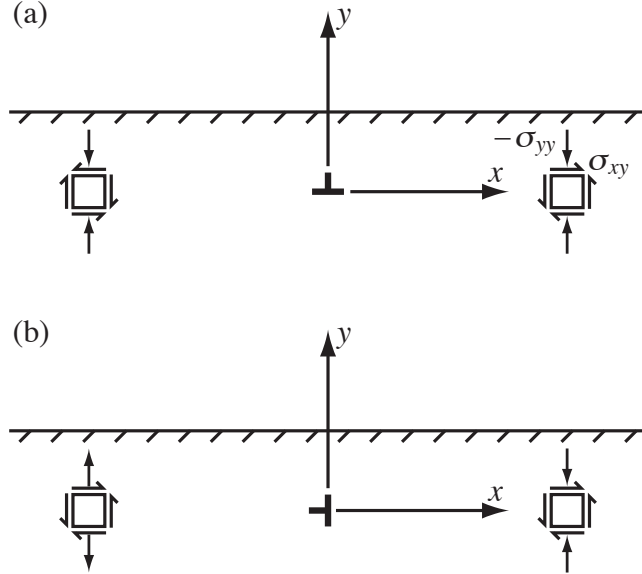


Figure C.1: Elements along the x -axis and at symmetric points about the y -axis indicate stress (σ_{xx} omitted) due to an edge dislocation with Burgers vector (a) parallel and (b) perpendicular to a free surface a distance h away. Standard positive conventions for normal (in tension) and shear stresses are designated in (a).

half-space, to the problem considered in 1969 and 1973, there is an inconsistency among the set of papers. Further, Tada et al. [2000, p. 231] give a beam theory asymptote for the mode I stress intensity factor that is different from Dyskin et al. [2000] and seemingly in agreement with the results of Erdogan et al. [1973]. However, if we assume that beam theory adequately describes energy transfer to the crack tip, hence implies $K_I^2 + K_{II}^2$, that mode-I asymptote requires that $K_{II} = \sqrt{3}K_I$, which deviates strongly from the trend in mode II of Erdogan et al. [1973]. Furthermore, Paynter et al. [2006], aware of the sign mismatch leading to the dissimilar results, maintain that the solution of Erdogan et al. [1973] is correct. The matter appears to some extent unsettled and we aim here to conclusively address the discrepancy based not on re-deriving specific proposed solutions but, rather, appealing to general

considerations of elastic reciprocity and symmetry.

C.2 ELASTIC RECIPROCITY

The Betti reciprocal theorem requires that for two elastic stress-displacement fields $\sigma_{ij}^{(1)}, u_k^{(1)}$ and $\sigma_{ij}^{(2)}, u_k^{(2)}$ in the half space, corresponding to different distributions of displacement discontinuity along a cut (e.g., to represent a crack) coincident with a portion of the x axis (which is parallel to the free surface), that

$$\int_S (n_i \sigma_{ij}^{(1)}) u_j^{(2)} dS = \int_S (n_i \sigma_{ij}^{(2)}) u_j^{(1)} dS \quad (\text{C.1})$$

Here the origin of the y -axis is a distance h below the free surface, and the closed contour S runs along $y = 0^\pm$ along the length of the cut. We consider cases of balanced tractions along $y = 0^\pm$ so that, for $i = x, y$, $\sigma_{yi}(x, 0^+) = \sigma_{yi}(x, 0^-) \equiv \sigma_{yi}(x)$ along that contour. Then, defining displacement discontinuities $\delta_i(x) \equiv u_i(x, 0^+) - u_i(x, 0^-)$ along the cut, reciprocity requires

$$\begin{aligned} & \int_{-\infty}^{\infty} [\sigma_{yx}^{(1)}(x) \delta_x^{(2)}(x) + \sigma_{yy}^{(1)}(x) \delta_y^{(2)}(x)] dx = \\ & \int_{-\infty}^{\infty} [\sigma_{yx}^{(2)}(x) \delta_x^{(1)}(x) + \sigma_{yy}^{(2)}(x) \delta_y^{(1)}(x)] dx \end{aligned} \quad (\text{C.2})$$

(with the integrands vanishing here and below for positions x outside the cut).

The stresses $\sigma_{yi}(x)$ due to continuous distributions of dislocations of the types in Figure C.1a and b, with local densities $-d\delta_k(x)/dx$ over the domain $-\infty < x < \infty$, have the form

$$\sigma_{yi}(x) = \frac{\mu}{2\pi(1-\nu)} \int_{-\infty}^{\infty} \left[\frac{1}{t-x} \frac{d\delta_i(t)}{dt} + K_{ij}(t-x) \frac{d\delta_j(t)}{dt} \right] dt \quad (\text{C.3})$$

While labeling the kernels as $K_{ij}(t - x)$ versus a notation $L_{ij}(x - t)$ is an arbitrary and inconsequential choice, we have chosen to follow the implicit preference of Erdogan [1969].

Choosing $\delta_x^{(2)}(x) = 0$, $\delta_y^{(1)}(x) = 0$ and substituting the relations for stress

$$\begin{aligned} \int_{-\infty}^{\infty} \left[\int_{-\infty}^{\infty} K_{yx}(t - x) \frac{d\delta_x^{(1)}(t)}{dt} dt \right] \delta_y^{(2)}(x) dx = \\ \int_{-\infty}^{\infty} \left[\int_{-\infty}^{\infty} K_{xy}(t - x) \frac{d\delta_y^{(2)}(t)}{dt} dt \right] \delta_x^{(1)}(x) dx \end{aligned} \quad (\text{C.4})$$

Integrating the innermost integrals by parts, noting that the kernels must vanish as $|t - x| \rightarrow \infty$, and assuming that $\delta_x^{(1)}(t)$, $\delta_y^{(2)}(t)$ are bounded as $t \rightarrow \pm\infty$,

$$\begin{aligned} \int_{-\infty}^{\infty} \left[\int_{-\infty}^{\infty} K'_{yx}(t - x) \delta_x^{(1)}(t) dt \right] \delta_y^{(2)}(x) dx = \\ \int_{-\infty}^{\infty} \left[\int_{-\infty}^{\infty} K'_{xy}(t - x) \delta_y^{(2)}(t) dt \right] \delta_x^{(1)}(x) dx \end{aligned} \quad (\text{C.5})$$

where $K'_{ij}(\theta) = dK_{ij}(\theta)/d\theta$. Switching the symbols for the integration variables x and t on the left hand side and rearranging

$$\int_{-\infty}^{\infty} \int_{-\infty}^{\infty} \delta_x^{(1)}(x) \delta_y^{(2)}(t) [K'_{xy}(t - x) - K'_{yx}(x - t)] dt dx = 0 \quad (\text{C.6})$$

That equation must be satisfied for an arbitrary choice of the functions in the product $\delta_x^{(1)}(x) \delta_y^{(2)}(t)$, requiring that

$$K'_{xy}(t - x) = K'_{yx}(x - t) \quad (\text{C.7})$$

Then noting that $K'_{xy}(\theta) - K'_{yx}(-\theta) = 0$ is equivalent to $d[K_{xy}(\theta) + K_{yx}(-\theta)]/d\theta = 0$,

we conclude that

$$K_{xy}(t-x) = -K_{yx}(x-t) \quad (\text{C.8})$$

C.3 SYMMETRY

To further sharpen the constraint of Equation 8, consider the two cases

$$\delta_x^{(1)}(x) = -\frac{b_x}{2} \frac{x}{|x|}, \quad \delta_y^{(2)}(x) = -\frac{b_y}{2} \frac{x}{|x|} \quad \text{for } |x| > 0 \quad (\text{C.9})$$

with $\delta_x^{(1)}(0) = \delta_y^{(2)}(0) = 0$, and with $\delta_y^{(1)}(x) = \delta_x^{(2)}(x) = 0$ for all x . These describe a classical edge dislocation line running perpendicular to the x, y plane through its origin, i.e., along the z direction, with Burgers vector components b_x in case (1) and b_y in case (2). The stress field created in case (1) is equivalent to that produced by insertion of a sliver of material of thickness b_x along the portion of the y, z plane corresponding to $y > 0$ (Figure C.1a). That created in case (2) is equivalent to that produced by insertion of a sliver of thickness b_y along the portion of the x, z plane corresponding to $x < 0$ (Figure C.1b).

The resulting stresses on $y = 0$ in the two cases are, by Equation 3,

$$\sigma_{yx}^{(1)}(x) = \frac{\mu b_x}{2\pi(1-\nu)} \left[\frac{1}{x} - K_{xx}(-x) \right], \quad \sigma_{yy}^{(1)}(x) = -\frac{\mu b_x}{2\pi(1-\nu)} K_{yx}(-x) \quad (\text{C.10})$$

$$\sigma_{yx}^{(2)}(x) = -\frac{\mu b_y}{2\pi(1-\nu)} K_{xy}(-x), \quad \sigma_{yy}^{(2)}(x) = \frac{\mu b_y}{2\pi(1-\nu)} \left[\frac{1}{x} - K_{yy}(-x) \right] \quad (\text{C.11})$$

Case (1) has mirror symmetry about the y, z plane, $u_y^{(1)}(x, y) = u_y^{(1)}(-x, y)$, $u_x^{(1)}(x, y) = -u_x^{(1)}(-x, y)$, so that $\sigma_{yx}^{(1)}(+x) = -\sigma_{yx}^{(1)}(-x)$ and $\sigma_{yy}^{(1)}(+x) = \sigma_{yy}^{(1)}(-x)$, assuring that

$$K_{xx}(-x) = -K_{xx}(+x) \quad \text{and} \quad K_{yx}(-x) = K_{yx}(+x) \quad (\text{C.12})$$

Case (2) has pure antisymmetry about that y, z plane, requiring that $u_x^{(2)}(x, y) = u_x^{(2)}(-x, y)$, $u_y^{(2)}(x, y) = -u_y^{(2)}(-x, y)$, so that $\sigma_{yx}^{(2)}(+x) = \sigma_{yx}^{(2)}(-x)$ and $\sigma_{yy}^{(2)}(+x) = -\sigma_{yy}^{(2)}(-x)$, assuring that

$$K_{xy}(-x) = K_{xy}(+x) \quad \text{and} \quad K_{yy}(+x) = -K_{yy}(-x) \quad (\text{C.13})$$

Thus both $K_{xy}(t - x)$ and $K_{yx}(t - x)$ are *even* functions of $t - x$ and our previous deduction that $K_{xy}(t - x) = -K_{yx}(x - t)$ can be rewritten as

$$K_{xy}(t - x) = -K_{yx}(t - x) \quad (\text{C.14})$$

Reverting to the opening discussion, this result, based only on elastic reciprocity and symmetry, clearly shows that the *opposite* alternative must be the correct one. This result is not restricted to the coordinate choice of Figure C.1, as we show next.

C.4 COORDINATE CHANGES

Given $K_{ij}(\theta)$ for a particular choice of coordinates x, y , the components $K_{\tilde{i}\tilde{j}}(\theta)$ may be determined for an alternative choice \tilde{x}, \tilde{y} . Consider the coordinates $\tilde{x} = -x$, $\tilde{y} = -y$ [e.g., Erdogan, 1969; Erdogan et al., 1973; Figure C.2], for which the displacement discontinuities are $\delta_i(\tilde{x}) = u_i^+(\tilde{x}, 0^+) - u_i^-(\tilde{x}, 0^-)$ for $i = \tilde{x}, \tilde{y}$, and the stress components take the form

$$\sigma_{\tilde{y}\tilde{i}}(\tilde{x}) = \frac{\mu}{2\pi(1-\nu)} \int_{-\infty}^{\infty} \left[\frac{1}{\tilde{t} - \tilde{x}} \frac{d\delta_i(\tilde{t})}{d\tilde{t}} + K_{\tilde{i}\tilde{j}}(\tilde{t} - \tilde{x}) \frac{d\delta_j(\tilde{t})}{d\tilde{t}} \right] d\tilde{t} \quad (\text{C.15})$$

We note that $\delta_{\tilde{x}}(-x) = \delta_x(x)$ and $\delta_{\tilde{y}}(-x) = \delta_y(x)$ and that $\sigma_{\tilde{y}\tilde{x}}(-x) = \sigma_{yx}(x)$, and $\sigma_{\tilde{y}\tilde{y}}(-x) = \sigma_{yy}(x)$. Using these relations for displacement discontinuities and

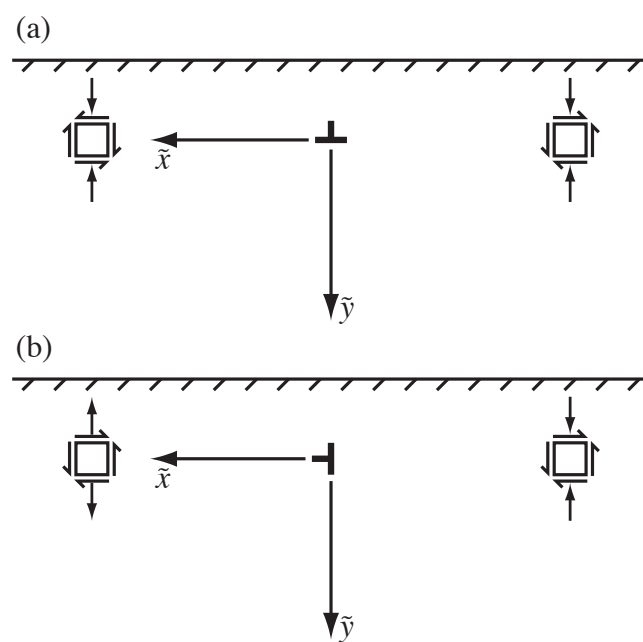


Figure C.2: Elements along the \tilde{x} -axis and at symmetric points about the \tilde{y} -axis indicate stress ($\sigma_{\tilde{x}\tilde{x}}$ omitted) due to an edge dislocation with Burgers vector (a) parallel and (b) perpendicular to a free surface a distance h away.

stress components between the two coordinate systems, the coordinate transformations themselves, and the anticipated even or odd nature of $K_{\tilde{i}\tilde{j}}(\theta)$, we may transform the expression for $\sigma_{\tilde{y}\tilde{i}}(\tilde{x})$ as an integral over \tilde{t} (Equation 15) to an expression for $\sigma_{y\iota}(x)$ as an integral over t . Doing so and comparing the resulting expression with Equation 3, we find the relation between the nonsingular kernels: $K_{\iota\jmath}(\theta) = K_{\tilde{i}\tilde{j}}(\theta)$ for $\iota = \jmath$ and $K_{\iota\jmath}(\theta) = -K_{\tilde{i}\tilde{j}}(\theta)$ for $\iota \neq \jmath$. (Here the notation is such that if $\iota = x$, then $\tilde{\iota} = \tilde{x}$, etc.) That both $K_{xy}(\theta)$ and $K_{yx}(\theta)$ transform into the new coordinate system with the same sign preserves the conclusion of the previous section: $K_{\tilde{x}\tilde{y}}(\theta) = -K_{\tilde{y}\tilde{x}}(\theta)$.

This indicates that the solution proposed in Erdogan [1969] and Erdogan et al. [1973], in which $K_{\tilde{x}\tilde{y}}(\theta) = K_{\tilde{y}\tilde{x}}(\theta)$, must require correction, presumably due to an unnoticed sign error in transcription from notes or in derivation. From the above analysis alone, it is not possible to determine which of the two terms requires a sign change to arrive at $K_{\tilde{x}\tilde{y}}(\theta) = -K_{\tilde{y}\tilde{x}}(\theta)$. However, using a correct solution in another coordinate set [e.g., Head, 1953] and the coordinate transformation above, the appropriate sign change may be determined (following section).

C.5 EXPRESSIONS FOR STRESS DUE TO EDGE DISLOCATIONS UNDER CHANGE OF COORDINATES, BURGERS VECTOR CONVENTION

For the coordinates of Figure C.1 and the positive Burgers vector convention represented by cases (1) and (2) [e.g., as in Thouless et al., 1987], stresses along $y = 0$

are

$$\frac{\sigma_{yx}^{(1)}(x) + \sigma_{yx}^{(2)}(x)}{\mu / [2\pi(1-\nu)]} = b_x \left[\frac{1}{x} - \frac{x}{4h^2 + x^2} + \frac{8h^2x}{(4h^2 + x^2)^2} + \frac{4h^2x^3 - 48h^4x}{(4h^2 + x^2)^3} \right] + b_y \left[\frac{24h^3x^2 - 32h^5}{(4h^2 + x^2)^3} \right] \quad (\text{C.16})$$

$$\frac{\sigma_{yy}^{(2)}(x) + \sigma_{yy}^{(1)}(x)}{\mu / [2\pi(1-\nu)]} = b_y \left[\frac{1}{x} - \frac{x}{4h^2 + x^2} - \frac{8h^2x}{(4h^2 + x^2)^2} + \frac{4h^2x^3 - 48h^4x}{(4h^2 + x^2)^3} \right] + b_x \left[-\frac{24h^3x^2 - 32h^5}{(4h^2 + x^2)^3} \right] \quad (\text{C.17})$$

Comparing the above to eqs. (C.10–C.11), the components $K_{ij}(\theta)$ are

$$\begin{aligned} K_{xx}(\theta) &= -\frac{\theta}{4h^2 + \theta^2} + \frac{8h^2\theta}{(4h^2 + \theta^2)^2} + \frac{4h^2\theta^3 - 48h^4\theta}{(4h^2 + \theta^2)^3} \\ K_{xy}(\theta) &= -\frac{24h^3\theta^2 - 32h^5}{(4h^2 + \theta^2)^3} \\ K_{yy}(\theta) &= -\frac{\theta}{4h^2 + \theta^2} - \frac{8h^2\theta}{(4h^2 + \theta^2)^2} + \frac{4h^2\theta^3 - 48h^4\theta}{(4h^2 + \theta^2)^3} \\ K_{yx}(\theta) &= \frac{24h^3\theta^2 - 32h^5}{(4h^2 + \theta^2)^3} \end{aligned} \quad (\text{C.18})$$

The solution for the coordinates \tilde{x} , \tilde{y} of the Erdogan 1969 and 1973 papers is then correctly given, using the transformation $K_{\tilde{x}\tilde{y}}(\theta) = -K_{xy}(\theta)$, $K_{\tilde{y}\tilde{x}}(\theta) = -K_{yx}(\theta)$, and $K_{\tilde{x}\tilde{x}}(\theta) = K_{xx}(\theta)$, $K_{\tilde{y}\tilde{y}}(\theta) = K_{yy}(\theta)$, as

$$K_{\tilde{x}\tilde{y}}(\theta) = -K_{\tilde{y}\tilde{x}}(\theta) = \frac{24h^3\theta^2 - 32h^5}{(4h^2 + \theta^2)^3} \quad (\text{C.19})$$

with on-diagonal $K_{\tilde{i}\tilde{j}}(\theta)$ as above, whereas previously Erdogan [1969] stated $K_{\tilde{x}\tilde{y}}(\theta) = K_{\tilde{y}\tilde{x}}(\theta) = (24h^3\theta^2 - 32h^5)/(4h^2 + \theta^2)^3$. Erdogan [1971], using the same coordinates, is in agreement with these $K_{\tilde{i}\tilde{j}}(\theta)$ provided the sign is changed for each of his kernel terms. That is appropriate for $K_{\tilde{x}\tilde{x}}$ and $K_{\tilde{y}\tilde{y}}$ because he reversed the sign convention

for these terms in the 1971 paper, but not for $K_{\tilde{x}\tilde{y}}$ and $K_{\tilde{y}\tilde{x}}$. If we speculate that such was a misprint and that he intended to reverse the sign convention for the off-diagonal terms too, then results of his 1971 paper would be fully verified.

Table C.1: Mode-I and -II stress intensity factors for a plane-strain, surface-parallel crack under uniform pressure.

h/a	$K_I/(p\sqrt{\pi a})$	$K_{II}/(p\sqrt{\pi a})$
0.001	15146	8952.4
0.01	370.81	282.93
0.1	14.007	8.8119
1	1.5110	0.1849
10	1.0075	0.0004
100	1.0000	0.0000
1000	1.0000	0.0000

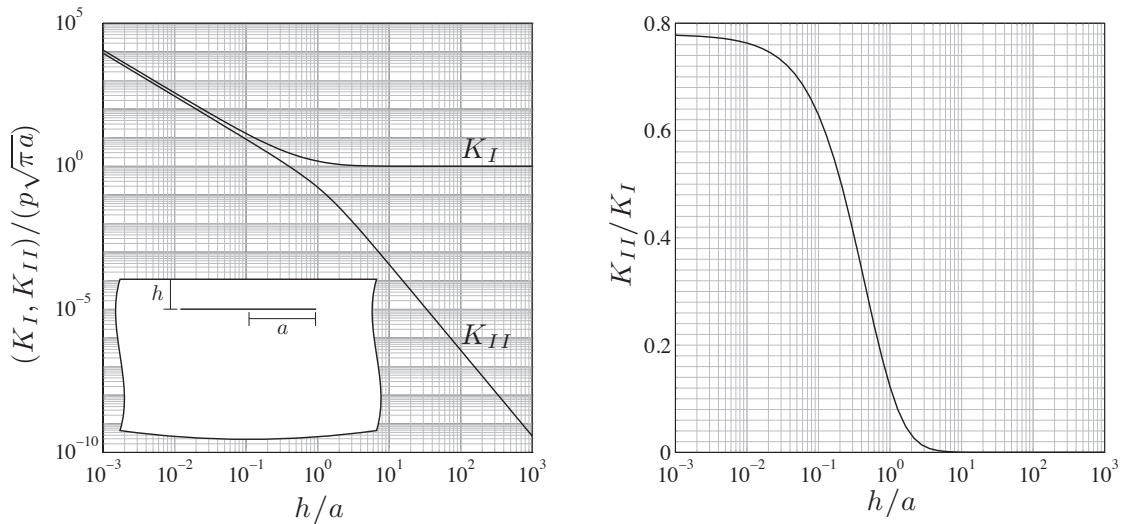


Figure C.3: Mode-I and -II stress intensity factors due to the uniform pressurization, with pressure p of a plane-strain crack of half-length a lying parallel to a free surface a distance h away.

C.6 STRESS INTENSITY FACTORS FOR A UNIFORMLY PRESSURIZED SUBSURFACE CRACK

Returning to the problem that highlighted the discrepancy, that of the uniformly pressurized subsurface crack, we calculate the correct stress intensity factors. We plot and tabulate the results against relative depth in Figure C.3 and Table C.1.

APPENDIX D

INELASTIC CONSTITUTIVE PROPERTIES IN THE DEFORMATION OF SATURATED POROUS MEDIA

This appendix outlines and gives in somewhat greater detail the arguments presented in an extended abstract [Rice, 1977], drawing on the constitutive methodology of Rice [1971, 1975a], and providing some constraints on representing plastic strain and porosity changes in fluid-saturated geo-materials. The focus is on a representative volume of material that is undergoing locally heterogeneous inelastic deformation by frictional slip on contacting fissure surfaces and by open microcrack growth. The macroscopic average stress, σ_{ij} , acting on the locally heterogeneous material can be regarded as determined by its macroscopic average strain, ϵ_{ij} , its pore pressure, p , and the current state of locally heterogeneous inelastic slip on fissures and microcracking within the representative volume of material. The latter array of microscale variables is represented symbolically by H ; it would be impossible to describe them other than statistically, but the only properties that we need for H are these: when H is fixed (no slip on fissures, no crack growth) during an increment in σ_{ij} , ϵ_{ij} , and p , the relation between those variables corresponds to normal poroelastic response. When there is an increment in local slip on fissures and/or microcrack growth, we understand there

to be an increment in H , and the overall response is poroelastic-plastic. Thus we can write

$$\sigma_{ij} = \sigma_{ij}(\epsilon_{kl}, p, H) \quad (\text{D.1})$$

where the relation between the variables at fixed H describes a poroelastic relation.

The strain energy $u = u(\epsilon_{kl}, n, H)$ of the solid phase per unit reference state volume of the porous material then satisfies [e.g., Rice and Cleary, 1976], for fixed H ,

$$du = \sigma_{ij} d\epsilon_{ij} + pdn \quad (\text{D.2})$$

Letting $\psi = \psi(\sigma_{ij}, p, H) = \sigma_{ij}\epsilon_{ij} + pn - u$, it then follows that

$$n = \frac{\partial \psi}{\partial p} \quad \epsilon_{ij} = \frac{\partial \psi}{\partial \sigma_{ij}} \quad (\text{D.3})$$

where the derivatives are at fixed H , and hence refer to elastic changes.

We define plastic parts of the variations of functions like the above potential ψ as the change in the value of the potential due to variations in H , but with ψ evaluated for the same σ_{ij} and p

$$d^p\psi = \psi(\sigma_{ij}, p, H + dH) - \psi(\sigma_{ij}, p, H) \quad (\text{D.4})$$

The plastic part [see Rice, 1971] of porosity and strain increments are $d^p n = n(\sigma_{ij}, p, H + dH) - n(\sigma_{ij}, p, H)$ and $d^p \epsilon_{ij} = \epsilon_{ij}(\sigma_{ij}, p, H + dH) - \epsilon_{ij}(\sigma_{ij}, p, H)$ and these satisfy

$$d^p n = \frac{\partial (d^p \psi)}{\partial p} \quad d^p \epsilon_{ij} = \frac{\partial (d^p \psi)}{\partial \sigma_{ij}} \quad (\text{D.5})$$

We then let changes in states of microscopic solid inelastic deformation H and $H +$

dH be characterized by incremental internal variables $d\xi_k$ with corresponding work-conjugate forces $f_k(\sigma_{ij}, p, H)$ such that the sum of their products when averaged over a representative macroscopic volume (where $\langle \dots \rangle$ represents the volume average of the quantity within the brackets) is

$$\langle f_k d\xi_k \rangle = d^p \psi \quad (\text{D.6})$$

Consequently, from (D.5) and (D.6) the plastic variations of the strain and porosity are given by

$$d^p n = \langle \frac{\partial f_k}{\partial p} \delta \xi_k \rangle \quad d^p \epsilon_{ij} = \langle \frac{\partial f_k}{\partial \sigma_{ij}} \delta \xi_k \rangle \quad (\text{D.7})$$

When considering a saturated, fissured rock mass or granular material, inelastic deformation may take the form of crack extension and frictional sliding along fissure surfaces. As introduced in Rice [1975a], the volume average representation of $d^p \epsilon_{ij}$ in the case of microcrack extension within a representative volume V includes an integration over all crack front arcs (Γ_c), with arclength s , of the local fracture energy release \mathcal{G}_{loc} per unit advance of the crack area times the advance area $\delta a(s)ds$

$$\langle \frac{\partial f_k}{\partial \sigma_{ij}} \delta \xi_k \rangle = \frac{1}{V} \int_{\Gamma_c} \frac{\partial \mathcal{G}_{loc}(\sigma_{ij}, p, H)}{\partial \sigma_{ij}} \delta a(s) ds \quad (\text{D.8})$$

Similarly, in the case of frictional sliding along fissure surfaces S_f , which experience local slip increments $\delta(\Delta u)$ and over which local shear stress τ acts in the slip direction, the volume average representation of $d^p \epsilon_{ij}$ in (D.7) can be expressed as

$$\langle \frac{\partial f_k}{\partial \sigma_{ij}} \delta \xi_k \rangle = \frac{1}{V} \int_{S_f} \frac{\partial \tau(\sigma_{ij}, p, H)}{\partial \sigma_{ij}} \delta(\Delta u) dS \quad (\text{D.9})$$

Now, we consider porous materials for which all pore spaces are in matter com-

munication with the pore fluid and for which all of the solid phase has an identical isotropic elastic response to local increments in isotropic stress. The same special materials are considered for estimating some of the constants of poroelasticity [Nur and Byerlee, 1971; Rice and Cleary, 1976]. In those materials simultaneous macroscopic stress and pore pressure increments of the form

$$d\sigma_{ij} = -\delta_{ij}dP \quad dp = dP, \quad (\text{D.10})$$

result in a uniform, isotropic local stress increment $d\sigma_{ij}^{local} = -\delta_{ij}dP$ at each microscale point of the solid phase. (σ_{ij}^{local} is of course not equal to the macroscopic stress σ_{ij} , but increments in $d\sigma_{ij}^{local}$, when H is fixed, will be linearly proportional to increments $d\sigma_{ij}$ and dp , with local coefficients in that proportionality constrained by the requirement $d\sigma_{ij}^{local} = -dP\delta_{ij}$ in the case of (D.10).) Such isotropic changes in local stress do not alter local stress τ or effective normal stress on fissures and, because they leave local crack tip singular stress fields unaffected, they do not alter the local \mathcal{G} . Thus such increments would not cause a change in the work-conjugate forces f discussed above. Neither would they induce a further increment of plastic deformation, because they would not slip a fissure surface (if governed by normal concepts of effective stress) nor grow a crack if its growth is controlled by \mathcal{G} .

The increments $d\sigma_{ij}$ and dp considered are, of course, exactly those which cause no change in the macroscopic Terzaghi effective stress,

$$\sigma'_{ij} = \sigma_{ij} + p\delta_{ij} \quad (\text{D.11})$$

and therefore their induction of no further plastic deformation means that the Terzaghi stress is the appropriate stress controlling macroscopic inelastic strain increments.

An additional result of the force conjugate to microscopic inelastic deformation, $f(\sigma_{ij}, p, H)$, remaining unaffected by stress increments in the form of (D.10) is that

$$df = \frac{\partial f}{\partial \sigma_{ij}} d\sigma_{ij} + \frac{\partial f}{\partial p} dp = \left(-\frac{\partial f}{\partial \sigma_{ij}} \delta_{ij} + \frac{\partial f}{\partial p} \right) dP = 0 \quad (\text{D.12})$$

for an arbitrary increment dP . Hence, the term within the parentheses must be identically zero. Using (D.12) and (D.7) we find that

$$d^p \epsilon_{kk} = d^p n \quad (\text{D.13})$$

i.e., plastic dilatancy is an inelastic increase in porosity.

APPENDIX E

DERIVATION OF EFFECTIVE MATERIAL PARAMETERS FOR UNDRAINED BEHAVIOR

When the stress state reaches a prescribed yield criterion, the material can deform plastically. The yield criterion is defined by the the yield function F , such that $F = 0$ when the material deforms plastically. The yield function for the Drucker-Prager criterion, as introduced in Templeton and Rice [2008] except here explicitly evaluated in terms of the Terzaghi effective stress, is

$$F = \bar{\tau} + \mu \left(\frac{\sigma_{kk}}{3} + p \right) - d \quad (\text{E.1})$$

Any hardening or softening of the material due to inelastic deformation is reflected by the movement of the yield surface in stress space. To ensure that the stress state continues to be on the yield surface during hardening, the stress state must satisfy $\dot{F} = 0$

$$\dot{\tau} + \mu \left(\frac{\dot{\sigma}_{kk}}{3} + \dot{p} \right) = \dot{d} - \dot{\mu} \left(\frac{\sigma_{kk}}{3} + p \right) \quad (\text{E.2})$$

The terms \dot{b} and $\dot{\mu}$ on the right hand side of (E.2) are the evolution of the yield criterion parameters. We define a hardening term h such that

$$\dot{b} - \dot{\mu} \left(\frac{\sigma_{kk}}{3} + p \right) = h\dot{\gamma}^{pl} \quad (\text{E.3})$$

where $\dot{\gamma}^{pl}$ is the rate of the equivalent plastic shear strain (γ^{pl}) and, for conciseness, used to represent what was $d^p\gamma/dt$ in Templeton and Rice [2008]

$$\dot{\gamma}^{pl} = \sqrt{2 \left(\mathcal{D}_{ij}^p - \frac{1}{3} \delta_{ij} \mathcal{D}_{kk}^p \right) \left(\mathcal{D}_{ij}^p - \frac{1}{3} \delta_{ij} \mathcal{D}_{mm}^p \right)} \quad (\text{E.4})$$

Here if we take μ to be constant, then $\dot{\mu} = 0$ and the evolution of the yield surface results from changes in the cohesion b and is given by

$$\dot{b} = h\dot{\gamma}^{pl} \quad (\text{E.5})$$

From (E.2) and (E.3),

$$\dot{\gamma}^{pl} = \frac{1}{h} \left(\dot{\tau} + \mu \left(\frac{\dot{\sigma}_{kk}}{3} + \dot{p} \right) \right) \quad (\text{E.6})$$

and combining (3.19) and (E.6)

$$\dot{\gamma}^{pl} = \frac{1}{h + \mu\beta KB/\alpha} \left(\dot{\tau} + (1 - B)\mu \left(\frac{\dot{\sigma}_{kk}}{3} \right) \right) \quad (\text{E.7})$$

This equation defines the effective internal friction parameter μ_u and effective hardening parameter h_u as

$$\mu_u = (1 - B)\mu \quad h_u = h + \frac{\mu\beta KB}{\alpha} \quad (\text{E.8})$$

Undrained conditions introduce a new internal friction parameter, μ_u . Under such conditions, changes in the deviatoric portion of the stress alone will not result in changes in pore pressure; therefore, the yield point above a given initial effective isotropic stress on a plot as in Figure 3.2 remains unchanged from yield point under drained conditions for the same initial effective isotropic stress. However, the introduction of μ_u necessitates the introduction of a corresponding effective cohesion, b_u .

$$b_u = b - B\mu\sigma_{kk}^o/3 \quad (\text{E.9})$$

Thus, under undrained conditions the yield criterion F becomes

$$F = \bar{\tau} + \mu_u \left(\frac{\sigma_{kk}}{3} \right) - b_u \quad (\text{E.10})$$

Additionally, because the hardening h is replaced by an undrained value h_u , from eqs. (E.2), (E.7), (E.9) and taking μ to be constant,

$$\dot{b}_u = h_u \dot{\gamma}^{pl} \quad (\text{E.11})$$

Since plastic dilatancy changes (reduces) pore pressure, there is some feedback from plastic dilatation on the elastic strains. This is accounted for by expressing the elastic strain rate as the sum of the regular undrained elastic response \mathcal{D}_{ij}^{Re} , plus a correction to account for pore pressure changes due to plastic dilatancy \mathcal{D}_{ij}^{Pe} :

$$\mathcal{D}_{ij}^e = \mathcal{D}_{ij}^{Re} + \mathcal{D}_{ij}^{Pe} \quad (\text{E.12})$$

where the regular undrained elastic response is expressed in (3.7). For positive plastic dilatancy, the reduction in pore pressure will have the effect of reducing the elastic

strain. This is accounted for in $\mathcal{D}_{ij}^{P_e}$ by

$$\mathcal{D}_{kk}^{P_e} = -\frac{\alpha}{K} \left[\frac{KB}{\alpha} \beta \frac{\dot{\tau} + \mu(1-B)\dot{\sigma}_{kk}/3}{h + \mu\beta KB/\alpha} \right] \quad (\text{E.13})$$

where the term inside the brackets is the term in (3.19) giving the increment in pore pressure due to plastic dilatancy.

Consequently, we define a contribution of plastic dilatancy to strain as a sum of changes in strain due to the plastic dilatancy itself and the feedback effect this dilatancy has on elastic strains:

$$\mathcal{D}_{kk}^p + \mathcal{D}_{kk}^{P_e} = (1-B)\beta \frac{\dot{\tau} + \mu(1-B)\dot{\sigma}_{kk}/3}{h + \mu\beta KB/\alpha} \quad (\text{E.14})$$

and we can thus define the effective plastic dilatancy as:

$$\beta_u = (1-B)\beta \quad (\text{E.15})$$

BIBLIOGRAPHY

- ABAQUS, Inc., 2005. ABAQUS Theory Manual, version 6.5. Providence, R.I.
- Ampuero, J.-P., Ripperger, J., Mai, P. M., 2006. Properties of dynamic earthquake ruptures with heterogeneous stress drop. In: McGarr, A., Abercrombie, R. E., Kanamori, H., Di Toro, G. (Eds.), Radiated Energy and the Physics of Earthquakes. Geophysical Monograph Series 170, American Geophysical Union, Washington, D. C., pp. 255–261.
- Ampuero, J.-P., Rubin, A. M., Jan. 2008. Earthquake nucleation on rate and state faults – Aging and slip laws. *J. Geophys. Res.* 113, B01302.
- Andrews, B. D., Brothers, L. L., Barnhardt, W. A., 2010. Automated feature extraction and spatial organization of seafloor pockmarks, Belfast Bay, Maine, USA. *Geomorphology* 124 (1-2), 55–64.
- Andrews, D. J., 1976. Rupture velocity of plane strain shear cracks. *J. Geophys. Res.* 81 (32), 5679–5687.
- Andrews, D. J., Apr. 1985. Dynamic plane-strain shear rupture with a slip-weakening friction law calculated by a boundary integral method. *B. Seismol. Soc. Am.* 75 (1), 1–21.
- Andrews, D. J., 2002. A fault constitutive relation accounting for thermal pressurization of pore fluid. *J. Geophys. Res.* 107 (B12), 2363.
- Andrews, D. J., 2005. Rupture dynamics with energy loss outside the slip zone. *J. Geophys. Res.* 110, B01307.
- Ashbaugh, N., 1975. Stress solution for a crack at an arbitrary angle to an interface. *Int. J. Fract.* 11 (2), 205–219.
- Bazant, Z. P., Zi, G. S., McClung, D., 2003. Size effect law and fracture mechanics of the triggering of dry snow slab avalanches. *J. Geophys. Res.* 108 (B2), 2119.
- Ben-Zion, Y., Shi, Z., 2005. Dynamic rupture on a material interface with spontaneous generation of plastic strain in the bulk. *Earth Planet. Sc. Lett.* 236 (1-2), 486–496.

- Benallal, A., Comi, C., 2002. Material instabilities in inelastic saturated porous media under dynamic loadings. *Int. J. Solids Struct.* 39, 3693–3716.
- Benallal, A., Comi, C., May 2003. Perturbation growth and localization in fluid-saturated inelastic porous media under quasi-static loadings. *J. Mech. Phys. Solids* 51 (5), 851–899.
- Bennett, R. H., Burns, J. T., Clarke, T. L., 1982. Piezometer probes for assessing effective stress and stability in submarine sediments. NATO Scientific Affairs Division Workshop, Algarve, Portugal, 1980, Plenum Pub. Corp., New York, pp. 129–161.
- Berndt, C., Mienert, J., Vanneste, M., Bünz, S., 2005. Gas hydrate dissociation and seafloor collapse in the wake of the Storegga Slide, Norway. In: Wandas, W. T. G., Nystuen, J. P., Eide, E., Gradstein, F. M. (Eds.), *Onshore-Offshore Relationships on the North Atlantic Margin*. Norwegian Petroleum Society Special Publication, Vol. 12, Elsevier, pp. 285–292.
- Bilby, B. A., Eshelby, J. D., 1968. Dislocations and the theory of fracture. In: Liebowitz, H. (Ed.), *Fracture, An Advanced Treatise*. Academic, San Diego, Calif., pp. 99–182.
- Biot, M. A., 1941. General theory of three-dimensional consolidation. *J. Appl. Phys.* 12 (2), 155–164.
- Bishop, A. W., 1971. Influence of progressive failure on the choice of the method of stability analysis. *Géotechnique* 21 (2), 168–172.
- Bizzarri, A., 2010. How to Promote Earthquake Ruptures: Different Nucleation Strategies in a Dynamic Model with Slip-Weakening Friction. *B. Seismol. Soc. Am.* 100 (3), 923–940.
- Bizzarri, A., Cocco, M., 2006. A thermal pressurization model for the spontaneous dynamic rupture propagation on a three-dimensional fault: 2. Traction evolution and dynamic parameters. *J. Geophys. Res.* 111, B05304.
- Bjerrum, L., 1967. Progressive failure in slopes of overconsolidated plastic clay and clay shales. *J. Soil Mech. Found. Div. ASCE* 93, 3–49.
- Bjerrum, L., Lo, K. Y., 1963. Effect of aging on the shear-strength properties of a normally consolidated clay. *Géotechnique* 13 (2), 147–157.
- Blum, J. A., Chadwell, C. D., Driscoll, N., Zumberge, M. A., 2010. Assessing slope stability in the Santa Barbara Basin, California, using seafloor geodesy and CHIRP seismic data. *Geophys. Res. Lett.* 37 (13).

- Brace, W. F., Paulding, B. W., Scholz, C., 1966. Dilatancy in fracture of crystalline rocks. *J. Geophys. Res.* 71 (16), 3939–3953.
- Bünz, S., Mienert, J., Berndt, C., 2003. Geological controls on the Storegga gas-hydrate system of the mid-Norwegian continental margin. *Earth Planet. Sc. Lett.* 209 (3-4), 291–307.
- Canals, M., Lastras, G., Urgeles, R., Casamor, J., Mienert, J., Cattaneo, A., Debatist, M., Haflidason, H., Imbo, Y., Laberg, J., 2004. Slope failure dynamics and impacts from seafloor and shallow sub-seafloor geophysical data: case studies from the COSTA project. *Mar. Geol.* 213 (1-4), 9–72.
- Carrubba, P., Del Fabbro, M., 2008. Laboratory investigation on reactivated residual strength. *J Geotech Geoenviron* 134 (3), 302–315.
- Cathles, L. M., Su, Z., Chen, D., 2010. The physics of gas chimney and pockmark formation, with implications for assessment of seafloor hazards and gas sequestration. *Marine and Petroleum Geology* 27 (1), 82–91.
- Chen, S. H., Keer, L. M., Achenbach, J. D., 1980. Steady motion of a crack parallel to a bond-plane. *Int. J. Eng. Sci.* 18 (1), 225–238.
- Cleary, M. P., Rice, J. R., 1974. Some elementary models for the growth of slip-surfaces in progressive failure. Tech. rep., MRL E-91, Material Sciences Program, Division of Engineering, Brown Univ., Providence, Rhode Island.
- Cooper, M. R., Bromhead, E. N., Petley, D. J., Grant, D. I., 1998. The Selborne cutting stability experiment. *Géotechnique* 48 (1), 83–101.
- Corbett, D. R., McKee, B., Mead, A., 2006. Nature of decadal-scale sediment accumulation on the western shelf of the Mississippi River delta. *Continental Shelf Research* 26 (17-18), 2125–2140.
- de Borst, R., Réthoré, J., Abellan, M.-A., 2006. A numerical approach for arbitrary cracks in a fluid-saturated medium. *Arch. Appl. Mech.* 75 (10-12), 595–606.
- Dieterich, J. H., 1992. Earthquake Nucleation on Faults with Rate-Dependent and State-Dependent Strength. In: *Tectonophysics*. pp. 115–134.
- Duan, B., Day, S. M., 2008. Inelastic strain distribution and seismic radiation from rupture of a fault kink. *J. Geophys. Res.*, B12113.
- Dugan, B., Flemings, P. B., 2000. Overpressure and fluid flow in the New Jersey continental slope: Implications for slope failure and cold seeps. *Science* 289 (5477), 288–291.

- Dundurs, J., Sendecky, G. P., 1965. Behavior of an edge dislocation near a bimetallic interface. *J. Appl. Phys.* 36 (10), 3353–3354.
- Dunham, E. M., Belanger, D., Cong, L., Kodzon, J. E., 2011a. Earthquake ruptures with strongly rate-weakening friction and off-fault plasticity: 1. Planar faults. *B. Seismol. Soc. Am.*
- Dunham, E. M., Belanger, D., Cong, L., Kodzon, J. E., 2011b. Earthquake ruptures with strongly rate-weakening friction and off-fault plasticity: 2. Nonplanar faults. *B. Seismol. Soc. Am.* in press.
- Dunham, E. M., Rice, J. R., 2008. Earthquake slip between dissimilar poroelastic materials. *J. Geophys. Res.* 113, B09304.
- Dyskin, A. V., Germanovich, L. N., Ustinov, K. B., 2000. Asymptotic analysis of crack interaction with free boundary. *Int. J. Solids Struct.* 37 (6), 857–886.
- Edwards, B. D., Lee, H. J., Field, M. E., 1995. Mudflow Generated by Retrogressive Slope Failure, Santa-Barbara Basin, California Continental Borderland. *J. Sediment. Res.* A65 (1), 57–68.
- Erdogan, F., 1969. Approximate solutions of systems of singular integral equations. *SIAM J. Appl. Math.* 17 (6), 1041–1059.
- Erdogan, F., 1971. Bonded dissimilar materials containing cracks parallel to the interface. *Eng. Fract. Mech.* 3, 231–240.
- Erdogan, F., Gupta, G. D., 1972. On the numerical solution of singular integral equations. *Q Appl Math* 289, 288–291.
- Erdogan, F., Gupta, G. D., Cook, T. S., 1973. Numerical solutions of singular integral equations. In: Sih, G. (Ed.), *Mechanics of Fracture: Method of Analysis and Solution of Crack Problems*. Noordhoff Int. Pub., Leyden, Netherlands, pp. 368–425.
- Flemings, P. B., Liu, X. L., Winters, W., 2003. Critical pressure and multiphase flow in Blake Ridge gas hydrates. *Geology* 31 (12), 1057–1060.
- Flemings, P. B., Long, H., Dugan, B., Germaine, J., John, C. M., Behrmann, J. H., Sawyer, D., 2008. Pore pressure penetrometers document high overpressure near the seafloor where multiple submarine landslides have occurred on the continental slope, offshore Louisiana, Gulf of Mexico. *Earth Planet. Sc. Lett.* 269 (3-4), 309–325.

- Garagash, D., Germanovich, L. N., Murdoch, L. C., Martel, S. J., Reches, Z., Elsworth, D., Onstott, T. C., 2009. A thermal technique of fault nucleation, growth, and slip. In: EOS Trans. AGU, 90(52), Fall Meet. Suppl., Abstract H23E-0995.
- Garagash, D. I., Germanovich, L. N., 2011. Nucleation of dynamic slip on a pressurized fault. to be subm. to Proc. R. Soc., Ser. A.
- Gay, A., Lopez, M., Berndt, C., Seranne, M., 2007. Geological controls on focused fluid flow associated with seafloor seeps in the Lower Congo Basin. Mar. Geol. 244 (1-4), 68–92.
- Gay, A., Lopez, M., Ondreas, H., Charlou, J., Sermonadaz, G., Cochonat, P., 2006. Seafloor facies related to upward methane flux within a Giant Pockmark of the Lower Congo Basin. Mar. Geol. 226 (1-2), 81–95.
- Gee, M., Gawthorpe, R., Friedmann, J., 2005. Giant striations at the base of a submarine landslide. Mar. Geol. 214 (1-3), 287–294.
- Gerasoulis, A., Srivastav, R. P., 1981. A method for the numerical solution of singular integral equations with a principal value integral. Int. J. Eng. Sci. 19, 1293–1298.
- Gibson, R. E., 1958. The progress of consolidation in a clay layer increasing in thickness with time. Géotechnique 8 (4), 171–183.
- Gomberg, J., Bodin, P., Savage, W., Jackson, M. E., 1995. Landslide Faults and Tectonic Faults, Analogs - the Slumgullion Earthflow, Colorado. Geology 23 (1), 41–44.
- Goren, L., Aharonov, E., Anders, M. H., 2010. The long runout of the Heart Mountain landslide: Heating, pressurization, and carbonate decomposition. J. Geophys. Res. 115, B10210.
- Haacke, R., Westbrook, G., Hyndman, R., 2007. Gas hydrate, fluid flow and free gas: Formation of the bottom-simulating reflector. Earth Planet. Sc. Lett. 261 (3-4), 407–420.
- Han, R., Shimamoto, T., Hirose, T., Ree, J. H., Ando, J. i., 2007. Ultralow Friction of Carbonate Faults Caused by Thermal Decomposition. Science 316 (5826), 878–881.
- Head, A. K., 1953. Edge dislocations in inhomogeneous media. P. Phys. Soc. Lond. B 66 (405), 793–801.
- Heaton, T. H., 1990. Evidence for and implications of self-healing pulses of slip in earthquake rupture. Phys. Earth Planet. In. 64 (1), 1–20.

- Henry, P., 2000. Fluid flow at the toe of the Barbados accretionary wedge constrained by thermal, chemical, and hydrogeologic observations and models. *J. Geophys. Res.* 105 (B11), 25855–25872.
- Higashida, Y., Kamada, K., 1982. Stress-fields around a crack lying parallel to a free-surface. *Int. J. Fract.* 19 (1), 39–52.
- Hok, S., Campillo, M., Cotton, F., Favreau, P., Ionescu, I., 2010. Off-fault plasticity favors the arrest of dynamic ruptures on strength heterogeneity: Two-dimensional cases. *Geophys. Res. Lett.* 37 (2).
- Hornbach, M. J., Saffer, D. M., Holbrook, W. S., 2004. Critically pressured free-gas reservoirs below gas-hydrate provinces. *Nature* 427 (6970), 142–144.
- Ida, Y., 1972. Cohesive force across tip of a longitudinal-shear crack and griffiths specific surface-energy. *J. Geophys. Res.* 77 (20), 3796–3805.
- Iverson, R. M., Reid, M. E., Iverson, N. R., LaHusen, R. G., Logan, M., Mann, J. E., Brien, D. L., 2000. Acute sensitivity of landslide rates to initial soil porosity. *Science* 290 (5491), 513–516.
- Kame, N., 2003. Effects of prestress state and rupture velocity on dynamic fault branching. *J. Geophys. Res.* 108 (B5), 2265.
- Karig, D. E., Ask, M. V. S., 2003. Geological perspectives on consolidation of clay-rich marine sediments. *J. Geophys. Res.* 108 (B4), 2197.
- Kayen, R. E., Lee, H. J., 1991. Pleistocene slope instability of gas hydrate-laden sediment on the Beaufort Sea margin. *Mar. Geotechnol.* 10, 125–141.
- Kilburn, C. R. J., Petley, D. N., 2003. Forecasting giant, catastrophic slope collapse: lessons from Vajont, Northern Italy. *Geomorphology* 54, 21–32.
- Krenk, S., 1975. Use of Interpolation Polynomial for Solutions of Singular Integral-Equations. *Q Appl Math* 32 (4), 479–484.
- Kvenvolden, K. A., 1993. Gas Hydrates - Geological Perspective and Global Change. *Rev. Geophys.* 31 (2), 173–187.
- Lachenbruch, A. H., 1980. Frictional heating, fluid pressure, and the resistance to fault motion. *J. Geophys. Res.* 85, 6097–6112.
- Lambe, T. W., Whitman, R. V., 1969. Soil mechanics. Wiley, New York.
- Lapusta, N., Rice, J. R., Ben-Zion, Y., Zheng, G. T., 2000. Elastodynamic analysis for slow tectonic loading with spontaneous rupture episodes on faults with rate- and state-dependent friction. *J. Geophys. Res.* 105, 23765–23789.

- Liu, X., Flemings, P. B., 2007. Dynamic multiphase flow model of hydrate formation in marine sediments. *J. Geophys. Res.* 112, B03101.
- Long, H., Flemings, P. B., Germaine, J. T., Saffer, D. M., 2008. Data report: consolidation characteristics of sediments from IODP Expedition 308, Ursa Basin, Gulf of Mexico. In: Flemings, P. B., Behrmann, J. H., John, C. M., the Expedition 308 Scientists (Eds.), Proc. IODP 308. Integrated Ocean Drilling Program Management International, Inc., College Station, Tex.
- Martel, S., 2004. Mechanics of landslide initiation as a shear fracture phenomenon. *Mar. Geol.* 203 (3-4), 319–339.
- Mase, C. W., Smith, L., 1987. Effects of frictional heating on the thermal, hydrologic, and mechanical response of a fault. *J. Geophys. Res.* 92, 6249–6272.
- McClung, D. M., 1979. Shear Fracture Precipitated by Strain Softening as a Mechanism of Dry Slab Avalanche Release. *J. Geophys. Res.* 84, 3519–3526.
- McClung, D. M., 2009. Dry snow slab quasi-brittle fracture initiation and verification from field tests. *J. Geophys. Res.* 114, F01022.
- McClure, M., Horne, R., 2010. Modeling slip during fluid injection and production using rate/state friction. In: Abstract H31G-1093 presented at 2010 Fall Meeting, AGU, Sn Francisco, Calif., 13-17 Dec.
- Mitchell, T. M., Faulkner, D. R., 2008. Experimental measurements of permeability evolution during triaxial compression of initially intact crystalline rocks and implications for fluid flow in fault zones. *J. Geophys. Res.* 113, B11412.
- Montgomery, D. R., Schmidt, K. M., Dietrich, W. E., McKean, J., 2009. Instrumental record of debris flow initiation during natural rainfall: Implications for modeling slope stability. *J. Geophys. Res.* 114, F01031.
- Moore, P. L., Iverson, N. R., 2002. Slow episodic shear of granular materials regulated by dilatant strengthening. *Geology* 30 (9), 843–846.
- Muller, J. R., Martel, S. J., 2000. Numerical models of translational landslide rupture surface growth. *Pure appl. geophys.* 157, 1009–1038.
- Murakami, Y. (Ed.), 1987. Stress Intensity Factors Handbook. Vol. 1. Pergamon Press, New York.
- Noda, H., Shimamoto, T., 2005. Thermal pressurization and slip-weakening distance of a fault: An example of the Hanaore Fault, Southwest Japan. *B. Seismol. Soc. Am.* 95 (4), 1224–1233.

- Nur, A., Byerlee, J. D., 1971. Exact effective stress law for elastic deformation of rock with fluids. *J. Geophys. Res.* 76 (26), 6414–6419.
- Ochiai, H., Okada, Y., Furuya, G., Okura, Y., Matsui, T., Sammori, T., Terajima, T., Sassa, K., 2004. A fluidized landslide on a natural slope by artificial rainfall. *Landslides* 1 (3), 211–219.
- Palmer, A. C., Rice, J. R., 1973. Growth of slip surfaces in progressive failure of over-consolidated clay. *P. Roy. Soc. Lond. A Mat.* 332 (1591), 527–548.
- Paynter, R. J. H., Hills, D. A., Sackfield, A., Dec. 2006. The penny crack beneath the surface of a half-space: with application to the blister test. *Int. J. Fract.* 142 (1-2), 173–182.
- Pellegrino, A., Picarelli, L., Urciuoli, G., 2004. Experiences of mudslides in Italy. In: Proc. Int. Workshop on Occurrence and Mechanisms of Flow-Like Landslides in Natural Slopes and Earthfills, May 14-16, 2003, Sorrento, Italy, ed. L. Picarrelli, Patron Editore, Bologna, Italy. pp. 191–206.
- Petley, D. N., Higuchi, T., Petley, D. J., Bulmer, M. H., Carey, J., 2005. Development of progressive landslide failure in cohesive materials. *Geology* 33 (3), 201.
- Picarelli, L., Russo, C., Urciuoli, G., 1995. Modeling earthflows based on experiences. In: Proc. 11th European Conference on Soil Mechanics and Foundation Engineering, Copenhagen, Denmark, 28 May – 1 June 1995, Danish Geotechnical Society, Copenhagen, Denmark. pp. 157–162.
- Picarelli, L., Urciuoli, G., Ramondini, M., Comegna, L., Mar. 2005. Main features of mudslides in tectonised highly fissured clay shales. *Landslides* 2 (1), 15–30.
- Pinet, N., Duchesne, M., Lavoie, D., Bolduc, A., Long, B., 2008. Surface and subsurface signatures of gas seepage in the St. Lawrence Estuary (Canada): Significance to hydrocarbon exploration. *Marine and Petroleum Geology* 25 (3), 271–288.
- Poliakov, A. N. B., Dmowska, R., Rice, J. R., 2002. Dynamic shear rupture interactions with fault bends and off-axis secondary faulting. *J. Geophys. Res.* 107 (B11), 2295.
- Potts, D. M., Kovacevic, N., Vaughan, P. R., 1997. Delayed collapse of cut slopes in stiff clay. *Géotechnique* 47 (5), 953–982.
- Prindle, R. W., Lopez, A. A., 1983. Pore pressures in marine sediments—1981 test of the geotechnically instrumented seafloor probe (GISP). In: Annu. Proc. Offshore Technol. Conf., Abstract 4463, 8pp.

- Puzrin, A. M., Germanovich, L. N., Apr. 2005. The growth of shear bands in the catastrophic failure of soils. *Proceedings of the Royal Society A: Mathematical, Physical and Engineering Sciences* 461 (2056), 1199–1228.
- Puzrin, A. M., Germanovich, L. N., Kim, S., 2004. Catastrophic failure of submerged slopes in normally consolidated sediments. *Géotechnique* 54 (10), 631–643.
- Rempel, A. W., Rice, J. R., 2006. Thermal pressurization and onset of melting in fault zones. *J. Geophys. Res.* 111, B09314.
- Réthonré, J., de Borst, R., Abellán, M.-A., 2007. A discrete model for the dynamic propagation of shear bands in a fluid-saturated medium. *Int. J. Numer. Anal. Meth. Geomech.* 31 (2), 347–370.
- Revil, A., Cathles, L. M., 2002. Fluid transport by solitary waves along growing faults - A field example from the South Eugene Island Basin, Gulf of Mexico. *Earth Planet. Sc. Lett.* 202 (2), 321–335.
- Rice, J. R., 1968. A Path Independent Integral and Approximate Analysis of Strain Concentration by Notches and Cracks. *J Appl Mech* 35 (2), 379–386.
- Rice, J. R., 1971. Inelastic constitutive relations for solids - an internal-variable theory and its application to metal plasticity. *J. Mech. Phys. Solids* 19 (6), 433–455.
- Rice, J. R., 1975a. Continuum mechanics and thermodynamics of plasticity in relation to microscale deformation mechanisms. In: Argon, A. S. (Ed.), *Constitutive Equations in Plasticity*. M. I. T. Press, Cambridge, Mass., pp. 23–79.
- Rice, J. R., 1975b. Stability of dilatant hardening for saturated rock masses. *J. Geophys. Res.* 80 (11), 1531–1536.
- Rice, J. R., 1977. Pore pressure effects in inelastic constitutive formulations for fissured rock masses. In: *Advances in Civil Engineering Through Engineering Mechanics, Proceedings of 2nd ASCE Engineering Mechanics Division Specialty Conference*, Raleigh, N.C., 1977. Am. Soc. of Civ. Eng., New York, pp. 295–297.
- Rice, J. R., 1980. The mechanics of earthquake rupture . In: Dziewonski, A. M., Boschi, E. (Eds.), *Physics of the Earth's Interior*. Italian Physical Society/North Holland Publ. Co., Amsterdam, pp. 555–649.
- Rice, J. R., 1992. Fault stress states, pore pressure distributions, and the weakness of the San Andreas fault. In: Evans, B., Wong, T.-F. (Eds.), *Fault Mechanics and Transport Properties in Rocks*. Academic Press, pp. 475–503.
- Rice, J. R., 2006. Heating and weakening of faults during earthquake slip. *J. Geophys. Res.* 111, B05311.

- Rice, J. R., Cleary, M. P., 1976. Some basic stress diffusion solutions for fluid-saturated elastic porous-media with compressible constituents. *Rev. Geophys.* 14 (2), 227–241.
- Rice, J. R., Rudnicki, J., 1979. Earthquake precursory effects due to pore fluid stabilization of a weakening fault zone. *J. Geophys. Res.* 84, 2177–2193.
- Rice, J. R., Sammis, C. G., Parsons, R., 2005. Off-fault secondary failure induced by a dynamic slip pulse. *B. Seismol. Soc. Am.* 95 (1), 109–134.
- Rice, J. R., Uenishi, K., Apr. 2010. Rupture nucleation on an interface with a power-law relation between stress and displacement discontinuity. *Int. J. Fract.* 163 (1-2), 1–13.
- Ripperger, J., Ampuero, J.-P., Mai, P. M., Giardini, D., 2007. Earthquake source characteristics from dynamic rupture with constrained stochastic fault stress. *J. Geophys. Res.* 112, B04 311.
- Rubin, A. M., Ampuero, J.-P., 2005. Earthquake nucleation on (aging) rate and state faults. *J. Geophys. Res.* 110, B11312.
- Rubin, A. M., Ampuero, J.-P., 2009. Self-similar slip pulses during rate-and-state earthquake nucleation. *J. Geophys. Res.* 114, B11305.
- Rudnicki, J. W., 1984a. A class of elastic plastic constitutive laws for brittle rock. *J. Rheol.* 28 (6), 759–778.
- Rudnicki, J. W., 1984b. Effects of dilatant hardening on the development of concentrated shear deformation in fissured rock masses. *J. Geophys. Res.* 89, 9259–9270.
- Rudnicki, J. W., 2000. Diffusive instabilities in dilating and compacting geomaterials. In: Chuang, T.-J., Rudnicki, J. W. (Eds.), *Multiscale Deformation and Fracture in Materials and Structures*. Kluwer Acad., New York, pp. 159–182.
- Rudnicki, J. W., Rice, J. R., 1975. Conditions for localization of deformation in pressure-sensitive dilatant materials. *J. Mech. Phys. Solids* 23 (6), 371–394.
- Rudnicki, J. W., Rice, J. R., 2006. Effective normal stress alteration due to pore pressure changes induced by dynamic slip propagation on a plane between dissimilar materials. *J. Geophys. Res.* 111, B10308.
- Segall, P., Rice, J. R., 1995. Dilatancy, Compaction, and Slip Instability of a Fluid-Infiltrated Fault. *J. Geophys. Res.* 100, 22155–22171.
- Sibson, R. H., 1973. Interactions between temperature and pore-fluid pressure during earthquake faulting and a mechanism for partial or total stress relief. *Nature-Phys Sci* 243 (126), 66–68.

- Stark, T. D., Choi, H., McCone, S., 2005. Drained shear strength parameters for analysis of landslides. *J Geotech Geoenviron* 131 (5), 575–588.
- Stark, T. D., Hussain, M., 2010. Shear Strength in Preexisting Landslides. *J Geotech Geoenviron* 136 (7), 957–962.
- Sultan, N., Marsset, B., Ker, S., Marsset, T., Voisset, M., Vernant, A. M., Bayon, G., Cauquil, E., Adamy, J., Colliat, J. L., Drapeau, D., 2010. Hydrate dissolution as a potential mechanism for pockmark formation in the Niger delta. *J. Geophys. Res.* 115, B08101.
- Suzuki, T., Yamashita, T., 2006. Nonlinear thermoporoelastic effects on dynamic earthquake rupture. *J. Geophys. Res.* 111, B03307.
- Suzuki, T., Yamashita, T., 2008. Nonlinear effects of temperature, fluid pressure, and inelastic porosity on dynamic fault slip and fault tip propagation: Emergence of slip strengthening and pulse-like fault slip. *J. Geophys. Res.* 113, B07304.
- Tada, H., Paris, P. C., Irwin, G. R. (Eds.), 2000. *The Stress Analysis of Cracks Handbook*, 3rd Edition. ASME, New York.
- Tanikawa, W., Shimamoto, T., Wey, S.-K., Lin, C.-W., Lai, W.-C., 2008. Stratigraphic variation of transport properties and overpressure development in the Western Foothills, Taiwan. *J. Geophys. Res.* 113, B12403.
- Templeton, E. L., Rice, J. R., 2008. Off-fault plasticity and earthquake rupture dynamics: 1. Dry materials or neglect of fluid pressure changes. *J. Geophys. Res.* 113, B09306.
- Thouless, M. D., Evans, A. G., Ashby, M. F., Hutchinson, J. W., 1987. The edge cracking and spalling of brittle plates. *Acta Metall. Mater.* 35 (6), 1333–1341.
- Tse, S. T., Rice, J. R., 1986. Crustal Earthquake Instability in Relation to the Depth Variation of Frictional Slip Properties. *J. Geophys. Res.* 91, 9452–9472.
- Uenishi, K., Rice, J. R., 2003. Universal nucleation length for slip-weakening rupture instability under nonuniform fault loading. *J. Geophys. Res.* 108 (B1), 2042.
- Vardoulakis, I., 2002. Dynamic thermo-poro-mechanical analysis of catastrophic landslides. *Géotechnique* 52 (3), 157–171.
- Viesca, R. C., Rice, J. R., 2010. Modeling slope instability as shear rupture propagation in a saturated porous medium. In: Mosher, D. C., Shipp, R. C., Moscardelli, L., Chaytor, J. D., Baxter, C. D. P., Lee, H. J., Urgeles, R. (Eds.), *Submarine Mass Movements and Their Consequences*. Springer-Verlag, New York, pp. 215–225.

- Viesca, R. C., Rice, J. R., 2011. Elastic reciprocity and symmetry constraints on the stress field due to a surface-parallel distribution of dislocations. *J. Mech. Phys. Solids* 59 (4), 753–757.
- Viesca, R. C., Templeton, E. L., Rice, J. R., 2008. Off-fault plasticity and earthquake rupture dynamics: 2. Effects of fluid saturation. *J. Geophys. Res.* 113, B09307.
- Viesca-Falguieres, R. C., Rice, J. R., 2010. Anticipated arrest: Insufficient conditions for continued dynamic propagation of a slip-weakening rupture nucleated by localized increase of pore pressure. In: Proc. And Abstracts SCEC Ann. Meet, XX, Abstract 2-036.
- Voight, B., Faust, C., 1982. Frictional Heat and Strength Loss in Some Rapid Landslides. *Géotechnique* 32 (1), 43–54.
- Wang, H. F., 2000. Theory of Linear Poroelasticity with Applications to Geomechanics and Hydrogeology. Princeton Univ. Press, Princeton, N.J.
- Wen, B. P., Aydin, A., 2003. Microstructural study of a natural slip zone: quantification and deformation history. *Eng. Geol.* 68, 289–317.
- Wen, B. P., Aydin, A., 2004. Deformation History of a Landslide Slip Zone in Light of Soil Microstructure. *Env. Eng. Geosci.* X (2), 123–149.
- Westbrook, G. K., Thatcher, K. E., Rohling, E. J., Piotrowski, A. M., Pälike, H., Osborne, A. H., Nisbet, E. G., Minshull, T. A., Lanoisellé, M., James, R. H., Hühnerbach, V., Green, D., Fisher, R. E., Crocker, A. J., Chabert, A., Bolton, C., Beszczynska-Möller, A., Berndt, C., Aquilina, A., 2009. Escape of methane gas from the seabed along the West Spitsbergen continental margin. *Geophys. Res. Lett.* 36, L15608.
- Wiberg, N. E., Koponen, M., Runesson, K., 1990. Finite-element analysis of progressive failure in long slopes. *Int. J. Numer. Anal. Meth. Geomech.* 14 (9), 599–612.
- Xu, W., Germanovich, L. N., 2006. Excess pore pressure resulting from methane hydrate dissociation in marine sediments: A theoretical approach. *J. Geophys. Res.* 111, B01104.
- Yang, F. Q., Li, J. C. M., 1997. Dislocation model of a subsurface crack. *J. Appl. Phys.* 82 (10), 4816–4822.